AEDC-TR-78-19

Cy.1

SIMULATION OF FRICTION, WEAR, AND GOUGING
FOR A HYPERVELOCITY GUIDE-RAIL SYSTEM

Louis I. Boehman, John P. Barber, and Hallock F. Swift

University of Dayton Research Institute
300 College Park Avenue
Dayton, Ohio 45469

May 1978

Final Report for the Period 20 November 1977

TECHNICAL REPORTS
FILE COPY

Approved for public release; distribution unlimited.

Prepared for

ARNOLD ENGINEERING DEVELOPMENT CENTER/XRFX
ARNOLD AIR FORCE STATION, TENNESSEE 37389

This report has been reviewed by the Information Office (OI) and is releasable to the National Technical Information Service (NTIS). At NTIS, it will be available to the general public, including foreign nations.

APPROVAL STATEMENT

This report has been reviewed and approved.

ALBERT E. DIETZ
Facility Planning Division
Director of Facility Plans and Programs

Approved for publication:

FOR THE COMMANDER

JAMES G. MITCHELL
Director of Facility Plans and Programs
Deputy for Planning

UNCLASSIFIED

REPORT DOCUMENTATION PAGE		READ INSTRUCTIONS BEFORE COMPLETING FORM
1 REPORT NUMBER AEDC-TR-78-19	2 GOVT ACCESSION NO.	3 RECIPIENT'S CATALOG NUMBER
4 TITLE (and Subtitle) SIMULATION OF FRICTION, WEAR, AND GOUGING FOR A HYPERVELOCITY GUIDE-RAIL SYSTEM		5 TYPE OF REPORT & PERIOD COVERED Final Report - 15 June 75 - 23 September 77
		6. PERFORMING ORG. REPORT NUMBER UDR-TR-77-68
7 AUTHOR(s) Dr. Louis I. Boehman, Dr. John P. Barber, and Mr. Hallock F. Swift		8 CONTRACT OR GRANT NUMBER(s) F40600-75-C-0008
9 PERFORMING ORGANIZATION NAME AND ADDRESS University of Dayton Research Institute 300 College Park Avenue Dayton, OH 45469		10 PROGRAM ELEMENT. PROJECT. TASK AREA & WORK UNIT NUMBERS Program Element 65807F
11 CONTROLLING OFFICE NAME AND ADDRESS Arnold Engineering Development Center/DOS Air Force Systems Command Arnold Air Force Station, Tennessee 37389		12. REPORT DATE May 1978
		13 NUMBER OF PAGES 156
14 MONITORING AGENCY NAME & ADDRESS(if different from Controlling Office)		15 SECURITY CLASS. (of this report) UNCLASSIFIED
		15a DECLASSIFICATION/DOWNGRADING SCHEDULE N/A

16 DISTRIBUTION STATEMENT (of this Report)

This document has been approved for public release
. . . its distribution is unlimited.

17 DISTRIBUTION STATEMENT (of the abstract entered in Block 20, if different from Report)

18 SUPPLEMENTARY NOTES

Available in DDC

19 KEY WORDS (Continue on reverse side if necessary and identify by block number)

Couette flow   aerodynamic stability
boundary layer   reentry simulation
hypervelocity facility
sliding friction

20 ABSTRACT (Continue on reverse side if necessary and identify by block number)
A computer model was developed to describe friction, wear, and gouging that may occur at the projectile-rail interface of a hypervelocity projectile being guided by alignment rails. Study of the gasdynamics of the interface region reveals that three types of flow can occur depending upon the associated Reynolds number computed with respect to projectile/rail separation, Re_h. The flow conditions are laminar Couette flow ($Re_h < 10^3$); turbulent Couette flow ($10^3 < Re_h < 10^5$); turbulent boundary flow ($Re_h > 10^5$). Pressures developed within the gap

DD FORM 1473 (1 JAN 73)   EDITION OF 1 NOV 65 IS OBSOLETE

UNCLASSIFIED

20. ABSTRACT (Continued)

affect the projectile dynamics significantly and, in turn, are affected by projectile motions and orientations produced by external gasdynamics interactions. In general, the interface pressures act to promote dynamic stability of projectiles in flight. Accordingly, a complete treatment of interface regions required development of a "Projectile Dynamics Computer Program" which describes the complete process of rigid projectiles passing along rail guidance systems. Program output demonstrates that drag forces caused by interface phenomena are negligible in comparison with other forces acting on the projectile. Further use of the program leads to identification of three levels of projectile stability with resultant effects upon friction, wear, and gouging: (1) when the projectile is aerodynamically stable it can traverse the guidance rail with virtually no wear other than that caused by rail imperfections; (2) when projectiles are aerodynamically unstable to a minor extent, stability can be achieved through action of the interface regions but projectile wear is produced by the required forces; (3) when projectiles are very unstable aerodynamically they will contact the rails which may lead to gouging, rapid wear and possibly catastrophic failure. The computer model also predicts that the projectile bow shockwave reflected from the rails impinges upon the forebodies of projectiles in flight, thereby increasing total drag forces considerably.

Comparisons between predicted and observed projectile friction, wear, and gouging in Tracks K and G are also presented.

AFSC
Arnold AFS Tenn

PREFACE

TABLE OF CONTENTS

TABLE OF CONTENTS (Continued)

LIST OF ILLUSTRATIONS

LIST OF ILLUSTRATIONS (CONT'D)

LIST OF TABLES

SECTION I

INTRODUCTION

This report describes an analysis of the sliding
phenomena that occur during operation of a hypervelocity guide-
rail system. As such systems come into wide use in the hyper-
velocity experimental field it becomes increasingly important
to understand the behavior of the sliding contact between the
projectile and rails. Very large guide-rail systems (both in
bore diameter and length) are currently being contemplated.
The technical feasibility of such systems will depend, among
other things, on the magnitude of the frictional forces and
associated projectile wear, and other behavior peculiar to hyper-
velocity sliding contacts such as gouging. This study was initiated
to investigate friction, wear, and gouging in hypervelocity
guide-rail systems. The objective of the investigation was to
develop an analysis of hypervelocity sliding which could be
used to evaluate frictional forces, projectile wear and the
probability of gouging behavior for both existing and proposed
guide-rail systems. To maintain the required generality a funda-
mental approach was employed. The basic phenomena were identified,
analyzed and combined into an overall interface model. This
model was then combined with the projectile/rail dynamics to
provide the overall friction, wear, and gouging evaluation tool.

This section begins with a general description of guide-
rail systems and a detailed description of the Arnold Engineering
Development Center (AEDC) Hypervelocity Tracks K and G, which
were the specific systems used to exercise the model. It must
be emphasized that our analysis is not restricted in any sense
to the track K or track G parameters and can be applied to any
guide-rail configuration now in use, under construction, or being
contemplated. An introduction to the projectile/rail sliding

9

phenomena which will be treated is then presented. Finally, the effects of projectile dynamics are outlined.

The remainder of the report deals in detail with the sliding phenomena, the interface model, the projectile dynamics, a computer program designed to describe the performance of hypervelocity guide-rail systems, and comparisons between results computed with this program and data from experimental firings.

1.1   GUIDE RAIL SYSTEMS

A guide-rail system is a device which basically takes a projectile as delivered from the muzzle of a gun and guides it via a fixed rail system through a prescribed atmospheric environment. The application under consideration is a hypervelocity guide-rail system employed in a reentry vehicle simulation and test facility. A model (the projectile) is launched through a typical reentry environment and undergoes ablation and erosion similar to that encountered during an actual reentry.

The principal advantage of a guide-rail system is that it provides precise control of projectile orientation and location during flight. This control permits satisfactory ballistic experimentation with projectiles that have at least some level of aerodynamic instability and lift. Free flight ranges are limited to testing with aerodynamically stable and zero lift projectiles in order to keep the projectile on a reasonably straight and predictable trajectory such that its behavior can be closely observed. This limitation becomes critically important for tasks such as erosion testing where non-symmetrical nosetip mass loss can generate lift and subsequent projectile fly-off.

Guide rail systems do, however, perturb the aerodynamic flow around projectiles in flight. These perturbations reduce the area of the forebody that can be used for testing and cause increased drag on the projectile. The increased drag can result in unacceptable velocity drop over the flight range and reduce the effective test time of the range. In addition, friction and flow interaction phenomena arising in the projectile/rail

interface region can augment the drag (and thus the velocity drop) and can threaten projectile integrity by inducing large amounts of projectile wear.

There are currently four hypervelocity guide rail systems in operation; Tracks K and G at AEDC, the McDonnell Douglas range in El Segundo, California, and the Air Force Materials Laboratory/ University of Dayton Research Institute (AFML/UDRI) light gas gun range at Wright-Patterson Air Force Base. Larger systems are in the preliminary planning stages at AEDC. This report is principally concerned with the AEDC ranges; however, the analysis has been made sufficiently general to handle the scaling between the various ranges currently in operation or being planned. As Tracks K and G are currently operating and some performance data are available, typical parameters for these two facilities will be used for example problems.

1.1.1   Track K Parameters

Track K is typical of current guide rail designs and is described in some detail by Teng, et al.[1] A drawing of the system is shown in Figure 1. There are two sets of opposing rails 7.92 mm wide. The inside of the guide tube is accurately honed to 96.52 mm $^{+30}_{-0}$ $^{\mu m}_{\mu m}$. The rail height is then precision ground to 27.43mm $^{+30}_{-0}$ $^{\mu m}_{\mu m}$ and the rails are located on the inside of the tube to provide an inter-rail gap of 41.33 mm ±30 μm. The guide tubes are constructed in 3.05 m sections and ten of them are connected together to form a system 30.5 m long. Care was taken to ensure proper inter-section alignment.

The Range K light gas gun has a 41.28 mm diameter launch tube and typically launches cylinders with various forebodies. The gap between the guide-rails and the projectile is nominally 50 μm*. The projectiles typically have a cylindrical section

---

*Recent in-flight measurements of projectiles launched on the Track K facility show projectiles having post launch diameters of 40.64 mm resulting in an increased gap height of the order of 350 μm.
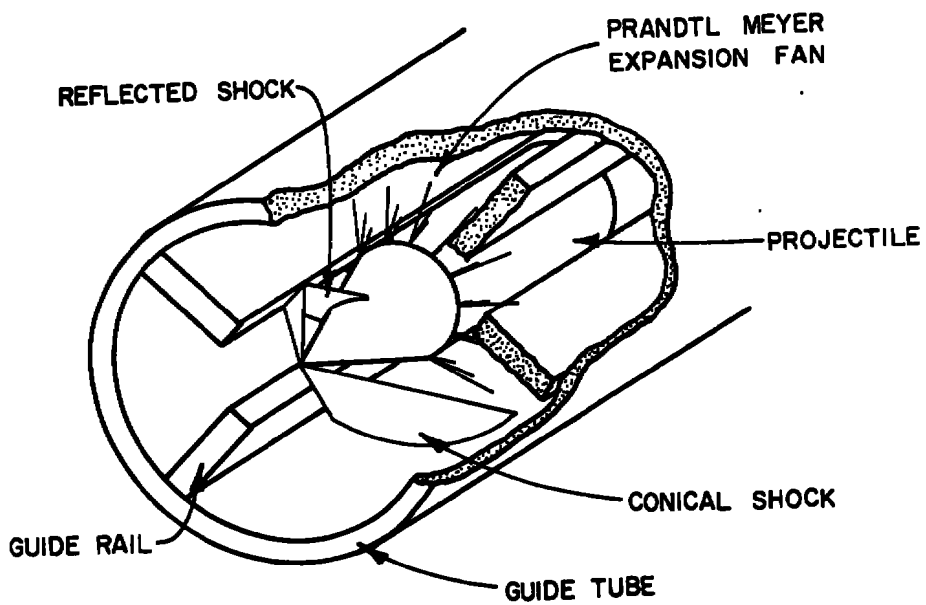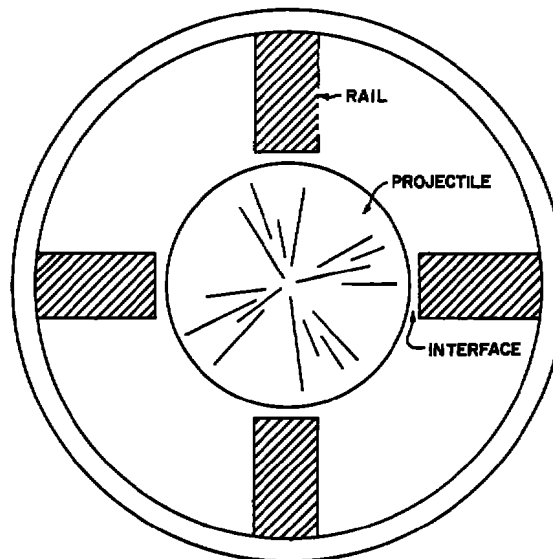
Figure 1.   A Typical Guide-Rail System.

41.28 mm long giving a nominal rail contact area of 327 mm^2 per rail. The half-angles of the conical forebodies are typically in the range of 45° to 10°. For simulation of typical current and projected reentry vehicles, half-angles of 10° are most appropriate. Therefore, principal attention in analysis development was directed to cone half-angles between 10° and 30°.

Projectiles are typically constructed from polycarbonate plastic material. For reentry simulation, the cone section surface must be a more realistic reentry vehicle nose tip material such as graphite. Typically, the cones are either covered with or fabricated from materials of interest, but the cylindrical portion which contacts the rails will probably remain poly-carbonate or some other impact resistant plastic.

The Track K launcher typically launches these projectiles to velocities between 2.5 km/s and 4.5 km/s although reentry testing can be extended up to velocities approaching 6 km/s. The range atmosphere is usually air at densities between 0.1 and 1.0 atm depending on the stage of reentry to be simulated.

The following is a list of the parameters of interest for the Track K at AEDC with typical values:

1. Projectile:

      Velocity – 2.5 km/s to 4.5 km/s

      Material – Polycarbonate

      Geometry – 41.28 mm diameter cylinder
                     10° to 30° half-angle conical forebody

2. Rails:

      Material – Steel

      Inter-rail gap – 41.33 mm

      Length – 30 m

3. Projectile – Rail Interface:

      Gap height – ≤0.35 mm nominal

      Contact area ∿300 mm^2 nominal

4. Range Atmosphere:

      Gas – air

      Pressure – 0.1 atm to 1.0 atm

1.1.2 Track G Parameters

Track G is similar to Track K, but considerably larger. The Range consists of a light gas gun with a 63.5 mm diameter launcher tube and a nominal 300 m long free flight, range tank. The track system is installed in the range tank such that it can be swung off trajectory to permit unguided projectile testing. The track and range system is described in detail by Norfleet et al.[2] Track G parameters are summarized as follows:

1. Projectile:

   Velocity - 3 km/s to 6 km/s

   Material - Composite with polycarbonate resin sabot, aluminum or titanium internal strut and heat shield back up material, and carbon epoxy heat shield material

   Geometry - 63.5 mm (2.5 inch) diameter cylinder (nominal). Various forebody designs

2. Rails:

   Material - Steel

   Inter-rail gap - 63.5 mm

   Length - 277.4 m (910 ft). 91 sections 10 ft/section

3. Projectile - Rail Interface:

   Gap height - $\leq$.50 mm (0.020 inch) nominal

   Contact area - 500 mm^2 nominal

4. Range Atmosphere:

   Gas - air (can use nitrogen, argon, helium, etc)

   Pressure - 0.00026 atm to 1.0 atm

1.2 PROJECTILE-RAIL SLIDING PHENOMENA

This report is particularly addressed to describing the phenomena associated with projectile-rail sliding and the effects of these phenomena on guide-rail performance. Three aspects of hypervelocity sliding will be treated; friction, wear, and gouging.

Friction occurs when any two solid surfaces in close proximity slide with respect to one another. The frictional force opposes the slider (projectile) motion and so adds to the aerodynamic drag force on the projectile. This effect should be small for a successful guide-rail system.

Wear is closely associated with the frictional process and is defined as the mass removed from the rail and/or projectile by the sliding process. Wear is important in guide rail systems for three reasons:

1. Wear increases the projectile-rail gap separation and thus degrades the position and orientation control of the system.

2. Wear could remove sufficient material to appreciably lower the available testing area of the projectile.

3. Wear could remove sufficient material to threaten projectile integrity either by parting the projectile or by providing sufficient space for lateral or rotational oscillations of the projectile to grow and ultimately disintegrate the projectile.

As wear, no doubt, increases with the distance traveled, all of these problems could become very important on the very long ranges under consideration. Indeed, wear has been found to be an important constraint in Track G. Wear on Track K models has, on the other hand, been minimal.

Gouging is a phenomenon peculiar to hypervelocity sliding contacts.[3,4,5] Under certain conditions tear shaped craters are formed on the rail (and presumably the projectile) surface during sliding. Gouging, therefore, is a relatively violent process and has two possible detrimental effects:

1. The rails can become so damaged that they must be refinished or replaced periodically. This will be expensive and time consuming when very large and long systems are developed.

2. The violence of the gouging process could result in disintegration of the projectile and complete loss of data. Subsequent rail refinishing or replacement would again be required.

15

This investigation is addressed to understanding friction, wear, and gouging phenomena sufficiently to design long rail systems and/or to scale the behavior of current systems to ones developed in the future.

1.3   PROJECTILE-RAIL DYNAMICS

The behavior of the interface region between the projectile and the rail is a function of the dynamics of the projectile in the rail system. In particular, the projectile can undergo relative lateral translation and rotation due to aerodynamic forces and moments and the curvature of the rails. These projectile motions result in changes in the interface behavior which, in turn, affects system dynamic behavior performance. It is, therefore, necessary to incorporate projectile and coupled interface dynamics into any realistic description of guide-rail performance.

This report identifies the phenomena of importance in hypervelocity sliding. These phenomena are then analyzed in detail and modeled for the particular conditions of interest in guide-rail systems. The dynamics of rail guided projectiles are then analyzed and modeled. Finally, the interface model and projectile dynamics model are combined to provide an overall model of the dynamic behavior of hypervelocity guide-rail sliding performance. The results obtained from exercising the combined program are compared with the experimental data currently available.

SECTION II

BACKGROUND REVIEW OF SLIDING PHENOMENA

The following paragraphs outline background information
on the sliding of solids and describe the conceptual framework
in which the present problem will be investigated.

2.1   LOW AND MEDIUM VELOCITY SLIDING

Low to medium velocity friction has been studied exten-
sively and is described in a book by Bowden and Tabor.[6] It is
instructive to review briefly these well-understood mechanisms
before considering phenomena occurring during hypervelocity
sliding.

Static friction between solids is attributed to the
cold welding of asperities on the surfaces as they are brought
into contact. A tangential force applied to the interface must
shear these welded regions, thus giving rise to the frictional
force. The area of welded contact is proportional to the
normal force and the shear, or friction force is proportional
to the area of welded contact. Therefore, the coefficient of
friction which is defined as the ratio of the maximum frictional
force to the normal force, is predicted to be independent of the
normal force, as is observed experimentally. The process is a
material shear strength dominated phenomenon.

When motion takes place, the welded areas shear, new
ones form, and the behavior remains essentially the same as for
static friction.

As sliding velocities increase, there is insufficient
time for the heat dissipated during shearing to be conducted into
the bulk material. Thermal equilibrium cannot be established,
and the shear region heats up. The rise in temperature at the

17

interface results in a lowering of the shear strength of the
material in the cold welded areas and friction forces decline.
Typically, the coefficient of friction declines as shown in
Figure 2. Finally, the entire interface becomes covered with
a molten layer and the friction becomes essentially fluid
dynamic and dependent upon: (a) the viscosity of the molten
interface materials; (b) sliding velocity; and (c) interfacial
thickness. Therefore, over some range of velocity, the friction
process transitions from strength dominated to viscous dominated.

The viscous force, F, which takes the place of the
classic friction force once surface melting occurs, may be
expressed in the form;

$$F = \bar{\mu}A \frac{dv}{dy} , \qquad (1)$$

where $\bar{\mu}$ is the coefficient of viscosity, A is the area of the
interface, and dv/dy is the transverse velocity gradient in the
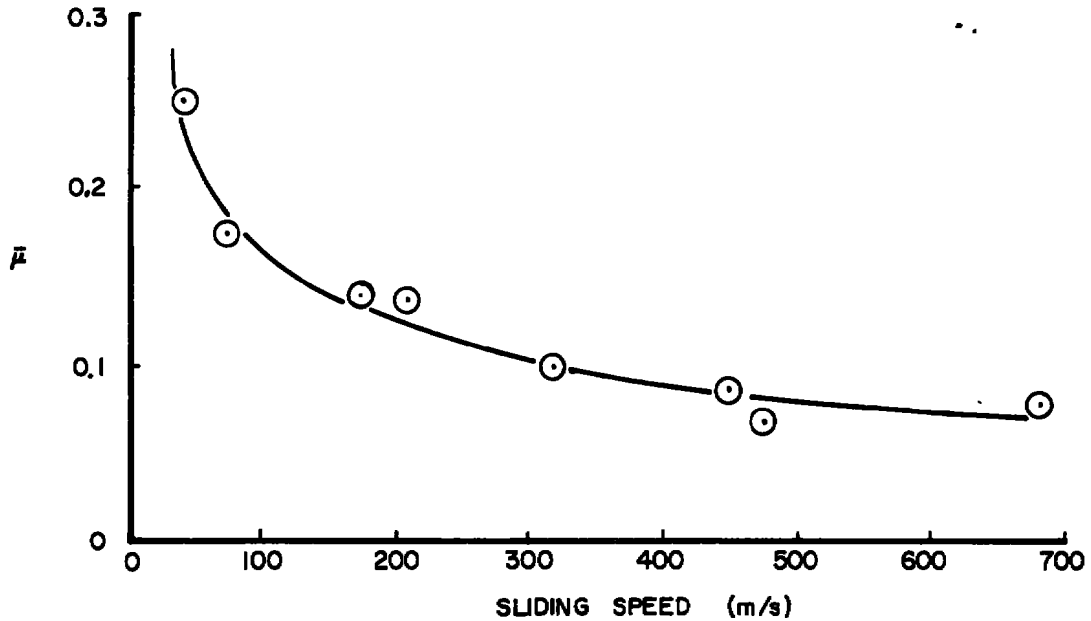
Figure 2. The Coefficient of Friction, $\bar{\mu}$, for Steel on Nylon
as a Function of Sliding Velocity. (Taken from
Bowden and Tabor,[6] Pg. 476).

18

interface zone (i.e., transverse to the sliding direction). The
average velocity gradient between surfaces sliding at velocity v
and separated by distance h is;

$$(dv/dy)_{av} = v/h. \tag{2}$$

Note that the separation, h, is the distance between solid pro-
jectile and rail surface. Substituting this expression into the
previous equation, we arrive at an "average" viscous force,
F_{av};

$$F_{av} = \frac{\bar{\mu} A v}{h} . \tag{3}$$

As shown in Equation (3), the viscous force varies directly
with the viscosity and velocity and inversely with separation
distance.

It should be noted here that, for a fluid dynamic
interface, the frictional force will have a strong velocity
dependence. Such frictional behavior makes it difficult to
distinguish between sliding "friction" and aerodynamic drag in
projectile deceleration data acquired from guide-rail systems.
As the aerodynamic drag is also velocity dependent, the func-
tional dependences of the "friction" and the aerodynamic drag
may well be nearly identical.

Further increases in sliding velocity result in diminish-
ing thermal equilibrium in the interface and the thickhess, h,
of the interface zone contracts, resulting in higher velocity
gradients within the fluid layer and increased drag. The
available experimental data on high speed contacts ends at about
700 m/s, well below the velocities at which this investigation
begins.

2.2   HYPERVELOCITY SLIDING

As velocity increases from zero the friction mechanism quite clearly changes from a material strength dominated phenomena to a viscous dominated process and hypervelocity friction is almost certainly a completely viscous process.

A logical extension to the previous discussion appears to be that, as velocity is further increased, the energy dissipation rate in the interface becomes sufficient to vaporize significant amounts of the interfacial material. In addition, for a guide-rail system, ambient air is entrained by the projectile motion and injected into the interface forming a self-pumped gas bearing.

The gas velocity varies across the interface from zero at the rail surface to the sliding velocity at the projectile surface. The average velocity of the interfacial material is, therefore, approximately one-half the sliding velocity. Material originating at the projectile or rail surface and moving into the interfacial layer must convert, on the average, 3/4 of its original kinetic energy to other forms of energy. This energy becomes available for chemical decomposition of the material, material heating, and phase changes (i.e., melting, boiling, or sublimation).

If we neglect energy described in phase changes and decomposition and consider that all the available kinetic energy is converted to thermal energy we obtain for a monatomic gas;

$$\frac{3nmU_\infty^2}{8} = \frac{3nKT}{2} \, , \tag{4}$$

where n is the number density of atoms, m is the molecular mass, K is Boltzman constant, U_∞ is the sliding velocity and T is the gas temperature. Solving for T we obtain;

$$T = \frac{m \, U_\infty^2}{4 \, K} \, , \tag{5}$$

20

Solutions for Equation (5) are shown in Table 1 for various atoms
that might be present in the interface. Larger polyatomic
molecules have larger masses (and kinetic energy) but they also
have more degrees of freedom in which to absorb energy. The
temperatures for polyatomic molecules are therefore probably
lower for single atom molecules, but the same order of magnitude
as those displayed in Table 1.

TABLE 1. GAS TEMPERATURES VS. SLIDING VELOCITY FOR OXYGEN,
CARBON, NITROGEN

	GAS TEMPERATURE, °K		
U_∞m/s	O (16)	C (12)	N (14)
1000	484	363	423
2000	1936	1452	1694
3000	4356	3267	3811
4000	7744	5808	6776
5000	12101	9076	10588
6000	17426	13069	15247
7000	23718	17789	20753

The energy available to the interfacial zone varies as the
square of the sliding velocity. Therefore, vaporization might
be expected at moderate velocities, perhaps of the order of a
few kilometers per second for the materials currently used for
hypervelocity projectiles, and the interface will display gas
dynamic behavior. It should also be noted that many plastics
such as Teflon sublime rather than melt when heated and the
frictional behavior of these materials might not display the
hydrodynamic phase but transfer directly to the gas dynamic
phase in a similar manner to a recently proposed solid CO_2
bearing.[7]

Frictional forces might be expected to be extremely
small for an ablative gas dynamic bearing, but will increase
with velocity because the interface thickness will contract

(leading to higher transverse velocity gradients) due to increasing thermal disequilibrium and its temperature will rise resulting in increasing gas viscosity. For hypervelocity sliding, therefore, a gaseous interface will be considered except when normal loads become sufficient to reduce the interface to zero thickness causing direct contact between the projectile and the rail. Such direct contact results in extremely high transverse velocity gradients. The high energy dissipation rates associated with these gradients could account for the crater-like surface damage characteristics of gouging. This conceptual approach to gouging is supported by the work of Graff and Dettloff[3] who studied high velocity gouging observed during operation of rocket sled tracks. They found that gouging occurred only when a critical normal force between a projectile and a rail was exceeded and that gouging could be inhibited by coating the rail with a variety of soft materials. We feel that both reducing the normal forces and introducing a soft pressure bearing but essentially fluid layer serve to maintain separation between the solid elements and keep the transverse velocity gradients sufficiently low to prevent gouging.

SECTION III

SLIDING IN A HYPERVELOCITY RAIL SYSTEM

3.1   INTRODUCTION

As was mentioned in Section II, sliding in a hypervelocity rail system is basically a fluid dynamic phenomenon except when critical normal loads become sufficient to reduce the interface to nearly zero thickness. The minimum thickness below which the interface can no longer be considered to be purely fluid dynamic is on the order of the surface roughness of either the rail or the projectile surface, whichever is larger. The critical normal load required to reduce the interface to a thickness on the order of the dimensions of surface asperities can be expected to increase as the projectile velocity increases because the viscous dissipation will increase and therefore the ablation rate will increase. The presence in the interface of gases from ablated material makes an additional contribution to the pressure of the gas in the interface over and above that due to fluid dynamic effects.

The interface thickness, which will be called gap height, is the critical parameter in a discussion of hypervelocity rail systems. Various flow regimes can be hypothesized depending on the gap height. A convenient gauge for determining the type of flow regime which can be expected is the lubrication Reynolds number Re* defined as;

$$Re* = \rho \frac{U_\infty B}{\mu} \left(\frac{h}{B}\right)^2 , \tag{6}$$

of which ρ is the gas density, B is the length of the projectile cylindrical surface, U_∞ is the projectile velocity, μ is the gas viscosity, and h is the gap height. If Re*<<1, the interfacial

23

flow is completely dominated by viscous forces and the inertial effects of the gas flow are negligible.[8] In this case, the interface flow can be treated as a purely laminar flow in which only the viscous terms in the governing equations (Navier Stokes equations) are considered. If Re* is of order 1, then the flow is still laminar, but inertia terms must be included. If Re*>>1, the flow is turbulent.

Thus, determining the interface forces acting on a projectile in a hypervelocity guide-rail system is a fluid dynamic problem except when normal forces are greater than the critical normal force required to produce solid-solid contact. In this section we present and discuss the methods and procedures which have been used to determine the fluid dynamic forces on the projectile and to determine the wear of the projectile due to ablation caused by aerodynamic heating. The special forms of the governing equations used to model the various flow regimes are discussed along with the boundary conditions to be applied to the governing equations. The methods and procedures used to describe the material properties including thermodynamic and transport properties of the gas are also presented.

3.2   GOVERNING EQUATIONS

The Navier Stokes (N-S) equations of fluid dynamics are the basic equations to be applied. The full N-S equations will not be written out here since they can be found in any standard fluid dynamics textbook (see Chapter 12 of Reference 9 for example). The special forms of the N-S equations applicable to the three different flow regimes listed in the previous paragraphs will, however, be given since they form the basic elements of the fluid dynamic models developed under this effort.

3.2.1   Coordinate System

Before discussing the governing equations themselves, the coordinate system in which the fluid dynamic equations are to be solved will first be developed. First, it should be emphasized

24

that the overall objective of this effort is to determine the
wear history of a projectile as it moves down the rail system.
The forces required to determine the trajectory of the pro-
jectile are basically transient in nature since the basic fluid
dynamics is transient. In order to be able to develop relatively
simple fluid dynamic models for determining the forces on the
projectile, it was necessary to perform a quasi-steady analysis
of the flow field. That is, it was assumed that the flow adjusts
rapidly enough to changes in angle-of-attack and position of
center-of-gravity that a steady flow solution to an instantaneous
geometry would adequately describe the instantaneous forces on
the projectile. From the point of view of an observer in a
coordinate system fixed to the rails, the flow is always transient.
However, an observer riding with the projectile sees a relatively
steady flow situation as long as the aerodynamic blockage in the
system is not too great.* Thus, the coordinate system used in
this work is one attached to the projectile and it is assumed
that the blockage ratio is greater than 3. In this coordinate
system an observer riding with the projectile sees the range
gas and the rails moving toward him with a velocity that is equal
and opposite to the absolute velocity of the projectile. The
basic flow situation is sketched in Figure 3. For the interface
flow analysis the coordinate system origin is taken as shown in
Figure 4.

Some details of the shock wave structure due to the
presence of the rails are shown in Figure 3. Note particularly
that boundary layer buildup begins on the rail at the point where
the bow shock intersects the rail.

---

*In Reference 1, it is suggested that if the open area of the
range tube divided by the closed area is greater than three, a
normal shock will not move down the range tube ahead of the pro-
jectile and the flow relative to the projectile will be steady.
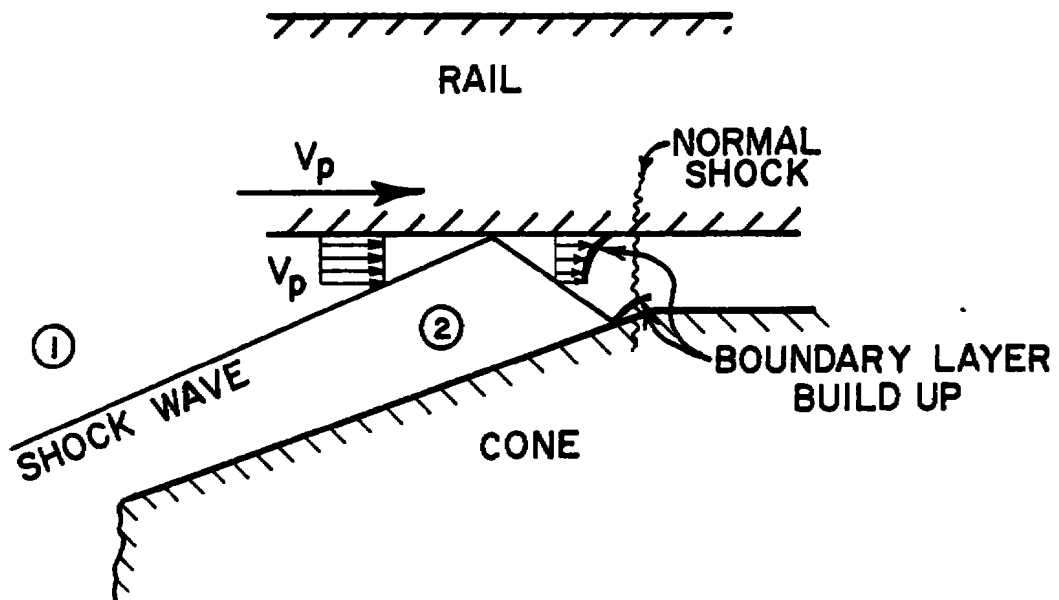
Figure 3.   Boundary Layer Build-up.
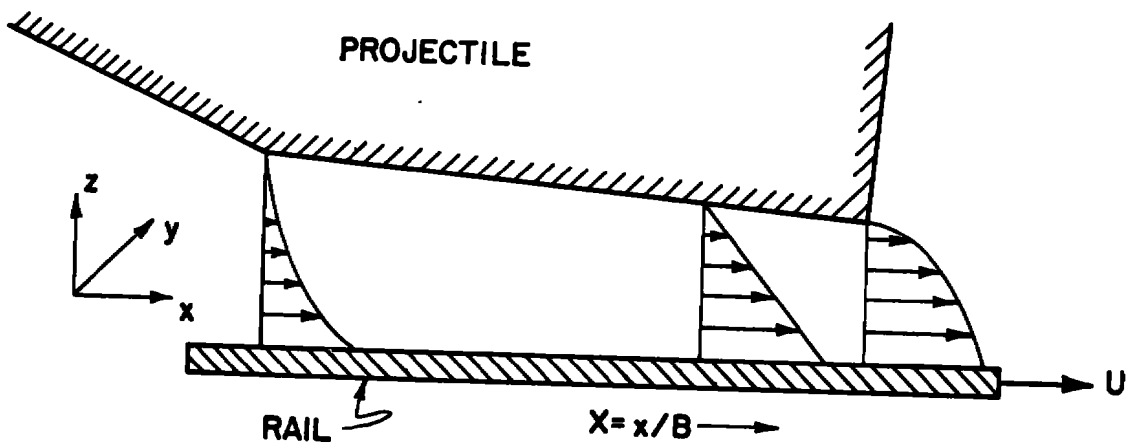
Figure 4.   Coordinate System for Projectile-Rail Interface.

3.2.2   The Reynolds Equations

By assuming steady flow in the interface and neglecting the inertial terms, body forces, z-direction components and pressure gradient, the classical momentum equations for the interface flow reduce to;

$$\frac{\partial P}{\partial x} = \frac{\partial}{\partial z}\left(\mu\frac{\partial u}{\partial z}\right) = \frac{\partial}{\partial z}\left(\tau_{xz}\right),\qquad(7)$$

and;

$$\frac{\partial P}{\partial y} = \frac{\partial}{\partial z}\left(\mu\frac{\partial v}{\partial z}\right) = \frac{\partial}{\partial z}\left(\tau_{yz}\right),\qquad(8)$$

in which $P=P(x,y)$, $u=u(x,y,z)$ and $v=v(x,y,z)$. In these equations, P is the pressure, u is local gas velocity in the x direction, v is the local gas velocity in the y direction, τ_{xz} is the viscous shear force acting in the x-direction on a plane perpendicular to the z-direction and τ_{yz} is the viscous shear force acting in the y-direction on a plane perpendicular to the z-direction.

The continuity (conservation of mass) equation is;

$$\frac{\partial}{\partial x}(\rho u) + \frac{\partial}{\partial y}(\rho v) + \frac{\partial}{\partial z}(\rho w) = 0,\qquad(9)$$

where the terms u, v, w are velocities in the x,y,z directions, respectively.

Integrating with respect to z, one obtains;

$$\rho w\Big|_{z=0}^{z=h} = -\int_0^h\left[\frac{\partial}{\partial x}(\rho u) + \frac{\partial}{\partial y}(\rho v)\right]dz.\qquad(10)$$

By interchanging the order of integration and differentiation the following equation is obtained;

27

$$\rho w \Big|_{z=0}^{z=h} = - \frac{\partial}{\partial x}\int_0^h \rho u \, dz - \frac{\partial}{\partial y}\int_0^h \rho v \, dz. \qquad (11)$$

The left hand side of the above equation is zero if there is
no ablation since the w-component of velocity vanishes at solid
surfaces.

Integration of Equation (7) yields;

$$\frac{\partial P}{\partial x} z = \mu\frac{\partial u}{\partial z} + c_1 (x) \text{ or,}$$

$$\frac{\partial u}{\partial z} = \frac{1}{\mu} \frac{\partial P}{\partial x} z - \frac{c_1 (x)}{\mu} , \qquad (12)$$

$$u = \int_0^z \frac{1}{\mu} \frac{\partial P}{\partial x} z \, dz - c_1 \int_0^z \frac{1}{\mu} \, dz + U_\infty,$$

where $c_1(x)$ is an integration constant and the no-slip condition,
$u=U_\infty$ at $z=0$ has been applied.

For the simplified case where the viscosity is taken
to be a constant (or replaced by a suitably defined average
value) the following equation for u is obtained;

$$u = \left[U_\infty - \frac{hz \ (\partial P/\partial x)}{2\mu}\right] \left(1 - \frac{z}{h}\right) . \qquad (13)$$

For the case of constant viscosity, integration of
Equation (8) yields;

$$v = \frac{hz \ (\partial P/\partial y)}{2\mu} \left(1 - \frac{z}{h}\right) . \qquad (14)$$

The velocity field for constant fluid viscosity is thus a
combination of very elementary viscous flows. Equation (13)
represents the solutions to laminar Couette flow[8] with pressure

gradient (Petrov-Couette flow[8]) and Equation (14) represents
plane Poiseuille[8] flow. The velocity field obtained by super-
position of these two elementary flows is assumed to describe
the basic interface flow for the case of very small gap heights
(Re*<<1). The primary objective here, however, is not necessarily
to define precisely the velocity field, but rather to determine
reasonable approximations to the normal and shear force distri-
butions on the projectile. The pressure distribution on the pro-
jectile could be obtained by combining Equations (11), (12), and
(13), yielding the well-known Reynolds Equation of lubrication
theory;

$$\frac{\partial}{\partial x}\left(\frac{\rho h^3}{\mu}\frac{\partial P}{\partial x}\right) + \frac{\partial}{\partial y}\left(\frac{\rho h^3}{\mu}\frac{\partial P}{\partial y}\right) = 6\frac{\partial}{\partial x}\left(\rho U_\infty h\right) + 12\,\rho W. \qquad (15)$$

The term W is the projectile velocity component normal to the
rail. The solution to this equation yields the pressure dis-
tribution. Integration of the pressure distribution over the
interface region then determines the total normal force on the
projectile in the interface. The viscous shear forces on the
projectile could then be determined by solving for $\tau_{xz}(z=h)$
and $\tau_{yz}(z=h)$ in Equations (7) and (8) respectively.

Application of Equation (15) to determining the pressure
distribution and shear force distribution on the projectile over
the interface region for hypervelocity· guide rail systems is a
formidable task. The density and viscosity in Equation (15) are
highly variable in the z-direction because of the large temper-
ature variation through the interface gap. In order to determine
the temperature variations through the interface gap, the energy
equation must be coupled to Equation (15). The energy equation
for the case of Re*<<1 is given by;[8]

$$u\frac{\partial P}{\partial x} + v\frac{\partial P}{\partial y} + \frac{\partial}{\partial z}\left(k\frac{\partial T}{\partial z}\right) + \mu\left[\left(\frac{\partial u}{\partial z}\right)^2 + \left(\frac{\partial v}{\partial z}\right)^2\right] = 0. \qquad (16)$$

The term k in Equation (16) is the thermal conductivity of the gas in the interface.

Thus, a highly non-linear strongly coupled system of partial differential equations would have to be solved, in order to determine the pressure and shear force distribution over the projectile. This could only be done numerically and would require far more computer time, even for a simple geometry, than would be practical for the present task.

Therefore, approximate solutions to Equations (15) and (16) available in the literature were used to establish order-of-magnitude estimates of the pressure and shear forces in the interface region. These approximate solutions were primarily those obtained for compressible Couette flow. The rationale for making extensive use of compressible Couette flow solutions (for both laminar and turbulent cases) in the present effort is discussed later in Section 3.5 after the governing equations for the Re*≈1 and Re*>>1 situations have been presented and after the boundary conditions have been discussed.

3.2.3   Governing Equations for Re*≈1

The Reynolds Equation (15) is based on purely viscous flow. If the gap height is large enough for Re* to be of order one, the fluid inertia terms are important and must be included. The addition of fluid inertia terms to Equations (7) and (8) yields the following equations;

$$\rho\left(u\frac{\partial u}{\partial x} + v\frac{\partial u}{\partial y}\right) = -\frac{\partial P}{\partial x} + \frac{\partial}{\partial z}\left(\mu\frac{\partial u}{\partial z}\right),\tag{17}$$

and;

$$\rho\left(u\frac{\partial v}{\partial x} + v\frac{\partial v}{\partial y}\right) = -\frac{\partial P}{\partial y} + \frac{\partial}{\partial z}\left(\mu\frac{\partial v}{\partial z}\right).\tag{18}$$

Solutions to Equations (17) and (18) available in the gas bearing
lubrication literature show that inertia effects are generally
small in terms of influencing the forces on gas bearing surfaces
when Re* is of order one, but become increasingly important as
Re*>>1. However, when Re* becomes much larger than 1, turbulence
effects become the primary inertia effects and so the solution
to Equations (17) and (18) are useful to the present problem
only over a very limited range of gap heights. Thus, no effort
was made to develop an interface flow model which included
laminar flow with inertia terms included.

3.2.4   Governing Equations for Re*>>1

The applicable equations for the flow in the interface
when Re* is much larger than one are the turbulent boundary layer
equations for compressible flow. Because the ratio h/B is a
very small number in the hypervelocity guide rail system, it is
appropriate to use a mixing length theory to relate the Reynolds
stress to density and mean velocity gradient. The turbulent
boundary layer equations for three dimensional boundary layers
are;

$$\frac{\partial}{\partial x}(\rho u) + \frac{\partial}{\partial y}(\rho v) + \frac{\partial}{\partial z}(\rho w) = 0, \qquad (19)$$

$$\rho\left(u\frac{\partial u}{\partial x} + v\frac{\partial u}{\partial y} + w\frac{\partial u}{\partial z}\right) = -\frac{\partial P}{\partial x} + \frac{\partial}{\partial z}\left(\mu\frac{\partial u}{\partial z}\right) + \frac{\partial}{\partial z}[(-\rho w)' u'] \quad , \quad (20)$$

$$\rho\left(u\frac{\partial v}{\partial x} + v\frac{\partial v}{\partial y} + w\frac{\partial y}{\partial z}\right) = -\frac{\partial P}{\partial y} + \frac{\partial}{\partial z}\left(\mu\frac{\partial v}{\partial z}\right) + \frac{\partial}{\partial z}[(-\rho v)' w'] \quad . \qquad (21)$$

Quantities primed represent turbulent fluctuations of the
specified quantity. Following the work of Korkegi, et al., [10,11,12]
the Von Karman mixing length model is used to relate the Reynolds
stress terms to mean velocity gradients. The last term in
Equations (20) and (21) are then respectively;

$$\frac{\partial}{\partial z}[(-\rho w)' u'] = \rho \ell_z^2 \left| \frac{\partial u}{\partial z} \right| \frac{\partial u}{\partial z} , \qquad (22)$$

$$\frac{\partial}{\partial z}[(-\rho v)' w'] = \rho \ell_z^2 \left| \frac{\partial w}{\partial z} \right| \frac{\partial w}{\partial z} . \qquad (23)$$

These equations, like the Reynolds Equations, are much too difficult to solve as a part of the interface flow model and recourse is made to using approximate solutions available in the literature. In particular, extensive use has been made of the work of Korkegi and Briggs[10, 11, 12] on hypersonic slipper bearings and turbulent Couette flow. The hypersonic slipper bearing analyses of Korkegi and Briggs as well as the general literature on gas bearing analyses is not directly adaptable to the present problem because of differences in boundary conditions.

3.3   BOUNDARY CONDITIONS FOR INTERFACE REGION

In order to completely define an interface flow model, the boundary conditions to be applied to the interface must be specified.

3.3.1   Entrance Conditions

The conditions of the flow just as it enters the interface are primarily determined by the aerodynamics of the nose cone guide-rail system. As is depicted in Figure 5, the conical shock attached to the cone tip interacts with the rail to produce a complicated shock-expansion wave system imbedded in the cone flow field. The velocity profile at the entrance to the interface is basically three-dimensional and is influenced by the boundary layer buildup both on the cone and on the rail section preceding the interface. Some of the details of how the interface entrance conditions are defined are given in the following paragraphs. The other boundary conditions are discussed in succeeding paragraphs.

TUBE

RAIL

① ② ③
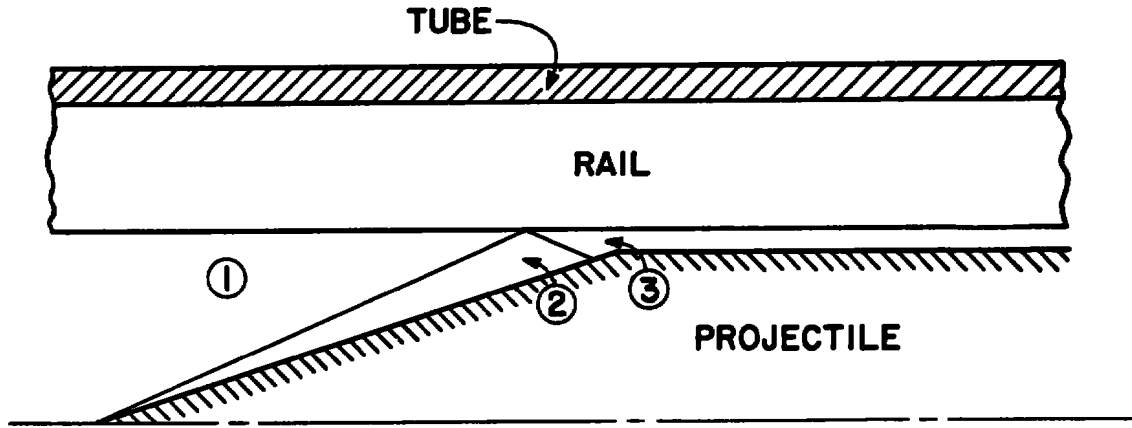
PROJECTILE

Figure 5. Projectile-Rail Geometry.

The initial effort centered on determining the entrance conditions for 30° and 45° half-angle sharp cones because experimental data were available to guide model development. Care was taken to assure the generality of the approach so that application to lower cone angles of interest (near 10° half-angle) can be readily accomplished. The laser shadowgraphs presented in Reference 1 for 30° and 45° half-angle cones at a Mach number of about 13 show that normal shocks (or possibly strong oblique shocks) are set up between the rail and the cone. The model developed herein predicts the conditions under which the normal (or strong oblique) shocks will occur. Downstream of the normal or strong oblique shock, the flow is subsonic; but the pressure is higher than that experienced by the flow away from the rail which has undergone only compression by the conical shock attached to the cone. Therefore, that part of the flow downstream of the strong shock will expand and accelerate until the pressure of the gas which underwent the strong shock

reaches the pressure of the gas which was compressed by the
weak conical shock. The condition of the gas which first under-
went the strong shock and then expanded back to the pressure
corresponding to the pressure behind the attached conical shock,
is assumed to be approximately the conditions at the entrance
to the rail-projectile interface.

In actuality, the gas flow which is influenced by the
presence of the rail is highly three-dimensional since the in-
teraction of the conical shock with the rail is a local phenomenon
imbedded in the conical flow field. In Figure 6, some details of
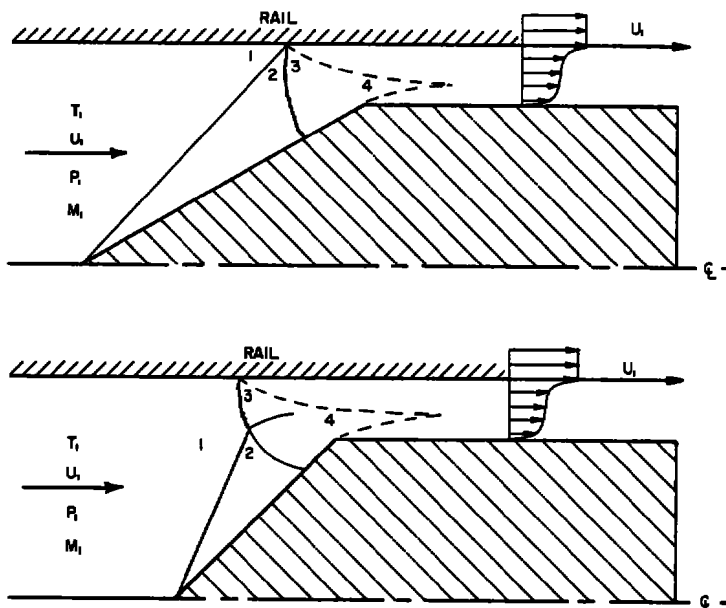
Figure 6. Shock System on 30° and 45° Cones Showing Definition
of Flow Regions.

the conical shock-rail interaction are shown. Point 3 refers
to the gas which has been compressed to a pressure over and
above the gas passing through the attached conical shock.
Surrounding this high pressure region is the lower pressure
region of gas, which is not influenced by the presence of the
rail. Point 2 refers to the state of the gas which only

experiences compression by the conical shock. The gas at Point
3, therefore, will tend to expand to the lower pressure region
of Point 2 where gas pressure is P_2. This expansion process is
assumed to be an isentropic expansion to the lower pressure.
The minimum pressure to which gas at Point 3 can expand is the
pressure corresponding to Point 2. Whether or not there is
sufficient distance between Point 3 and the entrance to the in-
terface for the gas at Point 3 to expand completely down to P_2
is not certain. For 30° and 45° half-angle cones, it is felt that
this assumption is fairly realistic. Under any circumstance,
the pressure at Point 2 is the minimum pressure which can be ex-
pected at the entrance to the interface region. Since the flow
field downstream of a conical shock is not a uniform flow field
(all properties are assumed constant along ray lines except for
entropy which is constant throughout the conical flow field down-
stream of the shock), a consideration must be made of the fact
that P_2 varies from one ray line to another in this conical flow
field. At the high Mach numbers considered here (M>10) nearly
all of the pressure increase occurs across the shock itself with
little extra pressure increase contributed by the turning of
the flow behind the conical shock. Thus, P_2 can be considered
to be constant in the conical flow region and can be taken to be
either the pressure just downstream of the conical shock or to
be slightly higher pressure adjacent to the cone surface.

During the early part of this investigation, it was
thought that a system of reflected shocks might be set up be-
tween the rail and the projectile much like the system of re-
flected shocks set up in a two-dimensional supersonic diffuser
formed by one parallel wall and one sloping wall forming a con-
vergent 2-D passage. If there could be a second reflection
(reflection at the cone surface of the shock reflected from the
rail), then this reflected shock would be highly curved since it
would be influencing gas which had already started to expand.

For the 30° half-angle cone traveling between Mach 10 and 15, it has been established that the second shock in the system (the first reflected shock from the rail) cannot undergo regular reflection at the cone surface as a weak oblique shock, but must be a strong oblique shock. Actually, this shock must have some curvature since the Mach number distribution just upstream of the second shock is non-uniform. Thus, for a 30° half-angle cone, the reflected shock at the rail is assumed to be a strong oblique shock. For the 45° half-angle cone, regular reflection of the conical shock itself is impossible in the Mach number range of 10 to 15. In this case, a normal shock is assumed for the flow near the rail.

Thus, for both 30° and 45° half-angle cones, a second reflected shock is not possible and the entire flow from Point 3 to the interface is expanding. In Section 5.3 it is shown that the strong shock assumption for the first (and only) reflected shock is indeed a very good assumption for 30° half-angle cones on the basis of total drag observations for 30° half-angle cones fired in Track K.

For smaller half-angle cones, regular reflection of the rail reflected shock impinging on the cone is theoretically possible although a reflected shock from the cone surface was not observed in the wind tunnel tests on 10° cones described in Reference 13. For a 10° sharp cone, the reflected shock off the rail is undoubtedly a weak nearly plane shock.[13] Between cone angles of 10° and 30° a rather dramatic change in the character of the reflected shock must take place. Figure 32 of Reference 1 shows a laser shadowgraph of a 30° cone. The authors of Reference 1 indicate on this figure the presence of a normal shock although it is not clear whether they are referring to a Mach reflection at the rail or that the reflected shock is nearly normal (a strong oblique shock) as we have assumed.

At some value of cone angle between 10 and 30 degrees, the gas dynamic conditions produced by shock reflections off the rail must change from those described by a weak shock solution

to those of a strong shock solution. The pressure at Point 3 (and thus the shock interference drag on the cone due to the presence of the rails) will be strongly dependent on how this transition in character of the reflected shock occurred. It is suspected that this transition in character might critically depend on the projectile Mach number as well as cone angle. A possible mechanism for the transition might be a Mach reflection of the rail-reflected wave at the cone surface, although neither this mechanism nor any other has been investigated as a part of this study. It might also be possible that there is actually a reflected wave from the cone surface for 10° cones, but it might not have been possible to observe the reflected shock in the Schlieren photographs of Reference 13 due to shock spreading and shock-boundary layer interaction, or the quality of the photographic reproduction.

A computer program was written which determines the flow conditions behind a normal shock, a series of oblique shock waves, or oblique shocks followed by either a strong oblique shock or a normal shock. After each shock in a system of shocks, the stagnation conditions, sonic conditions, and the conditions which would exist if the flow were isentropically expanded to the pressure existing immediately behind the first shock in the system are determined. Equilibrium air composition is assumed throughout these processes. The details of this computer program are presented in Section 3.4.

Some results of calculations with this computer program for 30° and 45° half-angle cones appear in Table 2. The numbering of states in Table 2 corresponds to the numbering in Figure 6. For 30° half-angle cones it is observed from the results in Table 2 that the flow conditions at the entrance to the interface correspond to supersonic flow when the assumption is made that $P_4 = P_2$ and that the rail reflected shock is a strong oblique shock. For the 45° cone, the Mach number M_4, is just slightly over one assuming a Mach reflection at the rail and subsequent isentropic expansion to P_2.

It should be emphasized that this computer program has sufficient flexibility that a number of hypotheses on the nature of the rail-cone shock interaction system can be tested.

3.3.2   Interface Sides

The sides of the interface region are open to the gas flow around the cylindrical portion of the projectile. The pressure in this region of the flow may be derived from the Prandtl-Meyer expansion of the gas around the shoulder of the cone-cylinder. The pressure along the sides of the interface is, therefore, defined by the pressure increase across the attached conical shock (or conical bow shock for a blunted cone) followed by the Prandtl-Meyer expansion through a turning angle equal to the cone half-angle.   The interface side pressures, P_5 are most informatively compared to the interface entrance pressures as tabulated in the last column of Table 2.

3.3.3   Interface Exit

The interface has an exit boundary at the trailing edge of the projectile. Determination of the pressure at the interface exit is perhaps one of the most challenging aspects of developing a model of the interface. If the interface flow could be considered to be two-dimensional, that is, if there were no circumferential pressure relief, the method used by Korkegi and Briggs could be used to estimate the exit pressure. They were able to determine the local pressure in the interface up to the point where the boundary layers on the rail and the projectile cylindrical surface merged to form a turbulent Couette flow region. After the mergence of the boundary layers, they assumed that the pressure remained constant with the flow at the exit, then expanding to the base pressure outside of the interface flow region.

TABLE 2. FLOW CONDITIONS NEAR RAIL AND AT ENTRANCE*

σ cone angle	M_1	P_1 atm	θ_1** deg.	δ *** deg.	U_1 m/sec	P_2/P_1 or P_4/P_1	U_2 m/sec	P_3/P_1	U_4 m/sec	M_4	ρ_4/ρ_1	T_4 °K	T_4^o °K	P_4^o/P_1
30°	10	1.0	33.57	27.20	3,470	36.54	2909	510	2410	2.42	3.91	2796	4498	587
30°	10	.1	33.57	27.20	3,470	36.54	2909	516	2385	2.41	3.90	2971	4229	588
30°	12	1.0	33.08	27.34	4,164	51.73	3507	821	2831	2.50	4.17	3653	5795	931
30°	12	.1	33.08	27.35	4,164	51.74	3507	832	2778	2.50	4.29	3507	5303	935
30°	14	1.0	32.64	27.40	4,858	69.33	4108	1221	3269	2.57	4.45	4418	7268	1377
30°	14	.1	32.64	27.40	4,858	69.49	4108	1251	3208	2.58	4.61	4114	6612	1399
30°	15	1.0	32.46	27.47	5,205	79.17	4409	1462	3498	2.60	4.57	4801	8015	1645
30°	15	.1	32.46	27.58	5,205	79.46	4408	1512	3437	2.60	4.75	4445	7236	1687
45°	10	1.0	4946	40.00	3,470	70.28	2286	124	1248	1.06	5.21	3935	4334	132.7
45°	10	.1	49.46	40.17	3,470	70.46	2286	125	1221	1.06	5.44	3695	4020	133.1
45°	12	1.0	48.88	40.57	4,164	100.70	2767	180	1446	1.06	5.70	4919	5458	191.5
45°	12	.1	48.88	40.91	4,164	101.3	2765	182	1405	1.06	6.0	4504	4976	191.2
45°	14	1.0	48.59	41.07	4,858	137.2	3241	246	1657	1.05	5.87	6086	6781	260.9
45°	14	.1	48.59	41.50	4,858	138.2	3238	247	1612	1.05	6.19	5623	6201	261.6
45°	15	1.0	48.30	41.09	5,205	156.6	3490	283	1769	1.06	5.93	6707	7421	300
45°	15	.1	48.30	41.52	5,205	157.8	3487	285	1715	1.07	6.28	6169	6722	301

*The flow regions denoted by the subscripts correspond to the numbering of the flow regimes shown in Figure 7. i.e. P_4^o refers to the stagnation pressure at condition 4.

** θ = angle between bow shock and trajectory.

*** δ = angle through which gas turns as it traverses bow shock.

TABLE 2. FLOW CONDITIONS NEAR RAIL AND AT ENTRANCE (Continued).

σ deg.	M_1	P_1 atm	θ_1 deg.	P_3/P_1	U_3 m/sec	U_1/U_3	ρ_3/ρ_1	ρ_{w_3}* gm/cm^3	ρ_{w_3}/ρ_3	T_3 °k	ρ_{w_4} gm/cm^3	ρ_{w_4}/ρ_4	MW_3**	P_{5/P_1}***
30°	10	1.0	33.57	510.8	604	5.75	34.06	.6007	14.99	4396	.043	9.34	28.3	1.58
30°	10	.1	33.57	516	575	6.03	35.67	.0607	14.46	4149	.0043	9.35	27.70	1.58
30°	12	1.0	33.08	821	665	6.26	40.62	.9651	20.192	5670	.0608	12.40	27.11	2.00
30°	12	.1	33.08	832	625	6.66	43.16	.0978	19.27	5203	.0061	12.15	26.07	2.00
30°	14	1.0	32.64	1221	748	6.50	45.75	1.436	26.68	7116	.0815	15.58	25.75	
30°	14	.1	32.64	1251	705	6.89	49.11	.1471	25.46	6494	.0082	15.04	24.63	2.43
30°	15	1.0	32.46	1462	789	6.59	48.33	1.719	30.23	7857	.0931	17.33	25.09	2.46
30°	15	.1	32.46	1512	739	7.04	52.7	.1778	28.67	7120	.0094	16.70	23.97	
45°	10	1.0	49.46	124	415	8.36	8.36	.1458	14.83	4290	.0827	12.79	27.90	2.66
45°	10	.1	49.46	125	393	8.83	8.83	.0147	14.15	3985	.00829	12.94	27.19	2.73
45°	12	1.0	48.88	180	457	9.10	9.10	.2119	19.79	5403	.1184	16.86	26.36	2.91
45°	12	.1	48.88	182	430.5	9.67	9.67	.0214	18.81	4930	.01191	16.88	25.37	2.98
45°	14	1.0	48.59	246	515	9.43	9.43	.2893	26.06	6715	.1614	23.3	24.87	
45°	14	.1	48.59	247	486	10.00	10.00	.0291	24.68	6151	.01625	22.32	24.00	3.95
45°	15	1.0	48.30	283	540	9.63	9.63	.3328	29.36	7357	.1842	24.95	24.19	4.11
45°	15	.1	48.30	285	505	10.32	10.32	.0335	27.71	6676	.0186	25.1	23.33	

*Subscript w denotes conditions defined at the temperature of the rail which is assumed to be at a temperature of 300°K.

**MW is the molecular weight of the air at state 3.

***State 5 denotes conditions at the sides of the interface (see Section 3.3.2).

For the purpose of this report, we have used the Reynolds number based on average gap height Re_h to serve as a guide in estimating the pressure at the exit. If the interface flow is laminar, that is, if Re_h is less than 10^3, the pressure in the interface is assumed to be constant at the entrance value. The procedure is justified on the basis of information given on pages 81-83 of Reference 8 where it is shown that, under conditions of extremely high values of U_∞, the flow in a parallel surface slider bearing with an imposed pressure gradient in the direction of flow is such that the pressure is constant at the initial value until at the very end of the bearing. Beyond that point, the pressure drops very rapidly to the surrounding value.

If the Reynolds number based on gap height lies between 10^3 and 10^5 the Korkegi and Briggs procedure is used. It is presumed that the boundary layers on the rail and the projectile will merge at some point along the interface and that the pressure in the interface will decrease continuously until the boundary layers merge, after which the pressure will remain constant until the end of the interface is reached. Because the width of the interface zone in the present problem (essentially the width of the rail) is not infinite as was presumed in the problem addressed by Korkegi and Briggs, the rate at which the pressure decreases in the region upstream of the merged boundary layers is taken to vary inversely with the ratio of rail width to length of the interface region.

If the Reynolds number based on gap height is larger than 10^5, it is presumed that the boundary layers have never merged and that the pressure in the gap decreases from the entrance pressure to the pressure existing along the sides of the interface at the very entrance to the interface region so that the pressure along the interface is presumed to be constant at the value fixed by the pressure existing on the cylindrical portion of the projectile which is not influenced by the presence of the rail.

41

3.3.4 Interface Walls

The interface is bounded by two solid walls--the rail and the projectile. Each of these walls presents a separate boundary condition for the problem.

The projectile passes rapidly over the rail so that any particular section of the rail is only in contact with the interface for a short time. This time is too short for significant heat to flow into any portion of the rail, or for appreciable temperature rise in the rail, so the rail will appear to be a cool constant temperature boundary.

The projectile surface remains in contact with the interface during the entire event. There can, therefore, be appreciable heat flow to the projectile and the temperature will only be limited by the heat capacity, thermal conductivity, and heat capacity associated with phase changes of the projectile material. For high heat fluxes, phase change dominates and the projectile surface temperature approaches the ablation temperature of the material. Strictly speaking, thermo-chemical equilibrium must be established and processes similar to those in an ablating boundary layer occur.

3.4 MATERIAL PROPERTIES

In this section the methods and procedures used to define the thermodynamic and transport properties of the various materials involved in the projectile-rail guide system are discussed. The material properties of interest are the gas in the system (air), the solid and vapor states of the projectile material, and the rail itself.

3.4.1 Air Properties

The thermodynamic properties of high temperature air are required in a convenient form in order to solve the normal and oblique shock equations for the high Mach numbers and cone angles associated with the projectiles. For a projectile running

into air initially at 300°K with a velocity of 4.6 km/s, the stagnation temperature reached by the air will be about 7500°K just prior to entering the interface. At temperatures below about 7500°K the primary species in dry equilibrium are O_2, N_2, O, N, NO, and Ar provided that the density of the air is no less than about one percent the density of air at standard conditions and no greater than about 100 times the density of air at standard conditions. In addition, the individual species comprising air still behave as ideal gases under these limits on temperature and density. Thus, the dissociation of O_2 and N_2 and the formation of nitric oxide (NO) can be used quite adequately to determine the composition and thermodynamic properties of equilibrium air within the above limitations on temperature and density.

Existing methods, procedures, and parts of computer programs available at UDRI which were originally developed for combustion of hydrocarbon fuels with air were used in conjunction with the elementary gas dynamic equations for normal and oblique shocks to produce a computer program which allows one to determine the thermodynamic and flow conditions downstream of a normal shock, an oblique shock, or a combination of oblique shocks followed by a normal shock. The program is very efficient both in terms of running time and central memory requirements. The running time is very short due primarily to a subroutine which determines initial guesses on the composition of the air to within 20 percent for each species.

An outline of a few of the details of the program follows. The key part of the program is a subroutine which solves for the equilibrium composition and thermodynamic properties of air at a specified temperature and pressure (EQAIR). The gas dynamic calculations are all carried out in the Subroutine GASDYN. The oblique shock equations are solved for a specified upstream Mach number temperature, pressure, and wedge half-angle. The oblique shock equations are written with the downstream temperature (T), pressure (P), and shock angle (θ_i) as the

independent variables. (The normal shock equations are just the
oblique shock equations with half-angle equal to zero and shock
angle equal to 90°.) Perfect gas oblique shock and thermo-
dynamic relations are used to provide initial estimates of T,P,
and θ_i. In order to carry out the Newton-Raphson procedures,
the thermodynamic derivatives $(\partial H/\partial T)_P$, $(\partial H/\partial P)_T$, $(\partial \rho/\partial T)_P$, and
$(\partial \rho/\partial P)_T$, where ρ is the density and H is the enthalpy, are
required. These quantities are determined in a separate sub-
routine. After T,P, and θ_i have been determined, the equilibrium
speed of sound, a, is calculated. The calculation of the speed
of sound is done in the subrountine SONIC which calculates the
derivative $(\partial n_i/\partial T)_s$ for each species where s is the entropy.
The speed of sound is calculated using the formula:

$$a^2 = (\partial P/\partial \rho)_s \tag{24}$$

Knowing T,P,θ_i and a, the remaining unknowns such as Mach number,
density, velocity, entropy, and enthalpy are then determined.
The program also contains a subroutine (CONSTS) which
performs isentropic compressions and expansions for equilibrium
air. This subroutine is used to determine stagnation pressures
and temperatures and is called by another subroutine PMEXP which
does Prandtl-Meyer expansions. A subroutine TRANSP is also
included which uses the equilibrium composition to determine
the viscosity and thermal conductivity of the equilibrium air.
This program facilitates the determination of interface
entrance conditions for any desired cone angle and Mach number
and provides boundary layer edge conditions at any location where
heat transfer calculations are needed.

3.4.2 Projectile Material Properties

Mass is deposited in the interface by the decomposition
of the slider contact surface. The interface gases are very hot
and the resulting heat flow to the slider surface is undoubtedly

large enough to cause ablation of the material. The mass loss rate, $\dot{m}_a$, is determined by the heat of ablation, L, the heat flux to the wall, $\dot{q}_w$, and the ablating (or contact) area, A_c;

$$\dot{m}_a = \dot{q}_w A_c / L. \tag{25}$$

If the length of the interface is B, then the ablative mass <u>per unit width</u> of gap is;

$$\dot{m}_a / W_r = \dot{q}_w B / L. \tag{26}$$

It is then necessary to evaluate $\dot{q}_w$ and L.

3.4.2.1 Heat of Ablation, L

The material of concern in this study is Lexan®, which is a polycarbonate material. The heat of ablation, L, is defined as;

$$L = \dot{q}_w / \dot{m}_a. \tag{27}$$

At steady state ablation;

$$L = \int C_p dT + \Delta L \text{ polymerization} + \Delta L \text{ vaporization}, \tag{28}$$

where;

$$C_p \quad = \quad 2.65 \text{ kJ/kg°K},$$

$$\Delta L \text{ vap} = \quad 0.68 \text{ MJ/kg}, \tag{29}$$

$$\Delta L \text{ poly} = \quad 0.98 \text{ MJ/kg},$$

or

$$L = 2.65 \times 10^3 \ (T - 295) + 1.66 \times 10^6 \text{ J/kg.*} \tag{30}$$

This equation is plotted in Figure 7.

®G.E. Trademark for polycarbonate.
*Private communication with Glen Ormbrek, AFML.
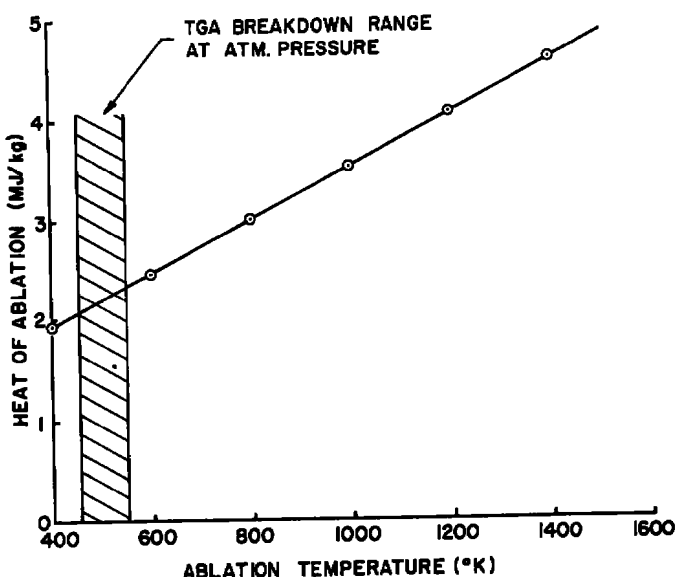
Figure 7. Heat of Ablation versus Ablation Temperature for Polycarbonate.

The ablation temperature of polycarbonate was found to be between 450°C and 550°C from a Thermal Gravametric Analysis (TGA) at atmospheric pressure. This would indicate a heat of ablation in the range of 2.1 to 2.3 MJ/kg. Laser ablation studies indicate a value of 3.76 MJ/kg (and a temperature of about 1100°K).* Other values are found in Reference 14 (5 MJ/kg) and Reference 15 (4.66 MJ/kg).

3.5 MODELS FOR DETERMINING FORCES AND WEAR FROM A FLUID DYNAMIC INTERFACE BETWEEN A PROJECTILE AND GUIDE-RAIL

Before presenting a description of the model developed for describing projectile/rail interface regions, a few words are in order concerning some practical constraints imposed upon the computational approaches. Ideally, it would be desired to use solutions to the Navier-Stokes equations to determine the pressure, temperature, and viscous stress distributions which

---

*Private communication with Glen Ormbrek, AFML.

exist in the interface fluid in order to determine the forces, moments, and wear (ablation) on the projectile. However, the time required to perform these computations would not be compatible with the present problem even if computer programs were available which could perform the necessary computations since these computations need to be performed thousands of times during analysis of a single passage of a projectile through the rail system. The same comment applies to the Reynolds lubrication equation which is very difficult to solve for all but the simplest cases. Also, the lubrication Reynolds number can be expected to be of order one only when the average gap height is extremely small because of the extremely high projectile velocities. Thus, the lubrication model can be applied for only those cases where a rail-projectile collision is imminent or when extremely small clearances exist between the rail and projectile. As will be shown later in this section, a gap height small enough for the laminar flow lubrication model to apply to the present problem is smaller than can be realized physically (in the range of hundreds of nanometers).

3.5.1 Boundary Layer Considerations for the Interface Flow

As was mentioned in Section 3.2.1, boundary layers develop on both the rail and the projectile surface upstream of the interface (see Figure 3). A boundary layer begins to develop on the rail at the point where the conical shock intersects the rail and the boundary layer on the cone begins to develop at the tip of the cone. The boundary layer on the conical portion of the projectile also undergoes a classical boundary layer-shock interaction at the point on the cone where the reflected shock from the rail intersects the cone. At the juncture of the conical portion of the projectile with the cylindrical portion, the projectile boundary layer undergoes another change as the flow on the projectile surface turns to enter the interface region. The character of the rail and projectile boundary layers in the region just upstream of the interface can have a strong

influence on the nature of the flow in the interface itself.
For instance, if these two boundary layers have not merged at
the entrance to the interface, then an inviscid core exists be-
tween the two boundary layers, and the initial behavior of the
flow in the interface is dominated by gas dynamic considerations
up to the point in the interface where the separate boundary
layers become fully merged. After mergence, the interface flow
is dominated by viscous effects. If the gap height is sufficiently
large, it is possible, of course, that the two boundary layers
never merge. If, on the other hand, the two boundary layers
merge upstream of the interface, then the flow throughout the
interface is dominated by viscous effects.

Because the work of Korkegi and Briggs comes closest
of any available treatment to describing the boundary layer as-
pects of the problem at hand, it bears close consideration.
Korkegi and Briggs studied the interface region of a hypersonic
slipper bearing on rocket-boosted sleds guided by rails.[12,16]
Figures 8 through 11 describe the basic features of the problem
they addressed and the idealizations of their flow model.
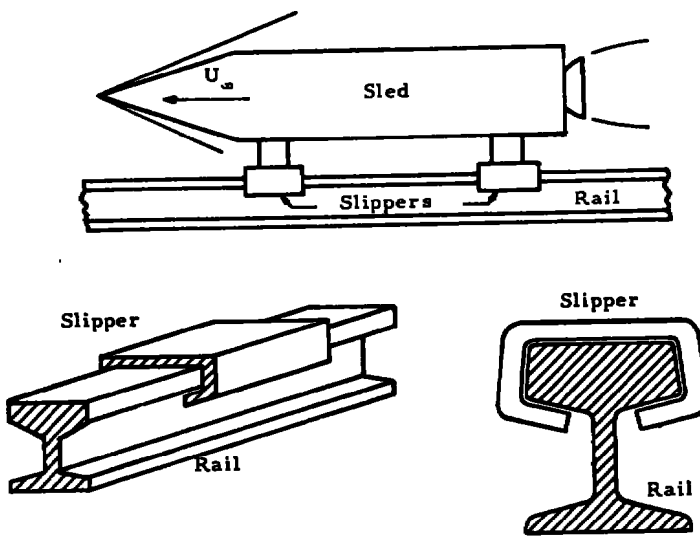
Figure 8. Typical Rocket Sled Configuration and Slipper Details.
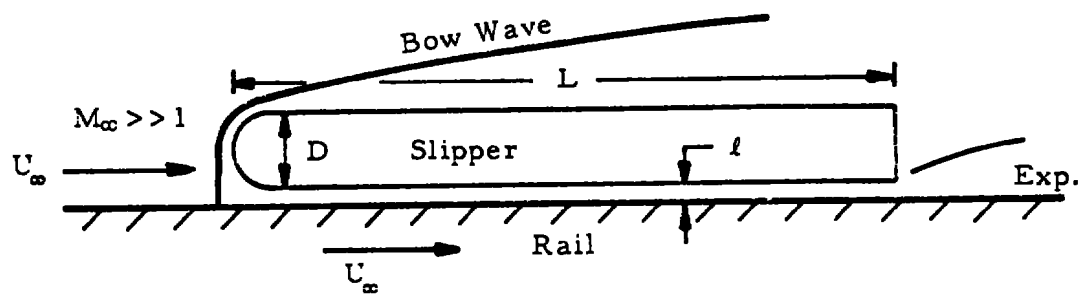
Figure 9. Slipper Cross Section.

a) Probable

b) Assumed
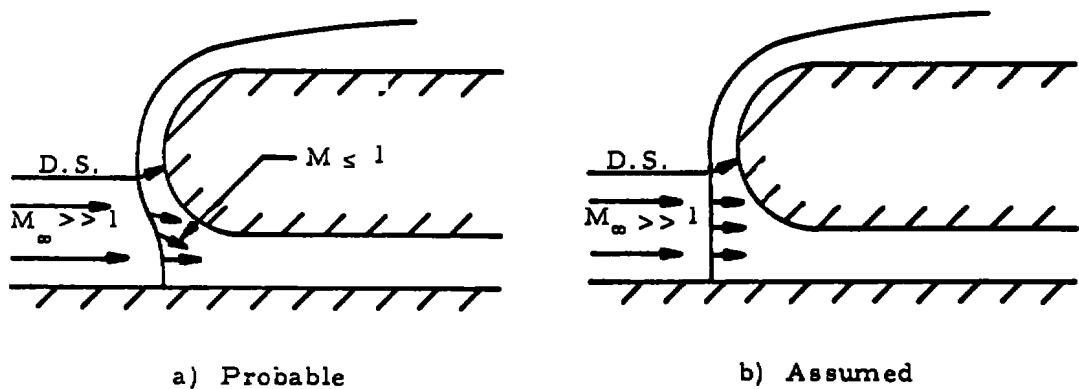
Figure 10. Bow Shock Wave.
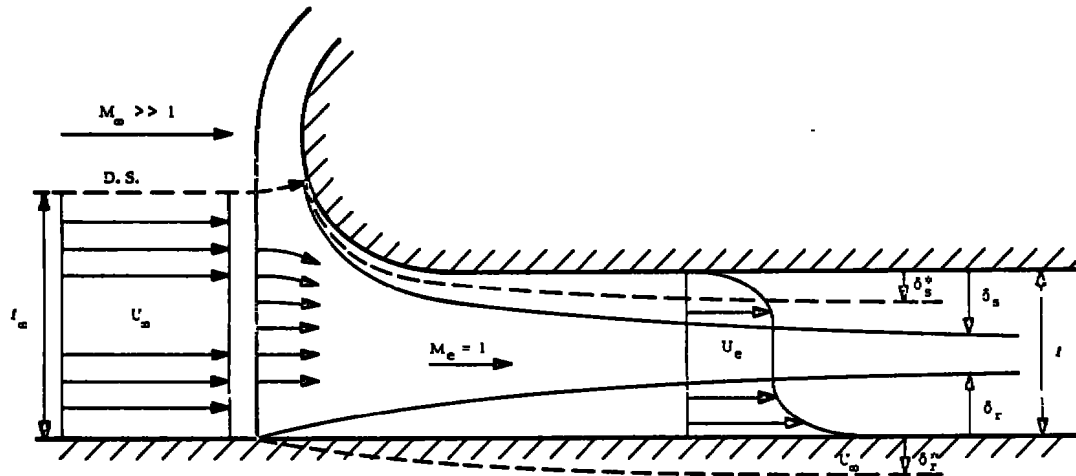
Figure 11.   Boundary Layer Growth in Gap.

In Reference 16 many simplifications were made on the
sled-slipper motion problem such as assuming: a steady state
configuration; locally two-dimensional flow; and that the flow
model consists of a laminar stagnation region at the leading
edge of the slipper followed by separate turbulent boundary layers
on slipper and rail (shock tube type) eventually merging into
a full shear layer which tends toward a Couette flow asymptote.
The inlet shock structure was determined to be dependent upon:
the shape of the leading edge of the slipper; the ratio of gap
height to slipper thickness; and the mass flow through the gap
which, in turn, dictates the location of the dividing streamline
separating the flow entering the gap from that going over the
slipper.   The mass flow was found to be dependent on the pressure
field generated by the shock compression.   Hence, the mass flow
and shock structure were considered coupled.   In the sled-slipper-
track problem, the gap heights were much smaller than the blunt
slipper leading edge; thus, it was assumed that the bow wave was
normal between the dividing streamline and the rail, so that all

the flow entering the gap was compressed through a single normal shock as shown in Figures 8 through 11.

One of the major differences between the slipper/rail problem and the projectile/rail problem is that slender nose cones will create a Mach reflection of the bow wave on the rail rather than the single normal shock. If the semi-cone angle becomes large, i.e., >45° the assumption of a single normal shock at the gap entrance would be reasonable; however, three-dimensional pressure relief is present along the projectile-rail interface. The single most important difference between the slipper/rail problem and the projectile/rail problem is the fact that in the slipper/rail problem, two-dimensional flow could reasonably be presumed to exist over the interface, whereas in the projectile/rail problem the two-dimensional assumption is never strictly valid, and grossly misrepresents the flow situation when the boundary layers in the flow have not merged to form a viscous dominated flow region.

While the entire interface model of Korkegi and Briggs is not applicable to the projectile/rail problem, some of the thinking that went into their model is applicable. In addition, their work on fully developed turbulent Couette flow is directly applicable. In principle, their basic approach to determine both the point in the interface where the boundary layers merged and the pressure distribution upstream of the mergence point can be used to advantage in the rail/projectile problem. They calculated the displacement thicknesses of the two boundary layers which defined the boundaries of a two-dimensional flow channel and then used isentropic flow gas dynamic considerations to determine the pressure distribution along the flow channel or interface. Because they assumed two-dimensional flow, their model was relatively straightforward to implement. In the present problem their procedure would have to be considerably altered to account for the pressure relief afforded by the circumferential flow from the center of the interface to the sides of the interface.

No detailed computations of the displacement thicknesses
were attempted in the present analysis because of the difficulty
involved in performing such calculations for three-dimensional
boundary layers. No simple formulations exist for determining
the displacement thickness of three-dimensional boundary layers.
Therefore, no effort was made to develop a rigorous method for
determining the exact point of mergence of the rail and projectile
boundary layers. Instead, a simple application of the results
of Korkegi and Briggs was made tempered with the fact that
pressure distribution upstream of the mergence point is adjusted
such that the pressure in the interface rapidly achieves equilibration
with the pressure existing along the sides of the interface when-
ever the boundary layers have not already merged upstream of the
interface. The results of computations of the rail boundary
layer are given in the next paragraph in order to provide some
insight into the conditions under which mergence of the boundary
layers upstream of the interface region could be expected.

3.5.2 Rail Boundary Layer Computations

From the data given in Table 2 some basic boundary layer
properties were calculated for the boundary layer which develops
along the rail having its leading edge at the juncture of the
strong shock and the rail. The purpose of these boundary layer
calculations was to determine whether this boundary
layer is a laminar or turbulent boundary layer by the time it
reached the entrance of the gap, and also to determine the thick-
ness of the boundary layer at the entrance to the gap. Knowledge
of the boundary layer thickness and Reynolds number at the en-
trance to the gap allows one to determine the conditions under
which the flow at the gap entrance could be expected to have a
significant uniform velocity region (an inviscid core) and whether
or not the shear flow region could be expected to already be
turbulent. If the boundary layer thickness is greater than the gap
height, no significant uniform mean flow region exists at the
gap entrance, and the flow in the entire gap length can be

considered viscous dominated with little pressure relief along
the interface. If, at the same time, the shear flow region
at the gap entrance is laminar, then the initial portion of the
interface flow region can be expected to be laminar regardless
of the laminar or turbulent state achieved well into the gap.
Conversely, if the boundary layer is already turbulent at the
entrance to the gap, then the flow in the interface region could
have one of two different basic characteristics depending on the
Reynolds number of the interface flow, Re_h. If Re_h is such that
the basically Couette flow is turbulent, then the entire in-
terface flow regime can effectively be considered to be a tur-
bulent Couette flow. If Re_h is such that the Couette flow is
laminar, then the initial turbulence will be damped out and the
entire interface flow will effectively be laminar.

Listed in Table 3 are the boundary layer characteristics
expected at the entrance to the gap. Before discussing these
results, the nomenclature of the table quantities must be de-
fined. The column listed as Δx represents the distance along the
rail from the strong shock to the gap entrance. The tabulated
values of Δx are calculated based on a zero gap height, h, and
for a projectile diameter of 41 mm. If h becomes a significant
fraction of the cone radius, then Δx will become smaller than
the tabulated values. As indicated in Table 3, the values of
Δx for a 45° half-angle cone are estimated values based on the
laser shadowgraph presented in Figure 30 of Reference 1. The
precise location of the juncture of the conical shock and the
strong shock cannot be easily calculated. Therefore, recourse
was made to estimation from the laser shadowgraph. The kine-
matic viscosities ν_w at the rail tabulated in Table 3 were
calculated at a temperature of 300°K using the pressure at either
point 3 or 4 (defined in Figure 6) as the case may be. The
dynamic viscosity of air at 300°K was taken to be 1.8×10^{-4}
gm/cm-sec and the perfect gas law was used to calculate the
density of the air at the rail. The column listed as y_δ gives
the laminar boundary layer thickness based upon the point in

53

TABLE 3. BOUNDARY LAYER CHARACTERISTICS FOR CONE PROJECTILES TRAVERSING GUIDE-RAILS.

σ cone angle	M_1	P_1 atm	Δx cm	$\nu_{w3} \times 10^4$ cm²/sec	$\nu_{w4} \times 10^4$ cm²/sec	$\dfrac{U_1}{U_4}$	$y_\delta \times 10^3$ cm	$\mu_4 \times 10^4$ gm/cm-sec	$\rho_4 \times 10^3$ gm/cm³	$\nu_4 \times 10^2$ cm²/sec	$R_{\Delta x} \times 10^{-5}$	$Re_h \times 10^{-5}$	MW_4
30°	10	1.0	.457	3.0	41.9	1.44	2.36	7.43	4.602	.162	1.31	2.1	28.91
30°	10	.1	.457	30.0	419	1.45	7.50	7.68	.4594	1.67	.135	.21	28.80
30°	12	1.0	.401	1.87	29.6	1.47	2.27	9.11	4.905	.186	1.35	3.6	28.43
30°	12	.1	.401	18.4	295	1.50	7.09	8.39	.5007	1.68	.165	.36	27.85
30°	14	1.0	.348	1.25	22.1	1.49	2.14	9.67	5.234	.185	1.45	5.58	27.37
30°	14	.1	.348	12.2	220	1.51	6.57	9.12	.5435	1.68	.176	.56	26.41
30°	15	1.0	.325	1.05	19.3	1.49	2.07	10.4	5.374	.194	1.40	6.85	26.75
30°	15	.1	.325	10.1	192	1.51	6.37	9.70	.5596	1.73	.171	.69	25.70
45°	10	1.0	↑	12.3	21.8	2.78	4.00	8.92	6.130	.146	18.97	4.04	28.17
45°	10	.1		122	217	2.84	12.91	8.63	.6402	1.35	2.15	.404	27.56
45°	12	1.0	.7	8.5	15.2	2.88	4.09	10.2	6.661	.154	23.2	6.96	26.71
45°	12	.1	(estimated from	84.1	151	2.96	13.10	9.77	.7057	1.38	2.75	.670	25.75
45°	14	1.0	Fig. 30	6.22	11.1	2.93	4.51	11.76	6.920	.170	25.5	11.1	25.19
45°	14	.1	of Ref.1)	61.9	111	3.01	13.86	11.29	.7281	1.55	2.95	1.11	24.31
45°	15	1.0		5.4	9.77	2.94	4.39	12.48	6.980	.179	26.10	13.5	24.54
45°	15	.1	↓	53.7	96.8	3.03	14.11	11.84	.7388	1.60	3.11	1.37	23.71

the boundary layer where the velocity is within one percent
of the free-stream value. Values for y_δ were calculated from
results presented in References 17, 18, and 19. The boundary
layer thickness was estimated using the following relation;

$$y_\delta = G \ (U_1/U_4, \ T_{w_4}/T_4)\sqrt{\frac{2\Delta x \nu_{w_4}}{U_4} \ \frac{\rho_{w_4}}{\rho_4}} \ . \tag{31}$$

G was taken to be 2.0 based primarily on the results presented in
Reference 17 for values of U_1/U_4 ranging from 2 to 4. The values
of T_{w_4}/T_4 for 30° half-angle cones do not correspond to values
of T_{w_4}/T_4 obtained for a single normal shock so that G can be
off by perhaps as much as 20 percent. The Reynolds number $R_{\Delta x}$
listed in Table 3 is defined in the following way;

$$R_{\Delta x} = \frac{(U_1 - U_4)^2 \ \Delta x}{U_4 \ \nu_4} \ . \tag{32}$$

This is the appropriate Reynolds number to use for determining
the transition Reynolds number for boundary layers formed by a
moving shock wave (References 19, 20, 21). The dynamic viscosity
ν_4 was determined from Reference 22.

The last column of Table 3 gives the Reynolds number of
the interface flow, Re_h, based on the following definition;

$$Re_h = \frac{U_1 h}{\nu_{w_4}} \ . \tag{33}$$

where U_1 is equal in magnitude to U_∞. A value of h of 25.4 μm
was used to define Re_h.

The results presented in Table 3 provide the following
insights: (1) the thickness of the boundary layer for $P_1=1$ bar
is on the order of 25 μm, (2) if the gap height is significantly
greater than 25 μm, a uniform mean flow region will exist and
the problem becomes similar to that treated by Korkegi and Briggs,

(3) the boundary layer Reynolds number, $Re_{\Delta x}$, for 30° half-angle
cones is well below the transition Reynolds number range of
1 to 10 x 10^6 for this type of boundary layer[11, 21] so that the
boundary layer on the rail at the entrance to the interface flow
region is always laminar, and (4) the interface flow Reynolds
number based on gap height is at least an order of magnitude
greater than the commonly accepted value of transition Reynolds
number of 1 to 4 x 10^3. Thus, only for gap heights smaller than
2.5 um could completely laminar Couette flow be expected in the
interface.

Thus, the following conclusions can be drawn based on
the preceeding analysis:

(1) Laminar Couette flow should not be expected to
     occur unless gap heights of less than 2.5 μm
     are to be considered.

(2) For gap heights in the range of 2.5 μm to about
     25 μm turbulent Couette flow can be expected over
     the entire interface flow regime.

(3) For gap heights significantly greater than about
     25 μm, the flow in the initial portion of the
     interface region will contain a basically uniform
     core which implies that gas dynamic considerations
     need to be included in the interface flow analysis.

The interface flow situation then becomes one of two separate
boundary layers developing one on the rail, and one on the
projectile with a bulk flow between the two boundary layers.
The behavior of the bulk flow becomes quite sensitive to the
shapes of the developing boundary layers. For large gap heights,
the bulk flow will also be influenced by the circumferential
pressure gradient between the center of the rail and the edge
of the rail. Because a circumferential pressure gradient was
not included in Korkegi and Briggs analysis of a hypersonic
slipper bearing, the direct application of their approach to the
present problem is not possible.

3.5.3   Simplified Fluid Dynamic Models

Based on the results of the previous section, it is
clear that three basic flow models are needed to describe the
interface phenomena in order to provide complete coverage of
the entire Reynolds number range from 0 to ∞. For the Reynolds
number range of $0<\mathrm{Re}_h \leq 1 \times 10^3$, the laminar Couette flow model is
used. For the Reynolds number range of 10^3 to 10^5 the turbulent
Couette flow mode of Korkegi and Briggs[23,24] is used. For
Reynolds numbers greater than 1×10^5 the projectile boundary
layer is presumed to be a fully turbulent boundary layer acting
as if no rail were present. The methods used to implement the
above three models, including the effects of: non-parallel
boundaries; ablation or wear; pressure buildup; and the forces
and moments on the projectile, are discussed in Section IV.

3.6   PROJECTILE MATERIAL DEFORMATION

During the initial time period of this investigation it
was assumed that elastic deformation of the projectile material
would not be important. The gap heights were expected to be on
the order of 25.4 μm (0.001 in.). Thus, the maximum possible
angular rotation of the projectile and consequently the normal
forces and aerodynamic moments associated with rotation of
the projectile were expected to be insignificant compared to the
normal forces and moments due to interfacial forces. However,
as test results became available, it was apparent that initial
gap heights were much greater than 25 μm (see footnote on page 3).
Analyses of the forces required to keep the projectile within the
confines of the rails with the larger than anticipated rotation
of the projectile showed that pressures in the interfacial region
were such that elastic deformation of the projectile would be an
important phenomenon. Thus, the fluid dynamic processes in the
interfacial region are not just simply hydrodynamic, but rather
elastohydrodynamic in nature.

SECTION IV

COMPUTER SIMULATION OF
PROJECTILE-RAIL INTERACTION PHENOMENA

In this section we describe the methods, procedures, and equations that are used in the Projectile Dynamics Computer Program to compute the forces, moments, and ablation of the projectile due to the presence of a rail. The computations are carried out individually for the top rail, the bottom rail, and the two side rails and then the net quantities are determined. This section also describes the methods used to determine those aerodynamic forces and moment coefficients which are calculated in the program. This section consists of three subsections. Section 4.1 describes how the zero angle-of-attack total drag coefficient, C_{D_O} is calculated. This quantity includes the contribution of the shock interaction drag to the total drag, but does not include drag due to interface forces. Section 4.2 describes subroutine INTER, in which the interface effects on the projectile are determined. These effects are the viscous shear forces, the normal forces (pressure forces), and the ablation rates. The moments on the projectile due to both interface forces and shock interaction forces are also computed by INTER.

4.1   COMPUTATION OF C_{D_O}

In this section we describe the methods used to determine the drag coefficient C_{D_O} which includes drag due to aerodynamic and shock interaction effects. In essence, this section is a description of subroutine DRAGCO. The factor C_{D_O} is defined as;

$$C_{D_O} = C_{D_P} + C_{D_v} + C_{D_b} + C_{D_{SI}} .$$
(34)

58

The first three components of C_{D_0} are standard aerodynamic drag coefficients; namely, pressure drag on the forebody of the projectile, viscous drag on the entire projectile, and base drag. The reference area used to define C_{D_0} is the base area of the projectile.

4.1.1 Pressure Drag, C_{D_P}

Two different equations for C_{D_P} are used in subroutine DRAGCO. Both are valid for blunted or sharp cones. The first equation for C_{D_P} is taken from Reference 25 and is valid for Mach numbers in the range of 5 to 25, cone half-angles up to 15° and blunted ratio, ζ, defined as the nose-tip radius, r_n, divided by the base radius of the cone, r_b, from 0 to 0.3;

$$C_{D_P} = C_1 \sin(\zeta)^{C_2} + \frac{C_3}{\sigma C_4} (\zeta)^{C_5} \, , \qquad (35)$$

where;

$$
\begin{aligned}
C_1 &= 1.944 + 1.872/M - 17.0/M^2 + 38.19/M^3, \\
C_2 &= 1.931 + 0.8635/M - 8.063/M^2 + 12.21/M^3, \\
C_3 &= 11.433 + 34.96/M - 921.5/M^2 + 2607.3/M^3, \\
C_4 &= 0.5359 + 0.09964/M + 10.769/M^2 - 104.21/M^3 \\
&\quad + 209.43/M^4, \text{ and} \\
C_5 &= 3.296 + 2.997/M - 74.378/M^2 + 154.67/M^3.
\end{aligned}
$$

If the above equation is not applicable then the following, less accurate equation for C_{D_P}, based on Newtonian theory of hypersonic drag is used

$$C_{D_P} = \frac{C_{Pmax}}{2} \left[(1 - \frac{\zeta^2}{2} \cos^2\sigma)(2 \sin^2\sigma) + \zeta^2 \cos^2\sigma \right] \, , \qquad (36)$$

where C_{Pmax} for Mach numbers greater than 6 has the value of 1.83 for air.

4.1.2 Viscous Drag, C_{D_V}

The viscous drag is the total of the contributions of skin friction drag on the projectile forebody and the cylindrical portion of the projectile. Both of these contributions are computed from the same basic skin friction coefficient formulation based on a turbulent flow skin friction formula for incompressible flow and corrected to compressible flow conditions by the reference enthalpy method.[26]

The drag coefficient for the cylindrical portion of the projectile then becomes;[13]

$$\left(C_{D_V}\right)_{cone} = \frac{0.0776 \ B_c}{\left(Re_{\ell_s}\right)^{0.2}} \left(\frac{U_e}{U_\infty}\right)^{1.8} \left(\frac{P_e}{P}\right)^{0.8} \left(\frac{T_\infty}{T_e}\right)^{0.58} \left(\frac{H_e}{H^*}\right)^{0.58}$$

$$\cot \sigma \ , \tag{37}$$

where Re_{ℓ_s} is the Reynolds number based on free stream conditions and the slant length of the cone. H^* is the Eckert reference enthalpy given by;[13]

$$\frac{H^*}{H_e} = 0.5 + 0.5 \ (T_w/T_e) \ (T_\infty/T_e) \ + 0.374 \ M_e^2 \tag{38}$$

The subscript e in the above equations denotes conditions evaluated just outside the boundary layer on the cone. This would correspond to conditions evaluated at state 2 in Table 2. Conditions at state 2 are evaluated in subroutine GASDYN. The subscript ∞ in the above equations refers to free stream conditions and this denotes conditions at state 1 in Table 2. B_c in the above equations is a blowing correction to account for mass addition to the boundary layer due to ablation. B_c is evaluated from a curve fit to data given in Figure 18 of Reference 13. The skin friction drag coefficient for the cylindrical portions of the projectile is given by;

$$\left(C_{D_v}\right)_{cyl} = \frac{0.074 \ B_c}{(Re_B)^{0.2}} \left(\frac{U_5}{U_\infty}\right)^{1.8} \left(\frac{P_5}{P_\infty}\right)^{0.8} \left(\frac{T_\infty}{T_5}\right)^{0.58} \left(\frac{H_5}{H^*}\right)^{0.58} \left(\frac{2B}{r_b}\right), \quad (39)$$

where B denotes the length of the projectile afterbody, Re_B denotes the Reynolds number based on the length B, and subscript 5 denotes conditions existing just outside the boundary layer on the projectile afterbody. Conditions at state 5 are evaluated in the Prandtl-Meyer expansion subroutine PMEXP. The last term in Equation (39) accounts for the use of the base area of the projectile as the reference area in defining the drag coefficient.

4.1.3 Base Pressure Drag, C_{D_B}

The following expression for base pressure drag was taken from Reference 13;

$$C_{D_B} = \frac{1.43}{M_\infty^2} \ [1 - (P_b/P_e) \ (P_e/P_\infty)] \ , \quad (40)$$

where P_b/P_e is evaluated from a curve fit to data given in Figure 19 of Reference 13. P_b is the base pressure and P_e is defined as in Section 4.1.2.

4.1.4 Shock Interaction Drag, $C_{D_{SI}}$

The basic expression used to define $C_{D_{SI}}$ is given by;

$$C_{D_{SI}} = \frac{4 \ W_r \Delta x_{SI} \sin \sigma (P_{SI} - P_e)}{1/2 \rho_\infty \ U_\infty^2 \ A_b} \ . \quad (41)$$

Δx_{SI} is the distance from the base of the conical forebody to the point on the cone where the rail shock intersects the cone surface, measured along the cone surface. P_{SI} represents the average pressure existing on the cone surface over the rail shock interaction region of length Δx_{SI}. $W_r \Delta x_{SI} \sin \sigma$ in Equation (41) represents the projected area normal to the x axis over which the average pressure increase due to the rail shock interaction $(P_{SI} - P_e)$ acts. Note that $P_{SI} - P_e$ is used in Equation (41) rather than P_{SI} since the drag force in the x-direction due the pressure P_e has already been accounted for in the expression for C_{D_p}. The factor 4 in Equation (40) accounts for the existence of four rails. A correction factor having a value

greater than unity should probably be applied to Equation (40) whenever the rail-projectile shock interaction is a weak shock interaction to account for the fact that the pressure immediately downstream of the point of intersection of the shock with the projectile is higher than the pressure in the region adjacent to the shock interaction region. For a weak shock interaction the velocity of the gas in the high pressure zone is still supersonic. Thus, a complicated three-dimensional shock system will be present which will cover an area somewhat greater than that given by $W_r \Delta x_{SI}$. A first approximation to this correction factor could be obtained from a loose analog to the two-dimensional problem of two parallel supersonic streams at different pressures suddenly confronting each other. An example of this type of problem is given on page 480 of Reference 26 from which it is clear that the high pressure region will expand outward toward the low pressure region and this expansion occurs such that the average pressure times the affected area is larger then the pressure of the high pressure stream times just the area covered by the high pressure stream. The determination of this correction factor was not attempted in the course of this effort.

The geometric conditions for an attached shock on a sharp cone are shown in Figure 12. The reflection angle of the shock reflecting off the rail, θ_r in Figure 12, is determined in subroutine GASDYN for a sharp cone. Δx_{SI} is calculated from the following formula obtained from a geometric analysis of Figure 12;

$$\Delta x_{SI} = \frac{r_b}{\sin \sigma} - \frac{(r_b + h)}{\sin \theta_s} \frac{\sin(\theta_s + \theta_r)}{\sin(\sigma + \theta_r)} . \tag{42}$$

The shock interaction pressure P_{SI} is a quantity which has not been defined rigorously in the present effort: In section 3.3.1 we discuss the basic difficulty in trying to define the exact nature of the rail shock interaction. Certainly the pressure existing over the length Δx_{SI} is not constant since the
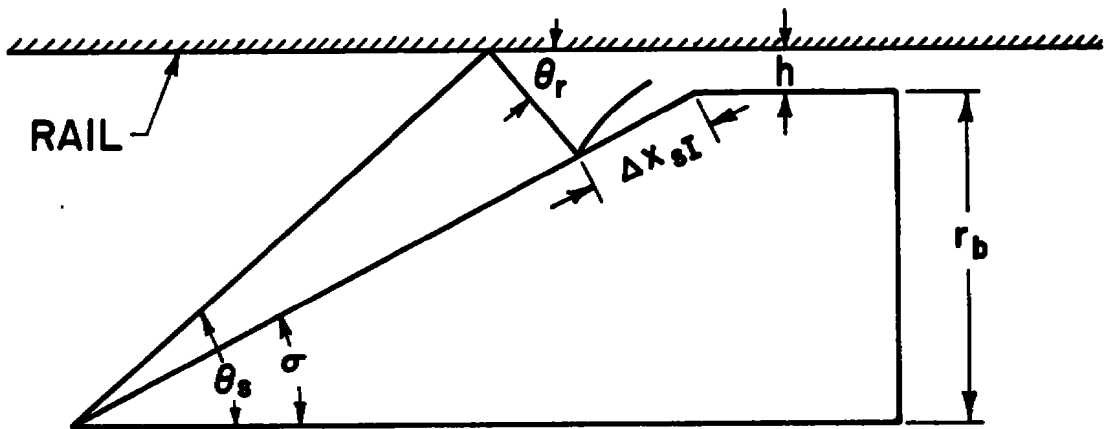
Figure 12. Sketch Showing Definition of Shock Interaction
            Distance Δx_{SI}.

flow will expand outward from the high pressure region. Then
there is the question concerning the number of weak reflected
shocks which can exist between the rail and the projectile for
those situations where the reflected shock from the rail is a
weak shock. The present best estimate of the authors is that,
for slender cones, the rail shock impinging on the cone will
experience a more or less regular reflection at the cone sur-
face, but the shock reflecting off the cone will probably not
penetrate back to the rail since it will be diminished in
strength as it moves into gas which itself is expanding out-
ward in a direction parallel to the rail surface but perpendi-
cular to the direction of motion of the projectile. On this
basis, perhaps the best approach to follow in defining P_{SI} for
slender cones would be to use an average pressure obtained for
the case of no reflection from the cone surface and the pressure
obtained for the case of a regular reflection at the cone surface.

The program is set up such that the user can specify the total number of reflected waves which he wants to consider (up to a total of 4). In determining the value of P_{SI}, the program will use the pressure existing behind the first reflected shock (conditions behind the first reflection from the rail, e.g., P_3 in Figure 6) if the user calls for one reflected shock, and will use the pressure existing behind the second reflected shock if two reflected shocks are specified. If more than two reflected shocks are called for, the program will compute the thermodynamic and flow conditions behind each of the reflected shocks, but will use the pressure behind the second shock as P_{SI}.

In concluding this paragraph, it should be mentioned that Appendix B contains a description of the input data required to operate the program and a description of the individual subroutines which comprise the total program.

4.2   FORCES, MOMENTS, AND ABLATION DUE TO THE INTERFACE

In this section we describe subroutine INTER. The sequence of computations in this subroutine is presented below.

- (1)   Gap heights at the front and rear of the interface on each rail (top, bottom, and side) are read from COMMON. An average gap height and a minimum gap height for each of these three interfaces are then computed and stored.

(2)   Reynolds numbers based on these average and minimum gap heights are then computed and stored.

(3)   Viscous shear forces (tangential forces on the projectile) are then computed followed by computation of ablation rates. One of the three fluid dynamic models discussed in Section 3.5 is used to determine an average skin friction coefficient for the interface depending on the value of the Reynolds number based on gap height or (if the projectile axis is not parallel to the rail) the Reynolds number based on the minimum gap height. Through the use of Reynolds analogy for heat and momentum transfer, an appropriate heat transfer coefficient is then computed followed by computation of the ablation rate.

(4) Normal forces due to the pressure distribution in the interfaces are computed along with the moments caused by these normal forces.

(5) Normal forces due to the rail shock interaction are computed along with the moments caused by both the normal and tangential components of the rail shock interaction forces.

(6) The net forces in the tangential and normal directions are then computed along with the net moment about the pitching axis.

The reader will observe that some effects of the rail shock interaction are included in this subroutine. The reason for this is that the net normal force and the net moment about the pitching axis both are sensitive to the position of the projectile relative to the rails. From Equation (41) it is observed that Δx_{SI}, and thus the shock interaction force, is a function of gap height. For slender cones in particular, Δx_{SI} is sensitive enough to small changes in the gap height, h, that the effect of variations in h must be included in determinimg the net normal force and the net moment. The net tangential force, however, is not sensitive to h and this effect is already included in the total zero-angle-of-attack drag coefficient.

Track G projectiles wear data became available near the end of this effort. Relatively large rotations of the projectile were found to occur ($5°$ to $7.5°$ at 6000 m/s and 1 atm.) The rotation of the projectile as well as the gap height affect Δx_{SI}. Figure 13 shows how Δx_{SI} is defined when the projectile is rotated through an angle θ. P_{SI} as well Δx_{SI} depends on h and θ. The variation of both Δx_{SI} and P_{SI} with h and θ were included in the procedures for determining the overall net forces and moments on the projectile. The details of these procedures are found in Section 4.3.

In the following paragraphs, the equations used to reflect the physics of the three fluid dynamic models are discussed.
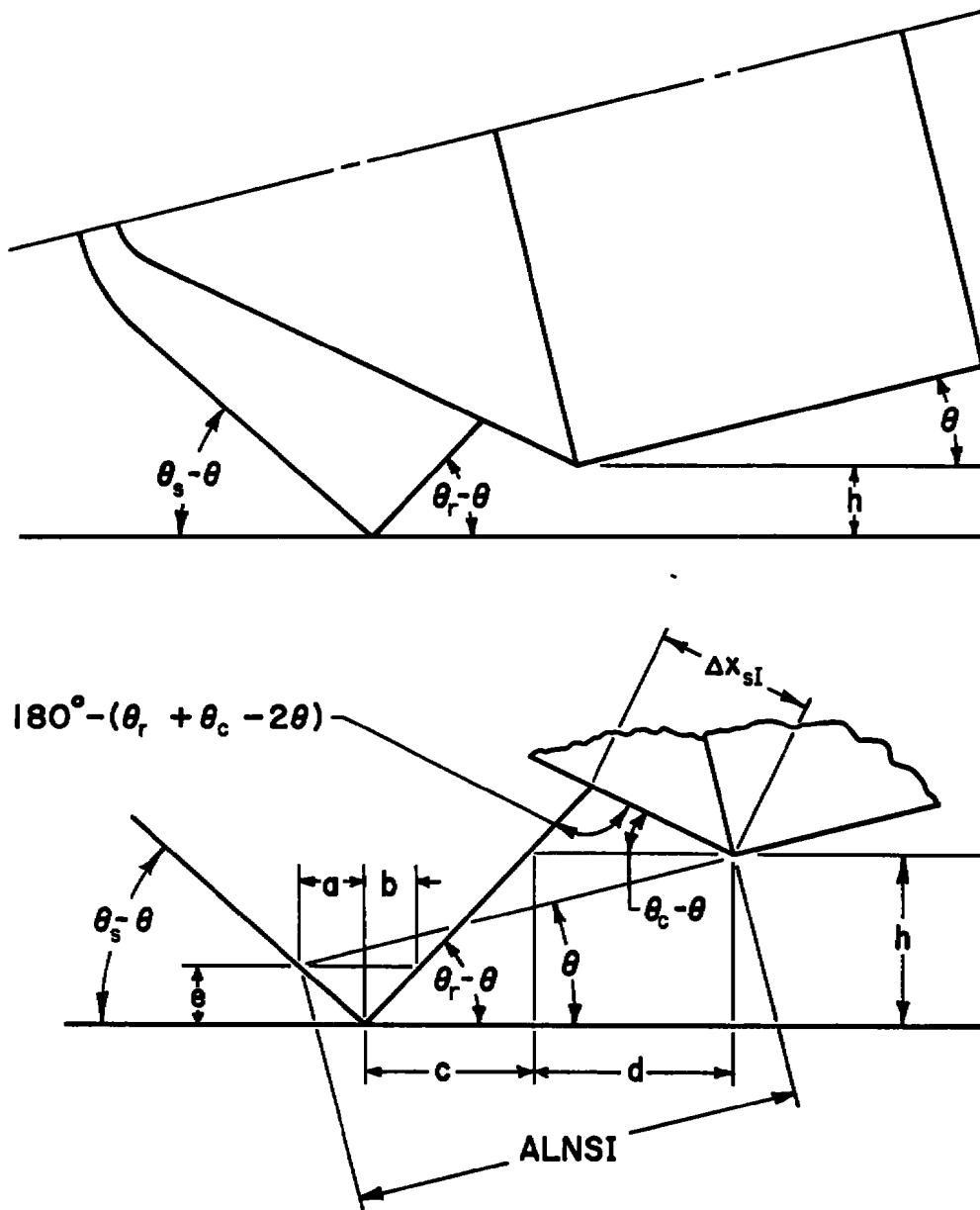
Figure 13. Sketch Showing Definition of Shock Interaction Distance Δx_{SI} when Projectile is Rotated through an Angle θ.

4.2.1 Laminar Couette Flow Model $(Re_h < 10^3)$

For determining the viscous shear forces and ablation rate, a local two-dimensional solution to Equations (13) and (16) is used. Based on a thorough study of gas bearing literature, we concluded in Section 3.5 that the pressure in the interface could be expected to remain reasonably constant at the entrance value over the entire length of the interface. Some pressure variation can, of course, be expected if the surface of the interface is not parallel to the rail surface and if the rate of mass addition to the interface flow due to ablation reaches of the same order as the flow of air pumped into the interface due to motion of the projectile. Both of these effects are included in determining the normal forces on the projectile. The effect of variation of the gap height along the interface is taken into account in determining the viscous shear, but not to determine the ablation rate.

The skin friction coefficient for laminar Couette flow, c_f, based upon the assumption that there is roughly equal heat transfer to the rail and to the projectile is given by;[23]

$$c_f = 2(1 + 0.0233 \, M_\infty^2)/Re_h , \qquad (43)$$

and the heat transfer rate, $\dot{q}_w$, is given by;

$$\dot{q}_w = 0.25 \, c_f \rho_\infty \, U_\infty^3 , \qquad (44)$$

where c_f is determined from Equation (43) using the average gap height. The net tangential force due to the interface is given by;

$$f_{tan} = W_{r,B} \, \tau_w , \qquad (45)$$

where;

$$\tau_w = 1/2 \, \rho_\infty U_\infty^2 c_f , \qquad (46)$$

67

if the projectile surface is parallel to the rail. If the pro-
jectile surface is not parallel to the rail, then the tangential
force is determined by integrating Equation (42) over the
length of the interface in order to obtain an average value of
c_f which is then substituted into Equation (46), in order to
determine f_{tan}.

The normal force due to pressure is taken to be the value
of the pressure multiplied by the area given by $W_r B$ plus an
additional force due to pressure buildup caused by ablation and a
contribution due to gas bearing effects if the surfaces are not
parallel. The additional pressure due to ablation is determined
by applying the simple model developed in Reference 1 for the
case of strong ablation. In Reference 1, the average pressure in
the interface due to ablation is determined by comparing the mass
flow at the exit of the interface to the mass ablation rate. It
was assumed in Reference 1 that the pressure would buildup in the
interface such that the density of the ablated gas vapor would
become large enough to allow the full ablation mass flow to pass
through the exit area of the interface. This is a grossly
simplified model, but was considered to be adequate for the pre-
sent purpose. The model of Reference 1 was implemented in the
program by fitting a curve to Figure 3 of Reference 1 to
describe a non-dimensional mass loss quantity ϕ, as a function
of projectile velocity. ϕ depends upon the thermal conductivity
and viscosity of the ablated vapor, the ablation temperature of
the projectile material as well as the projectile velocity. The
pressure in the interface due to ablation P_{abl} was then deter-
mined from Equation 11 of Reference 1;

$$P_{abl} = \frac{\dot{m}_a \, R_a \, T_v}{\phi \, U_\infty \, W_r \, h} \, , \qquad (47)$$

where R_a is the gas constant of the ablated vapor. The gas dyna-
mic properties for the ablated vapor were taken as those given in
Reference 1 for polycarbonate plastic.

The increase in pressure due to non-parallel interface
surfaces is taken into account in the following fashion. First,

the bearing number is calculated for an interface. The bearing number, Λ, is defined as;

$$\Lambda = \frac{6 \, \mu_\infty U_\infty B}{h_m^{\,2} P_4} \, ,$$ (48)

where h_m is the minimum gap height in the interface. The bearing number is an important dimensionless quantity which arises in the hydrodynamic theory of lubrication. The following observation has been made from an analysis of computer solutions to the compressible flow version of the Reynolds Lubrication Equation presented in Reference 8. For a wide variety of bearing shapes the non-dimensional bearing load, defined as;

$$W' = \frac{W}{A_\ell P_4} \, ,$$ (49)

can be expressed as;

$$W' = 0.006 \times \Lambda \quad (\Lambda \le 100) \, ,$$

or;

$$W' = 0.6 \quad (\Lambda > 100) \, ,$$

where W is the normal load on the bearing and W' is the average pressure which exists over the bearing surface, over and above the pressure at the inlet to the bearing. Thus, the additional normal force, f_{lube}, due to the gas bearing effect caused by non-parallel interface surfaces can be expressed as;

$$f_{lube} = W' A_\ell P_4 \, ,$$ (50)

The area referred to in Equation (50) as A_ℓ represents the area over which significant lubrication effects can be expected. The procedure used in the subroutine INTER to evaluate this area is to first consider the location on the projectile where the minimum gap height exists. If the minimum gap height exists

69

at the rear of the model, the entire interface area (W_rB) is used
to define A_ℓ. The center of pressure through which the lubrica-
tion normal force acts in this case is taken to be at a distance
of 0.7B from the front of the interface.[8] If the minimum gap
height is found to be at the front of the interface, then the
area A_ℓ is defined as W_r^2. For this situation, the front part
of the gas bearing surface is considered to be the entrance region
of the interface, i.e., the bearing can be described as a tapered-
flat slider bearing where the taper angle is equal to the half-
angle of the cone. The center of pressure is taken to be at the
shoulder of the cone cylinder.

4.2.2   Turbulent Couette Flow Model ($10^3 < Re_h < 10^5$)

In this model fully merged turbulent boundary layers
are presumed to exist at the entrance region upstream of the
interface region. The Reynolds number Re_h is sufficiently large
to prevent relaminarization in the interface itself and the tur-
bulent Couette flow model of Korkegi and Briggs[10] is used. The
model presented in Reference 10 is developed for the case of equal
heat transfer rates to the rail and to the projectile. In
Reference 11, Korkegi and Briggs developed a more general model
for non-equal heat transfer rates, but the effect of the non-
equal heat transfer rates does not significantly affect the skin
friction (see Figure 6 of Reference 11). In addition, a con-
siderable savings in computational time is realized by using the
formulation of skin friction for equal heat transfer rates. The
equation developed in Reference 10 for skin friction is given by;

$$\left[1 + \frac{\beta^2}{0.16} \frac{C_f}{2}\right] 8.8 \left(\frac{C_f}{2}\right)^{1/2} Re_h = 2 \left[1 + \frac{\beta^2}{4}\right]^{1/2} \times$$

$$\exp\left[\frac{0.4}{\beta} \left(\frac{2}{C_f}\right)^{1/2} \tan^{-1} \frac{\beta}{2}\right] - 2 + \frac{\beta^2}{0.4} \left(\frac{C_f}{2}\right)^{1/2} , \qquad (51)$$

where;

$$\beta^2 = 0.2 \, M_\infty^2 \quad .$$

Equation (51) is shown as a function of Mach number for various values of Re_h in Figure 14. The actual evaluation of Equation (51) in the computer program is carried out in subroutine TURBCE.

The average pressure over the interface will be a weak function of Re_h due to the fact that the mean velocity distribution is a fully developed turbulent Couette flow is such that, near the center of the interface, the derivative of the mean velocity profile with respect to z is zero. Thus, the central part of the flow will be influenced by the circumferential pressure gradient and some pressure relief can be expected. In subroutine INTER, the average pressure is taken to be;

$$\bar{P} = P_3 - (P_3 - P_2) \ [\log(Re_h) \ -3]/2 \tag{52}$$

The center of pressure of this average pressure is presumed to act at a distance of 0.4B from the front of the interface reflecting the fact that the pressure distribution is such that a higher pressure will exist over the front portion of the interface than over the rear portion. The heat transfer rate is determined by substituting C_f from Equation (51) into Equation (44).

4.2.3 Turbulent Boundary Layer Model $(Re_h > 10^5)$

The basic assumption underlying models for turbulent boundary layers is that significant circumferential pressure relief will occur due to the presence of an inviscid core region over the initial portion of the interface zone and that the amount of pressure relief will increase as Re_h becomes greater than 10^5. The criterion of using $Re_h = 10^5$ as the Reynolds number at which this pressure relief will become significant has not been rigorously established, but rather represents our judgement made on the basis of interface pressure distributions obtained by Korkegi and Briggs for hypersonic slipper bearings

71
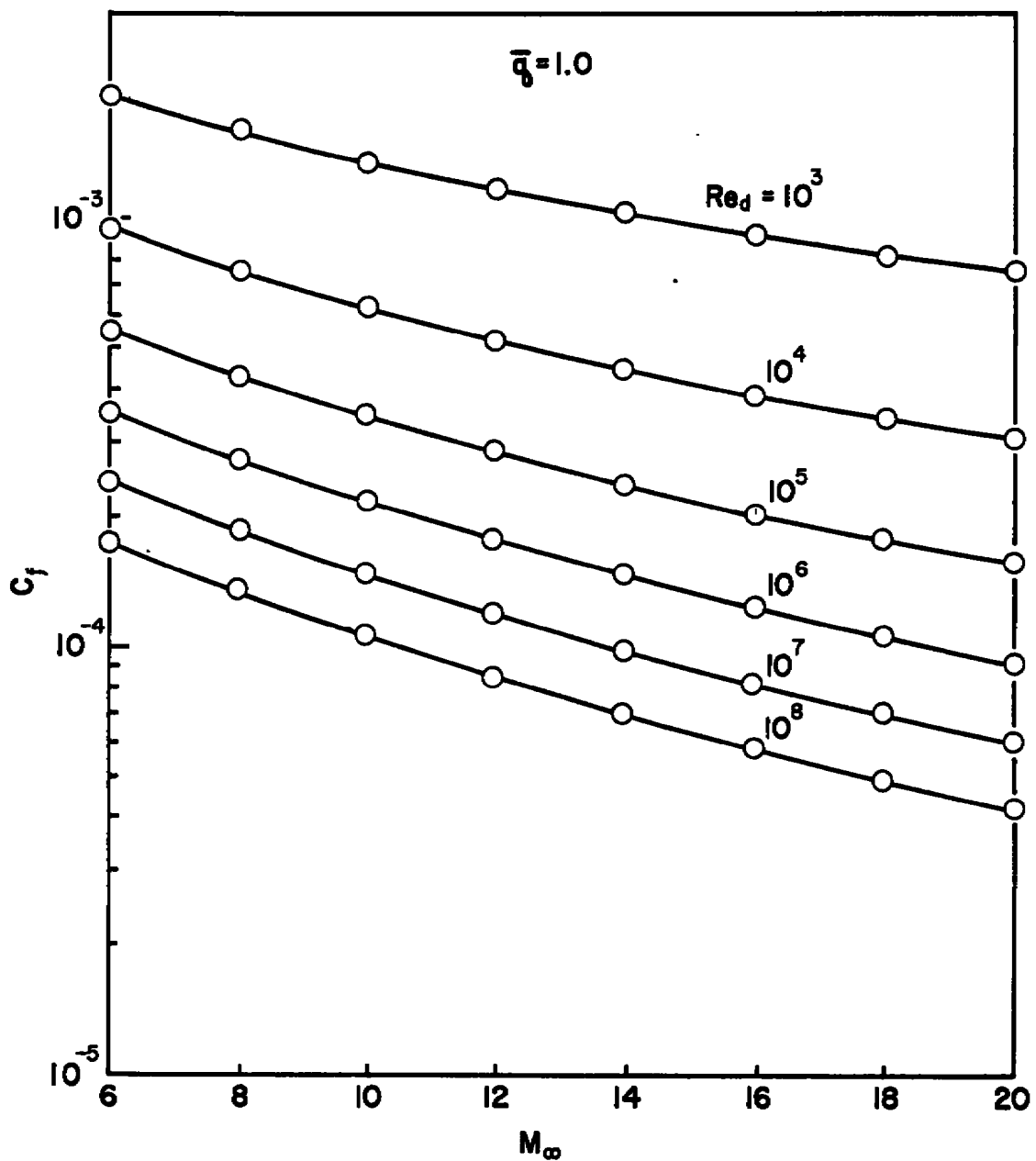
Figure 14. Skin Friction Coefficient Versus Mach Number for
Turbulent Couette Flow for Equal Heat Transfer
Rates at Rail and Projectile Surfaces.

72

tempered with the fact that pressure relief will occur more
rapidly in the rail/projectile problem than in the hypersonic
slipper problem.

The skin friction for the turbulent boundary layer is
determined from the Karman-Schoenher implicit formulation[9]
given by:

$$0.242 = \overline{C}_f \log (Re_x \ \overline{C}_f) \ , \tag{53}$$

where $\overline{C}_f$ is the average skin friction coefficient and the
Reynolds number is based on conditions evaluated at the pressure
existing at the sides of the interface and at a reference temper-
ature corresponding to the Sommer and Short reference enthalpy
defined by H^*/H_e given by:

$$\frac{H^*}{H_e} = 0.36 + 0.45 \frac{H_w}{H_e} + 0.19 \frac{H_{aw}}{H_e} \ . \tag{54}$$

A blowing correction factor B_c is applied to the skin friction
$\overline{C}_f$. This blowing factor is given by;[14]

$$B_c = \frac{1}{1 + 0.27 \ (H_{aw}-H_w)/L} \ , \tag{55}$$

$\overline{C}_f$ is computed in subroutine TURBFP. The tangential force is
then determined from the following equation;

$$f_{tan} = 1/2 \ \rho_e \ U_e^2 \ \overline{C}_f \ W_r \ \ell_a \ B_c \ , \tag{56}$$

and heat transfer rate is determined from;

$$q_w = \rho_e \ U_e \ \frac{\overline{C}_f}{2} \ (H_{aw}-H_w) \ W_r \ \ell_a \ B_c \ . \tag{57}$$

The average pressure is given by;

$$\overline{P} = P_2 - (P_2-P_5) \ [\log(Re_h) - 5]/5 \ . \tag{58}$$

The center of pressure is assumed to act at the midpoint of the afterbody. This completes the discussion of the present version of subroutine INTER. It should be mentioned that a simplified interface model, discussed next, was developed early in the present effort in order to check out the Projectile Dynamics Computer Program.

4.2.4   Simplified Interface Subroutine

A simple model which estimated at least the order of magnitude of the forces and moments on the projectile due to the interface was developed at the beginning of the program. From Equations (43) and (46) it is observed that for high projectile Mach numbers and small gap heights, the shear stress can be approximated by;

$$\tau_w = \frac{c \ U_\infty^3}{h} \ , \tag{59}$$

where c is a constant of proportionality. For small inclinations of the projectile relative to the rail, the pressure due to gas bearing effects and lubrication effects is inversely proportional to the square of the gap height, i.e.;

$$P = e/h^2 \ , \tag{60}$$

where e is another constant of proportionality. These two equations were used to construct a simple interface model. The details of this model are presented in Appendix A. This model has some potential usefullness insofar as it is very easy to use requiring only that the two constants c and e be specified.

This model could conceivably be used to represent the forces required to stabilize an unstable model since no actual physical collision with the rail can occur because of the $1/h^2$ behavior of the pressure. Thus, the maximum normal force required to prevent physical contact between the projectile and the rail can be estimated with the simple model.

4.3 INFLUENCE OF GAP HEIGHT AND MODEL ROTATION ON SHOCK INTERACTION LENGTH AND PRESSURE

The shock interaction length Δx_{SI} is obtained by noting the following geometric relations which apply to Figure 13.

$$e = h - ALNSI \sin \theta \tag{61}$$

$$a = e/\tan (\theta_s - \theta) \tag{62}$$

$$c = h/\tan (\theta_r - \theta) \tag{63}$$

$$d = ALNSI \cos \theta - a - c \tag{64}$$

Then the application of the law of sines to the triangle defined by the angles $\theta_c - \theta$, $\theta_r - \theta$, and $180° - (\theta_r + \theta_c - 2\theta)$ with two of the sides being d and Δx_{SI}, yields;

$$\Delta x_{SI} = d \; \frac{\sin (\theta_r - \theta)}{\sin (\theta_r + \theta_c - 2\theta)} \; . \tag{65}$$

Note that this result is based on the assumption that the bow shock rotates with the projectile.

The length ALNSI is either computed or read in as input data (see Appendix B).

The pressures at states 2, 3, or 4 in Figure 13 depend on θ. As can be seen from Figure 13, if the nose tip rotates toward the bottom rail, the lower conical surface of the projectile is inclined at a smaller angle, $(\theta_c - \theta)$, to the oncoming flow and the strength of the lower portion of the bow shock will be less than the shock strength when $\theta = 0$. Correspondingly, the upper conical surface will be inclined at angle $(\theta_c + \theta)$ to the oncoming flow and the strength of the upper portion of the bow shock will be greater than the $\theta = 0$ value.

For small turning angles, θ, the pressure change can be expressed as;

$$\Delta P = \frac{\rho U^2}{\sqrt{M^2 - 1}} \; (\pm \theta) \; , \tag{66}$$

where the plus sign is used when the flow is compressed. Using this result the pressure at state 2 with the projectile rotated can be approximated in terms of the pressure at state 2 when $\theta = 0$ in the following manner;

$$P_{2(\theta \neq 0)} = P_{2(\theta=0)} + \frac{\rho_2 U_2{}^2}{\sqrt{M_2{}^2 - 1}} (\pm\theta) , \qquad (67)$$

where the plus sign is used if the surface becomes more steeply inclined to the oncoming flow through projectile rotation and the negative sign is used if the surface becomes less steeply inclined. Similar reasoning leads to the following expressions for the pressures at states 3 and 4;

$$P_{3(\theta \neq 0)} = P_{2(\theta \neq 0)} \times \left(\frac{P_3}{P_2}\right)_{\theta=0} + \frac{\rho_3 U_3{}^2}{\sqrt{M_3{}^2 - 1}} (\pm\theta) , \qquad (68)$$

$$P_{4(\theta \neq 0)} = P_{3(\theta \neq 0)} \times \left(\frac{P_4}{P_3}\right)_{\theta=0} + \frac{\rho_4 U_4{}^2}{\sqrt{M_4{}^2 - 1}} (\pm 2\theta) . \qquad (69)$$

SECTION V

COMPUTER ANALYSIS OF PROJECTILE DYNAMICS

The interface models described in Section IV account
for the effects of the longitudinal motion of the projectile.
The projectile can also translate perpendicular to its axis
and can rotate about axes normal to its principal longitudinal
axis (pitch and yaw). These transverse motions have a direct
effect on the interface regions and therefore contribute to the
dynamic behavior of the interfaces with the rails. A computer
program describing projectile dynamics was developed to under-
stand these effects which includes descriptions of longitudinal,
translational, and rotational dynamics of the projectile. The
interface behavior is treated as coupling between projectile dy-
namics and interface behavior.

This model of projectile dynamics thus provides a complete
description of the operation of a guide-rail system with hyper-
velocity projectiles. All known components of the drag induced
on the projectile are computed as are the wear and wear rates
generated on the cylindrical surface of the projectile by inter-
action with the guide-rails. Finally, the model predicts the
stability of the projectile in flight along the rails and establishes
whether or not the projectile contacts the rails in flight. The
remainder of this section describes the computational architecture
of the projectile dynamics program and presents results from a
limited initial comparison between computed results and experi-
mental measurements from operation of the Tracks K and G at AEDC.
Some results from a scaling study are presented at the end of
this section.

5.1 OVERVIEW OF PROJECTILE DYNAMICS PROGRAM

A generalized flow chart of the projectile dynamics program is presented in Figure 15. Operation of the program is initiated by inputting the following parameters to an initialization subroutine: dimensions of the rail system and projectile; material characteristics of the projectile; atmospheric conditions in the ballistic range; aerodynamic coefficients of the projectile; irregularities of the rail system; initial position, orientation, and velocity of the projectile; and the variety of commands used to select various computational options within the remainder of the program structure. The initialization subroutine then calculates a variety of parameters used for subsequent computations such as initial gap height between the projectile and each of the rails, and initial orientation of the model and its velocity vector with respect to the upstream end of the rail system.

The main section of the program is an executive routine which coordinates the operation of an array of subroutines that accomplish the actual computations. Aerodynamics subroutines (called "DRAG" and "DRAGCO") are available which translate the aerodynamic coefficients of the projectile together with the model velocity and range atmospheric parameters into aerodynamic forces and moments applied to the model. Provisions are available within subroutine DRAGCO to treat aerodynamic coefficients as functions of Mach number and other independent variables. The aerodynamic subroutine DRAGCO also accounts specifically for shock interference effects due to the presence of the rail system. These routines are described generally in Section IV and specifically in Appendix B.

The projectile dynamics computer program has available two separate subroutines for analyzing the interface regions between the model and the guide-rails. Both are called "INTER" and are described generally in Section IV and are specified in Appendix B. The first is an extremely simplified model containing virtually no physics that was constructed to provide credible output data from the interface regions with minimal
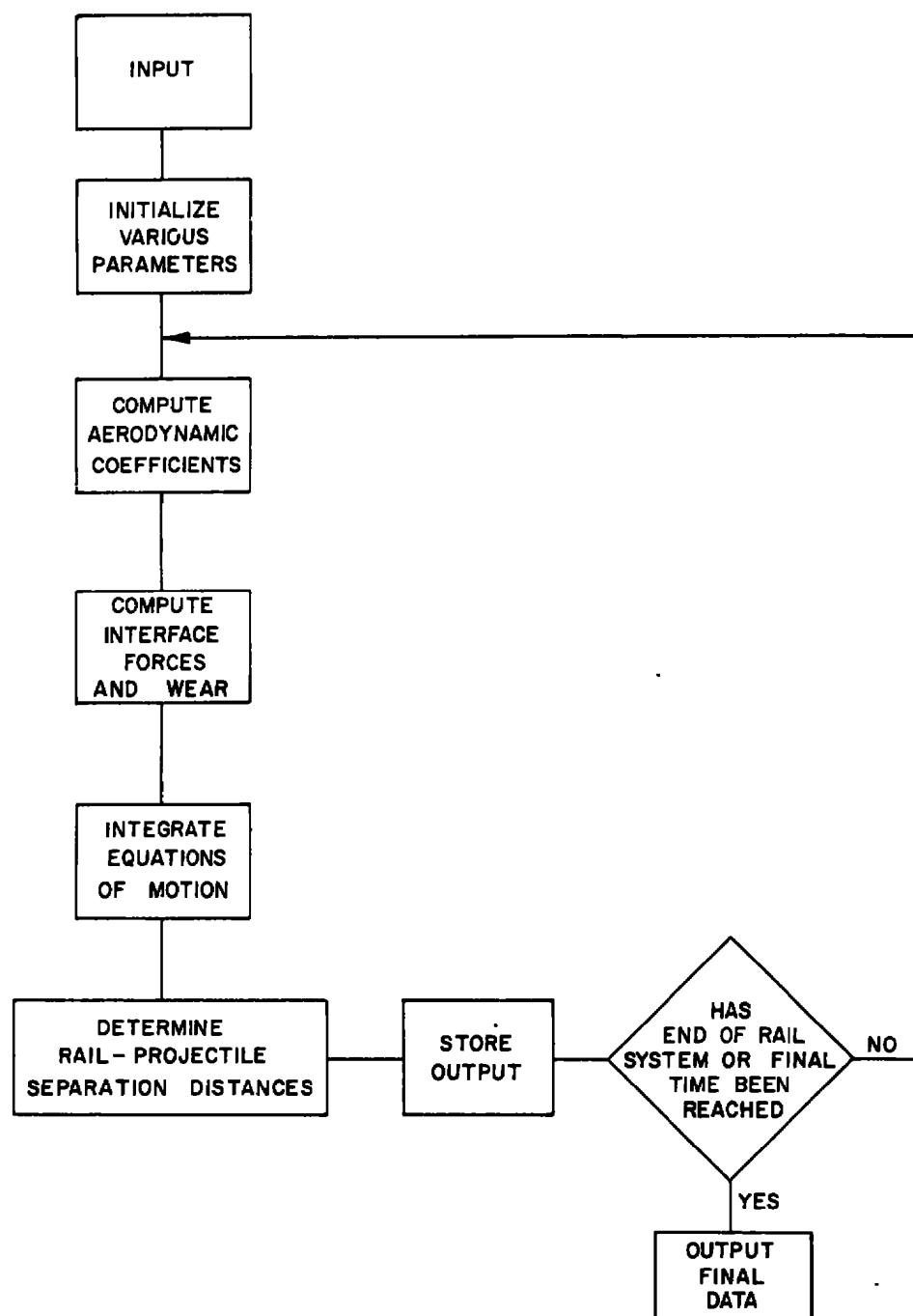
Figure 15.   Overview of Dynamic Rail/Projectile Modeling Program.

computational effort. This subroutine was used during develop-
ment of the remainder of the overall computer program and is still
useful for debugging tasks. The second interface subroutine
contains all of the physics of the projectile rail/interface
region that the authors currently understand, and is the model
that should be used for making actual predictions of rail/projectile
performance. The complete interface subroutine computes all
known forces arising within the interface region between the
projectile and the rails and also computes wear of the projectile.

The subroutine that employs rigid body equations of motion
to describe the position, velocity, orientation, and the pitch
rate of the model at any instant after the model has engaged
the rail system is called "RK" in the main computer program.
This subroutine accepts inputs from the other subroutines
describing forces and torques applied to the projectile and
outputs to appropriate subroutines projectile positional in-
formation required for their operation. Subroutine RK is des-
cribed in a subsequent paragraph of this section and is specified
in detail in Appendix B.

The rail system subroutines called "ORIENT" and "CONFIG"
contain equations of the rail surfaces relative to an earth-
fixed coordinate system. These routines are described in Appen-
dix B. CONFIG describes irregularities of the rail system,
such as steps, bends, convergences/divergences, etc. The in-
stantaneous separation distances between the model and each of
the rails are computed in ORIENT based on: the position of the
rails as defined by subroutine CONFIG; the position of the pro-
jectile as defined by the equations-of-motion subroutine; and
the amount of wear the projectile has experienced as defined by
the interface subroutine. The projectile position, orientation,
and wear are all outputted at time or space intervals specified
as input. Computation cycles of the main computer routine are
repeated until the projectile either reaches the end of the rail
system or exceeds a predefined performance envelope which leads
to the premature termination of its flight.

5.2   EQUATIONS OF MOTION SUBROUTINE

The three-dimensional equations of motion of the projectile are;

$$M_p \ddot{x} = - D_A \cos \gamma - D_I \cos \theta + L_A \sin \gamma + L_I \sin \theta, \qquad (70)$$

$$M_p \ddot{z} = - M_p g - D_A \sin \gamma - D_I \sin \theta + L_A \cos \gamma + L_I \cos \theta, \qquad (71)$$

$$I_y \ddot{\theta} = T_A + T_I, \qquad (72)$$

The x-z coordinate system is an earth-fixed system with the x-axis perpendicular to the earth's gravitational vector at the front end of the rail system. The z-axis is parallel to the gravitational vector and is positive upward. Figure 16 illustrates the directions of the forces acting on the projectile. The aerodynamic drag is in the opposite direction to the velocity
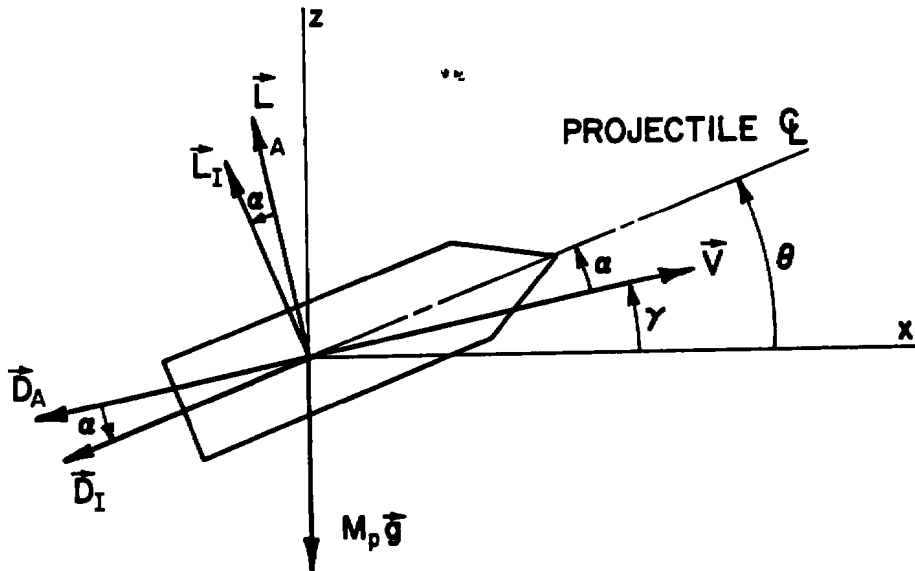
Figure 16. Forces Acting on the Projectile.

vector and the aerodynamic lift is perpendicular to the velocity
vector. The frictional force arising from the projectile-rail
interfaces is parallel to the projectile body and the lift
arising from the interfaces is perpendicular to the projectile
body. The angle γ is defined as;

$$\gamma = \tan^{-1} \frac{\dot{z}}{\dot{x}} . \tag{73}$$

The magnitudes of the aerodynamic forces and torque
acting on the projectile are given by;

$$D_A = 1/2 \, \rho \, SV^2 \, C_D, \tag{74}$$

$$L_A = 1/2 \, \rho \, SV^2 \, C_L, \tag{75}$$

$$T_A = 1/2 \, \rho \, S\bar{c}V^2 \, C_m. \tag{76}$$

The magnitude of the velocity vector is given by the equation;

$$V = (\dot{x}^2 + \dot{z}^2)^{1/2} . \tag{77}$$

The aerodynamic coefficients are given by the equations;

$$C_D = C_{D_0} + C_{D_\alpha}\alpha + C_{D_{SI}}, \tag{78}$$

$$C_L = C_{L_0} + C_{L_\alpha}\alpha + \frac{\bar{c}q}{2V}C_{L_q} + \frac{\bar{c}\dot{\alpha}}{2V}C_{L_{\dot{\alpha}}} + C_{L_{SI}}, \tag{79}$$

$$C_m = C_{m_0} + C_{m_\alpha}\alpha + \frac{\bar{c}q}{2V}C_{m_q} + \frac{\bar{c}\dot{\alpha}}{2V}C_{m_{\dot{\alpha}}} + C_{m_{SI}}. \tag{80}$$

The angle of attack and its time derivative are given by;

$$\alpha = \theta - \gamma, \tag{81}$$

and;

$$\dot{\alpha} = q + g/V \cos \gamma - \rho VSC_L/(2M_p). \qquad (82)$$

The above equations define the motion of the projectile. The values of the various coefficients in the equations for C_D, C_L, and C_m are computed in subroutine DRAG. The values for D_I, L_I, and T_I are computed in subroutine INTER. The forces and moments in the x,z, and θ directions are computed in subroutine F from information determined by subroutines DRAG and INTER. The equations of motion are integrated with a fourth-order Runge-Kutta scheme in subroutine RK.

5.3   ELASTIC DEFORMATION SUBROUTINE

As was mentioned in Section 3.6, only rigid body behavior of the projectile was initially considered. This approach was found to be inadequate when the rigid body computer model was used to simulate Track K experiments. It was found that the slightest perturbation to the projectile would always result in the model colliding with a rail. The pressures developed in the interface due to gas bearing and ablation effects were too small to keep the projectile cylindrical surface from contacting the rail. In order to estimate the forces and pressures required to prevent projectile/rail contact a linear elastic analysis of projectile deformation was conducted. This analysis showed that the forces required to deform the projectile and prevent contact were very large. If this force arises from gas bearing effects, the interfacial pressures necessary to account for such high forces imply very small gap heights and correspondingly small Reynolds numbers. The gap heights required are of the order of the surface asperities. When the importance of elastic deformation was realized, an elastic collision subroutine, ELASTC , was added to the program. This subroutine is based on a simple linear elastic relation of the form;

$$P_{e\ell} = k_e \, \delta_{e\ell} \, , \tag{83}$$

where $P_{e\ell}$ is the local force per unit area due to a local elastic deformation $\delta_{e\ell}$, and k_e is an elastic coefficient. Subroutine ELASTC is called whenever subroutine ORIENT produces a negative separation distance between the projectile and a rail, based upon a rigid body calculation. A linear relation between deformation required to reduce the negative separation distance to zero and distance along the projectile surface in the x-direction is presumed. The normal force required to deform the projectile surface so that the projectile surface does not pass outside the boundary of the rail is then determined by integrating Equation (83) over the region where negative separation distances would occur if the projectile were perfectly rigid. The equations for determining the normal forces and moments due to elastic collisions are developed in Appendix C.

Whenever a collision occurs with a rail, an additional mechanism for heat transfer exists due to the sliding friction. The sliding friction force, F_{sf}, is given by;

$$F_{sf} = \bar{\mu} \, F_n \, , \tag{84}$$

where F_n is the total normal force due to elastic deformation. The energy dissipation rate due to the sliding friction is given by;

$$\dot{Q}_{sf} = F_{sf} U_\infty \tag{85}$$

which is taken to be the rate of energy transfer to the projectile surface. The ablation rate due to sliding friction is then;

$$\dot{m}_{sf} = \bar{\mu} \, F_n \, U_\infty / L. \tag{86}$$

5.4   METHOD USED TO CALCULATE WEAR ON A PROJECTILE

Mass is removed from the projectile through two
mechanisms, ablation due to aerodynamic friction and ablation
due to sliding friction. Neither of these two mechanisms lead
to a uniform surface recession rate over the contact area be-
tween a rail and the projectile. A simplified method was used
to approximate the change in shape of the wear surfaces of the
projectile. The top and bottom wear surfaces of the pro-
jectile are each approximated by two straight line segments as
shown in Figure 17. These straight line segments are defined
by tracking the surface recession at three points on each of
the top and bottom wear segments: the front; the midpoint; and
the rear of the cylindrical portion of the projectile. The wear
surface at the side rail contact with the projectile is approxi-
mated by a single straight line segment defined by tracking
the surface recession at the front and rear of the cylindrical
portion of the projectile. The two side rail contact surfaces on

DASHED LINES REPRESENT
ORIGINAL SHAPE OF PROJECTILE
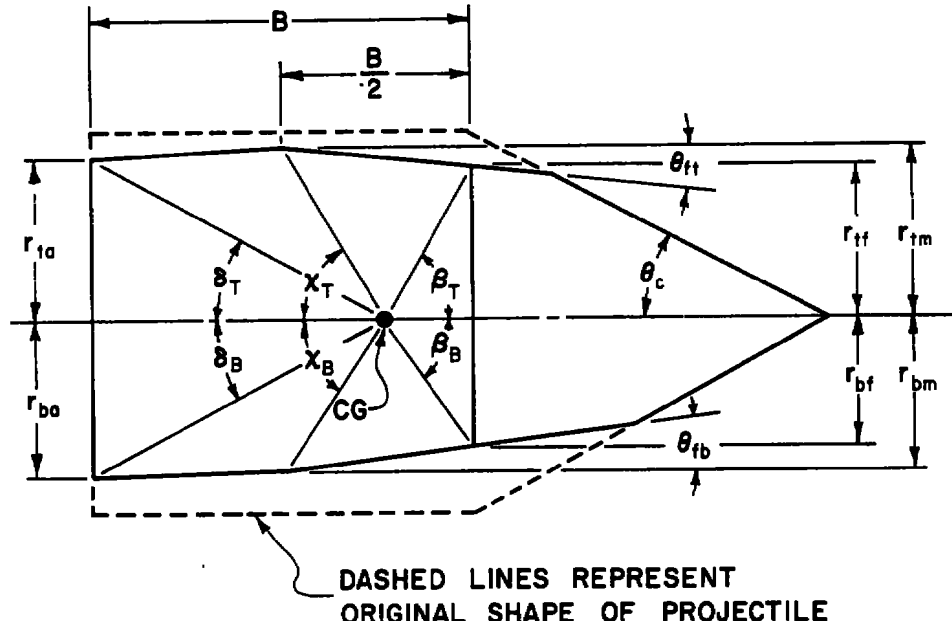
Figure 17.   Sketch Showing How the Instantaneous Shape of the
Projectile is Defined to Account for Wear.

the projectile are assumed to wear at the same rate whereas the
top and bottom wear surfaces will not, in general, wear symmetrically.
Thus, the surface recession rate is computed at eight different
points on the projectile.

Note in Figure 17 that the front segments of the top and
bottom wear surfaces extend onto the conical forebody. Track
G experience with shots at high projectile velocities (5000 m/s
and higher) at range pressures of 0.5 atm or greater showed large
amounts of wear. When attempts were made to simulate these
shots with an early version of the computer program which did
not consider the extension of the wear surface onto the conical
forebody, the predicted projectile wear was so high that the
projectile could have tumbled down the range. The increase in
the length of the wear surface as the shoulder of the cylindrical
portion of projectile wears is called "increase in wheelbase due
to projectile wear." In Figure 18 this increase in wheelbase
due to wear is denoted by ΔB. The radial location of the front
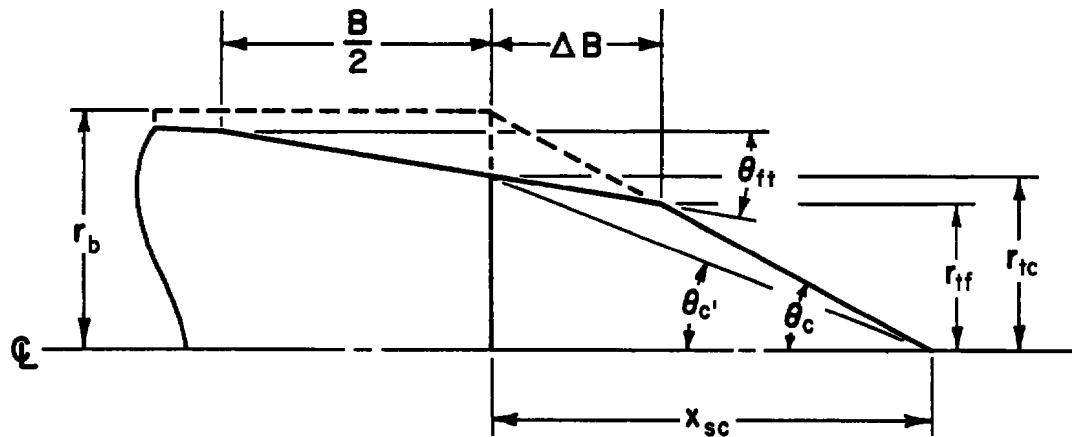
Figure 18. Sketch Showing Increase in Wheelbase Due to Wear, ΔB.

edge of this extended wear surface on the top of the projectile is denoted by r_{tf} in Figure 18. The axial position of r_{tf} and its counterpart on the bottom wear surface, r_{bf} are continuously tracked in the computer program. In particular, this point is used as one of the four points on each of the top and bottom wear surfaces in subroutine ORIENT where the separation distance between the projectile and the rail is computed. Likewise the normal force due to contact with the rail is computed at this point of the separation distance at this point becomes negative. The increase in wheelbase due to wear serves to increase the moment arm of the elastic deformation normal force when contact with the rail occurs at the front of the projectile. Thus, the magnitude of the normal force and wear experienced by the projectile during such a collision with the rail is less than the normal force and wear computed when the increase in wheelbase due to wear is not included in the analysis.

5.5 ˙ COMPARISON OF COMPUTED RESULTS WITH LIMITED EXPERIMENTAL DATA

Limited data for evaluating the predicted results have become available recently as a result of both dynamic measurements made during range firings at Tracks K and G and observations of models recovered after negotiating the hypervelocity tracks.

5.5.1 Comparisons with Track K Results

Track K at AEDC was outfitted with a set of hypervelocity guide rails approximately 30 m long. This system became operational and produced significant amounts of experimental data during the time that the study described in this report was being conducted. Several firings of projectiles with 30° and 45° half-angle cone sections were carried out where good quality data was achieved. More recently, a 10° half-angle cone projectile was launched successfully in Track K. No wear of the cylindrical surfaces of launched models caused by interactions with the guide rails was observed experimentally in Track K.

This result is in agreement with our predictions that wear during 30 m of travel would be slight. Unfortunately, this verification shed relatively little light upon the question of the validity of our analysis.

An indirect, but potentially important evaluation was carried out involving the total drag experienced by hypervelocity projectiles moving along guide-rails. The Track K data indicate that total projectile drag was 30 percent to 50 percent greater than would have occurred had the projectiles been launched into an open range. The computer model described in this section is capable of predicting total drag forces on projectiles flying along hypervelocity guide rails, so a basis of comparison was possible. Shot No. 2968 at the AEDC Track K involved launching a 30° half-angle cone at a velocity just over 3.87 km/s. The remainder of the information known to the authors about Shot No. 2968 is presented in Table 4. The total drag coefficient as determined from velocity reduction data was C_D=0.788. This shot was used as the basis for a computational run of the Projectile Dynamics Program from which a total drag coefficient of 0.789 was computed. The close agreement between the measured and predicted value (just over 0.1 percent deviation) is almost certainly fortuitous, although the comparison gives good reason to hope that at least the aerodynamic phase of the program describes practical situations accurately.

Also shown in Table 4 are results from a single firing of a 10° half-angle cone at a velocity of 2.35 km/s. A total drag coefficient of 0.199 was measured, while the results of a computation using identical input parameters predict a drag coefficient of 0.170. This value for total drag was the result of allowing the reflected weak shock from the rail to re-reflect from the cone once. The predicted value for the total drag coefficient was 0.140 when the reflected shock from the rail was not allowed to re-reflect from the conical surface. When the rail reflected shock was presumed to be a strong oblique shock, a total drag coefficient of 0.633 was obtained computationally.

TABLE 4.   COMPARISON OF COMPUTED TOTAL DRAG COEFFICIENTS
WITH EXPERIMENTAL DATA FROM TRACK K AT AEDC.

30° CONE PROJECTILE

Shot No. 2968

Projectile Type	30° half-angle cone, Model No. 4927
Projectile Diameter Before Launch	1.617" (41.07 mm)
Projectile Diameter After Launch	1.600 to 1.604" (40.64 to 40.74 mm)
Projectile Weight Before Launch	121.61 g
Projectile Velocity	12,317 ft/s (3.755 km/sec)
Range Pressure	103.7 torr (1.36 x 10^4 pa)
Range Temperature	66°F (18.9°C)
Measured Total Drag Coefficient	0.788
Predicted Total Drag Coefficient	0.789

10° CONE PROJECTILE

Shot No. 3014

Projectile Type	10° half-angle cone
Projectile Bluntness Ratio	0.167
Projectile Diameter Before Launch	1.625" (nom) (41.3 mm)
Projectile Diameter After Launch	
Projectile Weight Before Launch	152.6 gm
Projectile Velocity	7700 ft/s (2.348 km/sec)
Range Pressure	711.8 torr (9.36 x 10^4 pa)
Range Temperature	70°F (nom) (21.1°C)
Measured Total Drag Coefficient	0.199 ± .003

Predicted Total Drag Coefficients:
- weak reflected shock reaches cone surface: 0.170
- weak reflected shock doesn't reach cone surface: 0.140
- strong reflected shock: 0.633

We feel that the later computational result is especially sig-
nificant since the large deviation from the measured total drag
coefficient demonstrates that shock waves reflected from the
rails by slender cone projectiles are not strong. The viscous
drag computationally predicted to arise from the rail interface
region for the 10° half-angle cone was only 0.6 percent of the
total drag, and therefore, does not figure to any significant
extent in the difference between predicted and measured results.

A second factor of considerable importance became obvious
during the computation of the 10° cone trajectories. The pro-
jectile is highly unstable aerodynamically and our analysis which
included deformation considerations indicates that the projectile
will contact the rails. Careful consideration of the predicted
results lead us to believe that this prediction is correct, and
therefore, that the projectile fired in Track K indeed did contact
the rails repeatedly during its passage along them. No unusual
gouging or wear were noted after the firing either on the recovered
projectile or the rails. These considerations lead us to believe
that our initial assumption that gouging always occurs when the
projectile touches the rails during passage is an oversimplification.
Clearly, more work is needed to establish a proper gouging criterion.
In summary, we have strong indications that projectiles can contact
rails without undue wear or gouging at least under some circum-
stances. Computed values of total drag coefficients correlate
well with measurements for flights of projectiles with 30° half-
angle cones. Deviations between predicted and measured total drag
coefficients are somewhat larger for projectiles with slender cone
forebodies. These deviations are probably caused by either under-
estimation of the conical area of the projectile affected by shock
waves reflected from the rails, or by drag increases caused by
projectile/rail contact. Finally, comparisons between computational
and experimental results for the 10° cone flights strongly indicate
that shock waves reflected from the rails are weak and indicate
somewhat less certainly that reflected shock waves from the rails
actually re-reflect from the conical surface.

5.5.2   Comparison to Track G Results

Track G projectiles have typically been composite structures. The cylindrical portion, including the primary wear surfaces, have been made from polycrabonate. An internal aluminum strut supports the nose tip and provides a conical surface to which a carbon-epoxy heat shield is bonded. Some projectiles have forebodies which are essentially hemisphere-cylinder-conical configurations while others have forebodies which are essentially blunted cones. Table 5 lists wear measurements and instantaneous angular rotation measured from flash radiographs or laser photographs at the last observation point where photographs were available. The half-angle of the conical portion of the forebody on all of the projectiles listed in Table 5 was 25 degrees.

TABLE 5.   WEAR AND ANGULAR ROTATION OBSERVATIONS FOR SELECTED
TRACK G SHOTS

Shot No.	Velocity (m/s)	Range Pressure (torr)	Max. Groove Depth* (mm)	Min. Groove Depth* (mm)	Angle of Rotation*** (degrees)	Type of Model
4836	2870	233	0.89	0.41	-1.5	Erosion
4882	4880	570	3.30	1.27	8	Transition
4885	4880	100	2.06	1.37	2.2	TCNT**
4886	4880	150	2.29	1.02	-----	Erosion
4880	4880	100	1.78	0.89	>1	Erosion
4884	4880	570	3.18	1.27	5	Transition

---

*Based on post-launch diameter of 62.5 mm (0.51 mm wear assumed in launcher).

**TCNT--transpiration cooled nose tip.

***Angle of rotation at last x-radiograph or laser photography station--
not necessarily the maximum angle of rotation of the projectile.

A number of computer simulation runs were made for a Track G projectile. The purpose of these runs was primarily to determine values of the sliding friction coefficient $\bar{\mu}$ and the heat of ablation L which would yield good correlations between computed and measured wear. $\bar{\mu}$ was varied over a range from 0.0001 to 0.02 and L was varied from 3.8×10^6 joules/kg to 6.4×10^6 joules/kg. Typical results of these computations are shown in Table 6. The value of the elastic coefficient $k_e = 2.6 \times 10^{11}$ N/m^3 ($\sim 0.78 \times 10^6$ lb$_f$/in^3) was obtained from Dr. J. Hicks of ARO/VKF. He used a finite element structural analysis technique to determine the stiffness of a typical Track G composite model. His analysis showed that the elastic coefficient for Track G models could be represented by;

$$k_e = \frac{2.05 \times 10^9}{W_r} \ (\text{N/m}^3), \qquad (87)$$

where W_r is the width of the contact surface (rail width in meters). The rail width of Track G rails is 8 mm (0.31 in.). The geometric parameters of the projectile used in the computer simulation runs were as follows: $\sigma = 25°$, $r_n/r_b = 0.3$, $d_p = 62.5$ mm (2.46 in.), B = 63.5 mm (2.50 in.). An initial gap height of 0.5 mm (0.020 in.) was used reflecting Track K and Track G experience where about 0.5 mm of wear was found to have occurred in the launcher. Based on the results shown in Table 6 it was concluded that $\bar{\mu} = 0.0075$ and $L = 4.2 \times 10^6$ joules/kg produced acceptable agreement between computed and measured wear for Track G projectiles.

An important conclusion that can be drawn from the results presented in Table 6 is that the maximum wear experienced by the projectile decreases as the wavelength of sinusoidal rails decreases, all other parameters being held constant. Note that the maximum wear for a wavelength of 24.4 m (80 ft) is nearly the same as for the corresponding straight rail case.

TABLE 6.   COMPUTED WEAR AND MAXIMUM ANGLE OF ROTATION FOR TRACK G MODEL FOR VARIOUS VALUES OF HEAT OF ABLATION AND COEFFICIENT OF SLIDING FRICTION. $k_e = 2.6 \times 10^{11}$ N/m^3

Velocity (m/s)	Range Pressure (torr)	L MJ/kg	$\bar{\mu}$	Max. Groove Depth (mm)	Min. Groove Depth (mm)	Max. Angle of Rotation (degrees)
			Straight Rails			
2870	233	4.2	0.0005	0.26	0.23	-1.3
4880	100	4.2	0.0005	0.48	0.43	2.0
4880	150	4.2	0.0005	0.90	0.58	2.5
4880	150	6.4	0.0005	0.58	0.45	-2.0
4880	570	4.2	0.0005	4.52	1.50	-6.6
4880	570	3.8	0.0005	5.00	1.61	-6.8
4880	760	4.2	0.0005	5.44	1.76	-6.8
Sinusoidal Rails, Wavelength = 6.1 m (20 ft), Amplitude = 0.19 mm (0.0075 in.)						
4880	570	4.2	0.0010	2.02	1.50	1.8
Sinusoidal Rails, Wavelength = 6.1 m (20 ft), Amplitude = 0.38 mm (0.015 in.)						
4880	150	4.2	0.0005	1.07	0.58	2.6
4880	150	4.2	0.0010	1.77	0.58	-5.8
4880	570	4.2	0.0005	1.95	1.50	3.9
4880	570	4.2	0.0010	2.39	1.50	-5.4
Sinusoidal Rails, Wavelength = 12.2 m (40 ft), Amplitude = 0.38 mm (0.015 in.)						
4880	570	4.2	0.0005	2.11	1.50	5.8
4880	570	4.2	0.00075	4.80	1.50	-6.7
4880	570	4.2	0.0010	6.34	1.52	-6.5
Sinusoidal Rails, Wavelength = 24.4 m (80 ft), Amplitude = 0.38 mm (0.015 in.)						
4880	570	4.2	0.0005	4.44	1.51	-6.6

5.6   RESULTS OF AN INITIAL SCALING STUDY

Much larger guide-rail systems than these installed in Tracks K and G are currently being contemplated at AEDC. A primary concern for estimating feasibility of such track facilities is to determine how projectile wear will scale with: projectile diameter and velocity; track length; rail width; and range pressure.

The projectile dynamics computer program has been used to conduct an initial scaling study to support such an investigation. Some results obtained during the course of this study are presented in this section.

The values of $\bar{\mu}$ and L used for the scaling study were those which lead to good agreement between computed and measured wear for Track G projectiles, namely $\bar{\mu}$ = 0.00075 and L = 4.2 x 10^6 J/kg. The value of k_e used in the scaling study was determined from Equation 87. The basic configuration of the model used for the scaling study was provided by AEDC staff and is shown in Figure 19. Nominal projectile diameters of 12.7 cm, 20.32 cm, and 30.48 cm (5, 8, and 12 inches respectively) were considered with cone half-angles of 8, 10,and 15 degrees. Dimensional and other properties of these projectiles are presented in Table 7. The initial gap height used for the scaling study was linearly scaled with projectile diameter from the Track G value of 0.5 mm. The initial lateral velocity of the projectile was fixed at 0.6 m/s (2 ft/sec).

Some typical wear histories for 12.7 cm diameter, 10° half-angle cone projectiles are shown in Figures 20, 21, and 22. In these figures, the maximum wear on each of the wear surfaces is given as a function of distance traveled by the projectile. DRTF represents the ·change in radius (wear) at the front of the top wear surface, DRBF represents the change in radius at the side front wear surface. No collisions occur at the side rails so that wear at the side surface is due solely to aerodynamic heating whereas wear at the top and bottom surfaces is due to
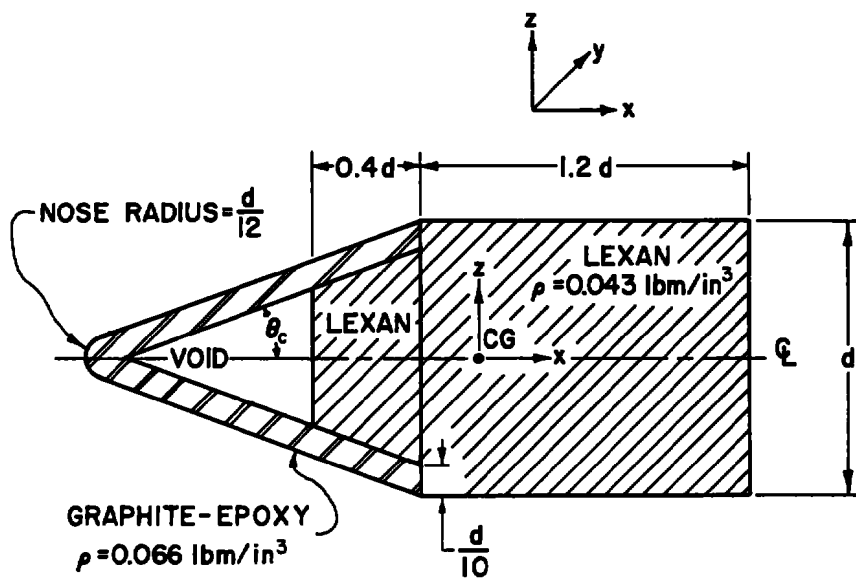
Figure 19. Configuration of Composite Projectile Used for Scaling Study.
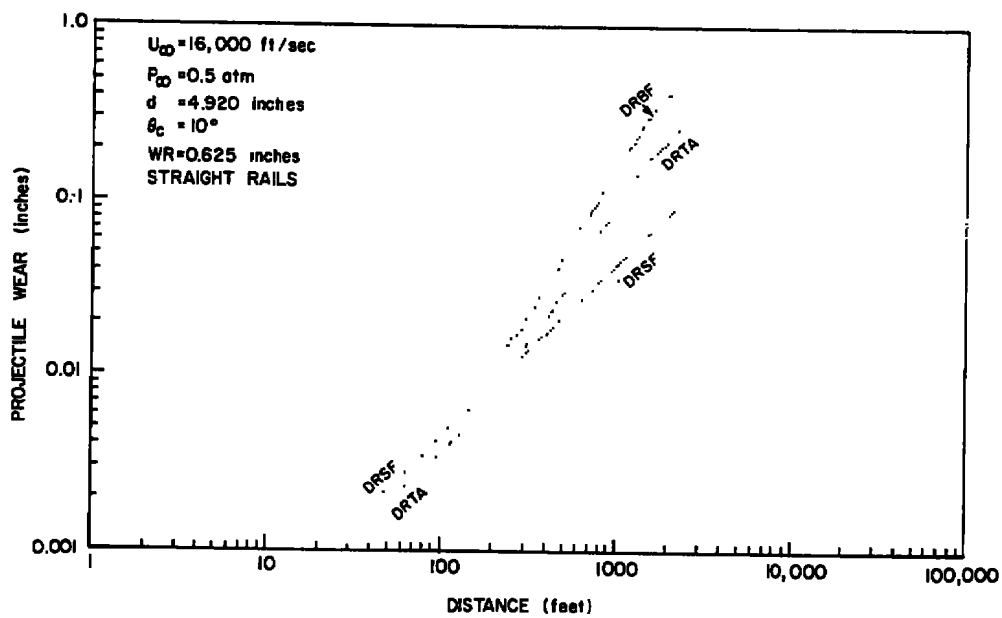

Figure 20. Wear History of a Nominal 13 cm (5 inch) Diameter Projectile. Straight Rails with Rail Width Linearly Scaled from Track G.
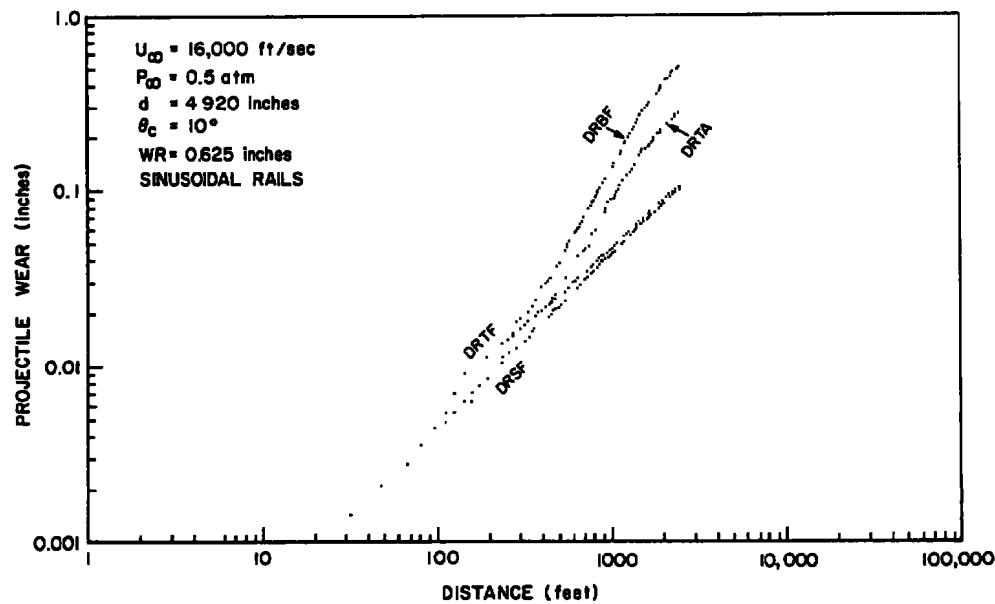
Figure 21. Wear History of a Nominal 13 cm (5 in.) Diameter Pro-
jectile--Sinusoidal Rails.
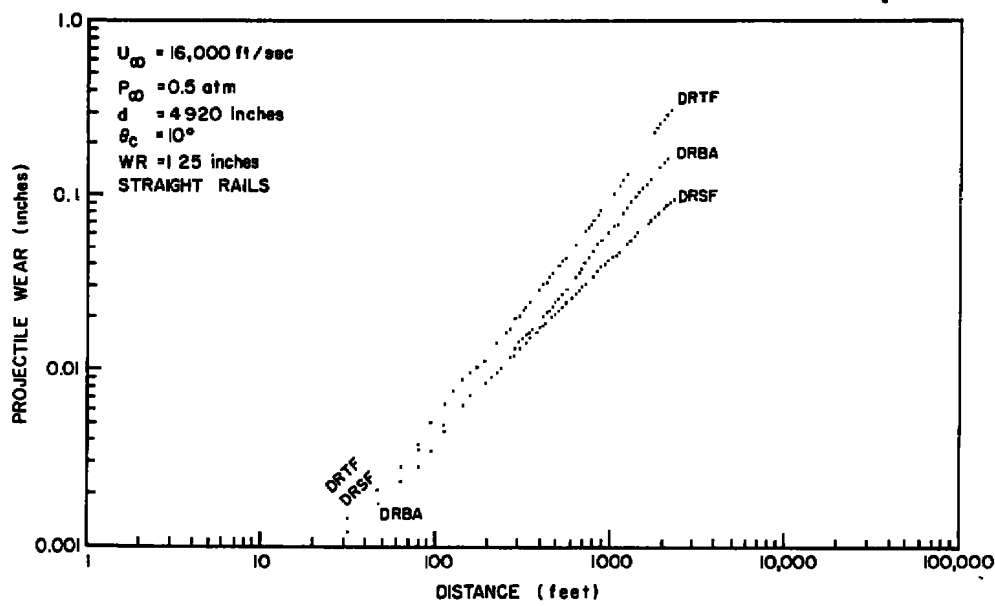
Figure 22. Wear History of a Nominal 13 cm (5 in.) Diameter Pro-
jectile. Straight Rails with Rails Twice as Wide as
Linearly Scaled G. Track.

TABLE 7. PROPERTIES OF PROJECTILES USED IN SCALING STUDY

Diameter (in)	Diameter (m)	Cone Half Angle (deg)	Mass (kg)	l_f^* (m)	l_a (m)	I_y (kg-m^2)
5.0	0.127	8	4.41	-0.0138	0.1662	0.0666
5.0	0.127	10	4.05	+0.0054	0.1470	0.0446
5.0	0.127	15	3.55	+0.0294	0.1230	0.0248
8.0	.203	8	18.06	-0.0222	0.2660	0.6983
8.0	.203	10	16.60	+0.0086	0.2352	0.4679
8.0	.203	15	14.56	+0.0471	0.1967	0.2598
12.0	.305	8	60.95	-0.0333	0.3990	5.301
12.0	.305	10	56.02	+0.0130	0.3528	3.553
12.0	.305	15	49.13	+0.0707	0.2951	1.973

*Negative l_f means center of gravity is located on forebody.

both sliding friction and aerodynamic heating. Figure 20 shows
that the projectile has nosed down and is sliding on the front
of the bottom wear surface after 61 m (200 ft) of travel and re-
mains in that position during the remainder of its travel. This
is a phenomenon which was observed in Track G projectiles at
range pressures between 0.75 and 1.0 bars. Figure 21 shows that
the influence of periodic rail unevenness is negligible when the
wavelength is 30.5 m (100 ft). This is consistent with the re-
sults given in Table 6 for a Track G projectile where it was ob-
served that the wear for a wavelength of 24.4 m (80 ft) was nearly
identical to that for a corresponding straight rail case. However,
smaller wavelengths can cause the wear to be more evenly distributed
between the top and bottom surfaces while at the same time re-
ducing the maximum wear experienced by the projectile as is evident
from the results given in Table 6. Apparently the rail unevenness
can prevent the projectile from sliding on just one rail. This
result suggests that periodic misalignment should purposely be

designed into long tracks to keep the projectile from sliding along a single rail. The only difference introduced between track-projectile configurations of Figure 20 and Figure 22 is that the rail width was doubled for Figure 22. The rail width used in Figure 20, 1.59 cm, (0.625 inches) represents a linear scaling from the current Track G track configuration. A comparison of Figures 20 and 22 shows that doubling the rail width does not change the wear due to aerodynamic heating, but does reduce the wear due to sliding friction. Of course, any increases in rail width will increase overall projectile drag by increasing shock reflection effects.

The results of the initial scaling study presented here when considered together with the comparison of the predictions with Tracks K and G measurements indicate that the Projectile Dynamics Computer Program is now a useful tool for establishing the feasibilities of and deisgn for very large track systems.

SECTION VI

SUMMARY, CONCLUSIONS, AND RECOMMENDATIONS

6.1   SUMMARY

The program undertaken for Arnold Engineering Development
Center and described in this report involved the study of inter-
faces between the projectile and rails in hypervelocity guide-rail
systems. The objective of the study was to provide an analysis of
the interface region between the projectile and the guide-rail which
would be capable of determining the friction force exerted on the pro-
jectile, the wear experienced by the projectile (and possibly
by the rail), and the conditions required to produce gouging of
the rails during projectile passage. The analysis must be
applicable both to rail systems currently in operation and to
future systems which are planned to be far larger than any
currently existing. The program should provide capability
for treating generalized projectile shapes, although special em-
phasis must be placed on the treatment of slender conical fore-
bodied projectiles. The project described in this report was
successful in meeting all but one of these goals (the prediction of
gouging). In addition, the project has produced an analysis (and an
efficient computer program) capable of describing many other aspects
of hypervelocity guidance rail operation.

The initial analysis of the projectile guide rail interface
was based on two assumptions: (1) when the rail system is op-
erating properly, the interface region is a self-pumped gas
bearing which may or may not be affected by ablation products
from the projectile and; (2) physical contact between the pro-
jectile and the rails is a necessary and sufficient condition to
produce gouging of the rails. The first assumption together with
fundamental gasdynamic analyses have been used to identify three

possible types of gas flow within the interface region. These
types of flow were identified by a Reynolds number calculated on
the basis of the average separation between the projectile and
the rail. Operation in two of these regimes can be expected
for practical hypervelocity guidance rail systems. Each of
the practically reached regimes was analyzed thoroughly and com-
puter subroutines describing them were generated.

Early in the project it was realized that conditions in
the interface region are closely coupled to the dynamic behavior
of the projectile along the guide-rails. For this reason, a gen-
eralized analysis of hypervelocity guide-rail operation was de-
veloped. This analysis was formalized in a Projectile Dynamics
Computer Program which combines the interface subroutines with
other subroutines that describe the rigid body motion of the pro-
jectile, the aerodynamic forces experienced by the projectile,
and the detailed geometry of the hypervelocity guide rail.
Later in the program, the importance of elastic deformation of
the projectile wear surfaces was recognized and taken into account
in the program. The program can be used to compute most major
parameters required to describe the projectile passing along a
guide-rail system. Exercising of this program has provided con-
siderable insight into the overall operation of hypervelocity
guide-rail systems. The relative importances of simple aerody-
namic drag, drag induced by forces from the projectile/guide-rail
interface region, and forces produced by reflections of projectile
bow shock waves from the guide-rails back onto the projectile
surfaces were evaluated. The importance of the influence of
normal forces developed by elastic deformation of the projectile
bearing surface on wear has been demonstrated in addition to the
wear produced by aerodynamic heating. Comparisons of some im-
portant aspects of the Projectile Dynamics Computer Program pre-
dictions were made with experimental results obtained from hyper-
velocity guide-rail operations at Tracks K and G at AEDC. These
comparisons showed good agreement between computed and measured
parameters, including total drag, wear, and rotation of projectiles

in flight along the rails. Finally, the Projectile Dynamics
Computer Program was used to conduct an initial scaling study for
investigating the feasibility of developing very large hyper-
velocity guide-rail systems.

No specific rail gouging criterion was developed during
the course of this project. The assumption made at the be-
ginning of this study, namely, that physical contact between the
projectile and the rails is a necessary and sufficient condition
to produce gouging proved to be incorrect. However, with the
addition of elastic deformation of the projectile-bearing surface,
it should now be possible to develop a normal force criterion for
gouging to occur such as that briefly investigated by Graff et al.[3]

6.2   CONCLUSIONS

The project described in this report produced a number
of firm conclusions which are of importance to the operation and
development of hypervelocity guide-rail facilities. These con-
clusions address the following areas; forces and pressures gen-
erated in the interface region between a hypervelocity projectile
and a guide-rail, wearing and gouging characteristics of inter-
face areas; and hypervelocity guide-rail phenomena not directly
connected with the projectile rail interface regions. Conclusions
in this last area are important to the overall guide-rail tech-
nology although they lie beyond the scope of this project.

6.2.1   Development of Projectile Dynamics Computer Program

A complete computer program has been developed with
simulates almost all known aspects of elastically deformable
projectiles traversing a guide-rail system. Aspects not specifically
covered by the program are the elastic response of the rails and
the ablation or erosion of the projectile forebody as it traverses
the rail system.

6.2.2   Interface Flow Regimes

Three separate types of gas flow within the projectile/rail
interface region have been identified. The type of flow existing

in any particular situation is determined by the Reynolds number Re_h calculated on the basis of the gasdynamic conditions within the gap and the gap separation. The three types of flow are:

(1) $Re_h < 10^3$ leads to laminar Couette flow in the interface region;

(2) $10^3 < Re_h < 10^5$ leads to turbulent Couette flow in the interface region;

(3) $Re_h > 10^5$ leads to turbulent boundary layer flow in the interface region.

Analyses of the second and third flow regimes have been emphasized since these are the only ones experienced by systems of practical importance. The first regime usually only occurs with such small gap separation that physical contact between surface asperities almost certainly occurs.

6.2.3 Fundamentally Complex Nature of Interface Flow Analysis

Simple analysis can not be developed for predicting projectile/rail interface parameters because the frictional shear forces (and hence power dissipation within the gap) are strongly dependent upon gap separation, and Re_h which, in turn, is strongly dependent upon several parameters including range gas density, projectile/rail spacing, flow Reynolds number, and the geometry of the projectile forebody.

6.2.4 Relative Magnitudes of the Interface Shear Forces

Projectile drag forces arising in the interface regions are negligible compared to other drag forces acting on the projectile for projectile/rail separations achievable in feasible systems.

6.2.5 Effect of Interface Gas Pressures

Internal gas pressure within the projectile/rail interface regions increases with decreasing gap height, but in general does not cause sufficient restoring forces to prevent the projectile from contacting the rails.

6.2.6 Drag Augmentation By Reflection of Shock Waves

The predicted total drag forces for projectiles with both blunt and slender cone forebodies were compared with

experimental results from the Track K at AEDC. Excellent agreement
was found. Detailed analysis of the slender cone drag leads to
the firm conclusion that bow shocks reflected from the rails are
weak shocks, and the less firm conclusion that the reflected
shock from the rail will re-reflect from the conical surface of
the projectile and contribute significantly to the total drag force.

6.2.7   Importance of Rail Imperfections

In minimizing projectile wear one of the more surprising
insights obtained from the initial scaling study was that rail
misalignment could lead to less projectile wear than the wear
obtained in tracks with perfectly straight rails. Crooked tracks
can insure that the projectile will not slide for too long
a time on a single wear surface. The influence of crooked tracks
is to more evenly distribute the wear over all of the bearing
surfaces. More total mass is generally removed from a projectile
in a crooked track than in one with straight rails, but the
maximum depth of the grooves and the maximum angular rotation of
the projectile is less.

6.2.8   Versatility of the Projectile Dynamics Computer Program

The Projectile Dynamics Computer Program is much more
versatile than its application to date would indicate. For
example, subroutines treating gasdynamics, equilibrium air and
transport properties can be used together as a general purpose
program for studying virtually any one or two-dimensional gas-
dynamic problem involving air flows with temperatures in the
range of 50°K to 8,000°K.

6.3   RECOMMENDATIONS

The development of a powerful computer program useful for
the design and evaluation of current and future hypervelocity
rail guidance systems provides a variety of exciting possibilities
whose exploitation will significantly aid the overall program
for developing improved ballistic range facilities at AEDC.

Additional work is required in three major areas in order to
realize these potentials, however. First, a gouging criterion
based upon determining the critical normal force between a pro-
jectile and a rail which will lead to gouging of the rail should
be developed. The capability of determining the elastic de-
formation of the projectile bearing surfaces: a capability which
was added to the program near the end of this project; makes it
possible to now use this capability to further investigate the
gouging mechanism. Even though rail gouging has proved to not be
a serious problem in either Tracks K or G, this damage mechanism can be
expected to be a potentially serious problem under certain circum-
stances where abnormally large normal forces are generated.

Second, a study should be performed to determine optimum
projectile configurations for minimizing wear. The location
of the center-of-gravity, wheelbase (or length of the cylindrical
portion of a projectile) and shock interaction length are some of
the parameters which the projectile designer can control and these
are parameters which can have a significant influence on pro-
jectile wear. The Projectile Dynamics Computer Program can be
used to assess the relative wear characteristics of rather
general axisymmetric projectiles and with minor modifications
could also be used to assess the wear characteristics of non-
axisymmetric projectiles. There exists the intriguing possibility
that, with a suitably designed projectile, the shock interaction
forces can be used to stabilize an otherwise unstable projectile.

Third, further effort should be directed toward verifying
the true nature of the rail-shock interaction for small half-angle
cones (8° to 15°). To date no good quality schlieren or shadow-
graph photographs have been made of the rail-shock interaction
region for cones with half-angles less than 30°. To our knowledge,
only one 10° half-angle cone-cylinder projectile has been success-
fully launched in Track K and none have been launched
in Track G. Also, apparently none of the existing three-dimensional
method-of-characteristics computer programs have the capability
of analyzing an embedded shock system as complicated as the rail-
shock system. Good quality shadowgraphs of the rail-shock

interaction which can be interpreted unambiguously cannot be made with the instrumentation as presently installed in Tracks K or G because the optical path through the flow field is not perpendicular to a plane defined by two opposing rails. It is recommended that attempts be made to obtain experimental verification of the nature of the rail-shock interaction by some means so that the validity of the simplified model used in the projectile dynamics computer program can be determined with greater certainty than is possible from drag measurements.

APPENDIX A

SIMPLE MODEL FOR PROJECTILE-RAIL INTERFACE

SIMPLE MODEL FOR PROJECTILE-RAIL INTERFACE

For the simple interface model we have assumed that the shear stress (τ) acting on the projectile is proportional to the cube of the velocity (V) and inversely proportional to the rail-projectile separation distance (h). We have assumed the pressure (P_T) acting on the projectile is inversely proportional to the square of the separation distance. Thus we have

$$\tau = c \frac{V^3}{h} \qquad\qquad (A.1)$$

$$P_T = \frac{e}{h^2} \qquad\qquad (A.2)$$

where c and e are proportionality constants.

The separation distance between the rail and projectile at any point along the projectile is a function of the transverse position of the projectile in the rail system and the orientation of the projectile. This is illustrated in Figure 16. The letter ℓ denotes some position along the projectile center line with $\ell = 0$ corresponding to the location of the projectile center-of-gravity. For any value of ℓ along the projectile the separation distance from the upper rail (h_1) is given by

$$h_1 = z_1 - z - \ell \sin \theta - 1/2\, d_p \cos \theta \qquad\qquad (A.3)$$
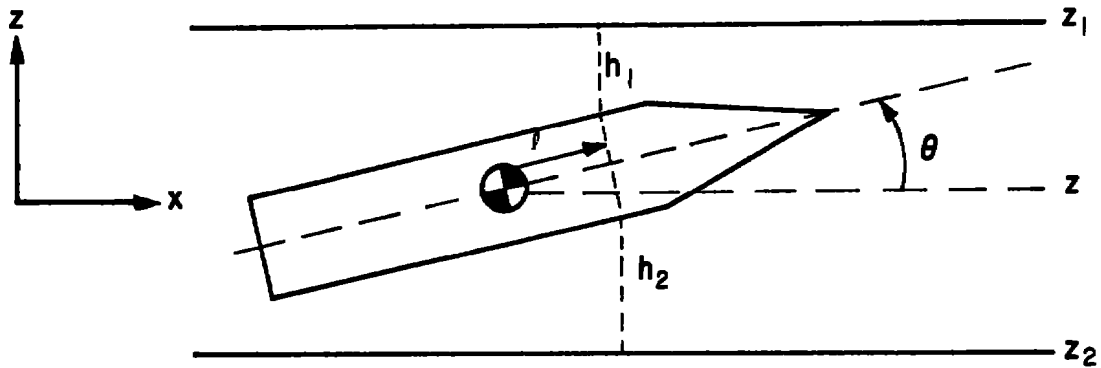
Figure A-1. Separation Distances (At Some Position ℓ Along the Projectile) Between the Projectile and the Upper and Lower Rails.

where

z_1 is the vertical coordinate of the upper rail

z is the vertical coordinate of the projectile center of gravity

d_p is the diameter of the projectile body.

The separation distance from the lower rail (h_2) is

$$h_2 = z - z_2 + \ell \sin\theta - \frac{1}{2} d_p \cos\theta, \qquad (A.4)$$

where z_2 is the vertical coordinate of the lower rail.

In order to determine the motion of the projectile, the shear stress and pressure must be converted into forces and torques acting on the projectile. The shear stress will produce a force (D_I) which is parallel to the projectile body. At some point ℓ along the projectile body the shear stress acting on the projectile is $\tau_1 + \tau_2$, where τ_1 is shear stress from the upper rail and τ_2 is the shear stress from the lower rail. The incremental force ΔD_I at point ℓ is given by

$$\Delta D_I = (\tau_1 + \tau_2) \, W_r \, (\Delta \ell) \qquad (A.5)$$

where

$$\tau_1 = \frac{c \, U_\infty^3}{h_1} \qquad (A.6)$$

$$\tau_2 = \frac{c \, U_\infty^3}{h_2} \qquad (A.7)$$

W_r is the width of the rails, and

$\Delta \ell$ is an increment along ℓ .

The value of D_I is found by integrating the incremental forces over the body of the projectile.

$$D_I = \int_{-\ell_a}^{\ell_f} \left(\frac{cV^3}{h_1} + \frac{cV^3}{h_2} \right) W_r \, d\ell \qquad (A.8)$$

where

ℓ_f is the distance from the center-of-gravity to the forward end of the projectile body, and

ℓ_a is the distance from the center-of-gravity to the aft end of the projectile body.

Substituting Equations (A. 3) and (A. 4) into Equation (A. 8) and performing the integration yields:

$$D_I = \frac{cV^3 W_r}{\sin \theta} \ln \left(\frac{h_{2f} h_{1a}}{h_{1f} h_{2a}} \right) \qquad \text{(A. 9)}$$

where

$$
\begin{aligned}
h_{1f} &= z_1 - z - \ell_f \sin \theta - \frac{1}{2} d_p \cos \theta \\[4pt]
h_{1a} &= z_1 - z + \ell_a \sin \theta - \frac{1}{2} d_p \cos \theta \\[4pt]
h_{2f} &= z - z_2 + \ell_f \sin \theta - \frac{1}{2} d_p \cos \theta \\[4pt]
h_{2a} &= z - z_2 - \ell_a \sin \theta - \frac{1}{2} d_p \cos \theta \ .
\end{aligned}
\qquad \text{(A. 10)}
$$

The factor h_{1f} is the distance between the upper rail and the forward end of the projectile body; h_{1a} is the distance between the upper rail and the aft end of the projectile body; h_{2f} is the distance between the lower rail and the forward end of the projectile body; and h_{2a} is the distance between the lower rail and the aft end of the projectile body. It might be noted that in the limit as θ approaches zero, Equation (A. 9) becomes

$$D_{I_{\theta \to 0}} = cV^3 W_r (\ell_f + \ell_a) \left(\frac{1}{h_{1c}} + \frac{1}{h_{2c}} \right) \qquad \text{(A. 11)}$$

where

h_{1c} is the distance between the upper rail and the center projectile body,

h_{2c} is the distance between the lower rail and the projectile body.

The pressure in the interface zone exerts a force (L_I) perpendicular to the body of the projectile. The pressure from the lower rail (P_2) exerts a positive force on the projectile; the pressure from the upper rail (P_1) exerts a negative force on the projectile. The incremental force (ΔL_I) at some point along the projectile body is

111

$$\Delta L_I = (P_2 - P_1) W_r (\Delta \ell) \qquad (A.12)$$

where $\qquad P_1 = \dfrac{e}{h_1^2},$ and $\qquad (A.13)$

$$P_2 = \dfrac{e}{h_2^2} \quad . \qquad (A.14)$$

The total force is

$$L_I = \int_{-\ell_a}^{\ell_f} \left(\dfrac{e}{h_2^2} - \dfrac{e}{h_1^2} \right) W_r \, d\ell \quad . \qquad (A.15)$$

Substituting Equations (A.13) and (A.14) into Equation (A.15) and performing the integration yields

$$L_I = \dfrac{e W_r}{\sin \theta} \left[\dfrac{1}{h_{1a}} + \dfrac{1}{h_{2a}} - \dfrac{1}{h_{1f}} - \dfrac{1}{h_{2f}} \right] \qquad (A.16)$$

As θ approaches zero Equation(A.16) becomes

$$L_{I_{\theta \to 0}} = k W_r (\ell_f + \ell_a) \left[\dfrac{1}{h_{2c}^2} - \dfrac{1}{h_{1c}^2} \right] \quad . \qquad (A.17)$$

The shear stress can exert a torque (T_s) on the projectile if τ_1 and τ_2 are not equal which occurs when h_1 is not equal to h_2. At some point along the projectile body the incremental torque (ΔT_s) is

$$\Delta T_s = (\tau_1 - \tau_2)(\tfrac{1}{2} d_p) W_r (\Delta \ell) \qquad (A.18)$$

where τ_1 exerts a positive torque and τ_2 exerts a negative torque. The total torque due to the shear stress is

$$T_s = \int_{-\ell_a}^{\ell_f} \left(\dfrac{c V^3}{h_1} - \dfrac{c V^3}{h_2} \right) \tfrac{1}{2} d_p W_r (d\ell) \qquad (A.19)$$

Substituting Equations (A. 3) and (A. 4) into Equation (A. 19) and performing the integration yields

$$T_s = \frac{c V^3 W_r d_p}{2 \sin \theta} \ln \left(\frac{h_{1a} h_{2a}}{h_{1f} h_{2f}} \right) \qquad (A.20)$$

It might be noted that the limit of T_s as θ approaches 0 is

$$T_{s_{\theta \to 0}} = \frac{1}{2} c V^3 W_r d_p (\ell_f + \ell_a) \left(\frac{1}{h_{1c}} - \frac{1}{h_{2c}} \right). \qquad (A.21)$$

The pressure exerts a torque (T_p) on the projectile if P_1 and P_2 are not equal. The incremental torque at some point along the projectile body is

$$\Delta T_p = (P_2 - P_1) \ell W_r (\Delta \ell) \qquad (A.22)$$

where P_2 exerts a positive torque when ℓ is positive and P_1 exerts a negative torque when ℓ is positive. The total torque due to the pressure is

$$T_p = \int_{-\ell_a}^{\ell_f} \left(\frac{e}{h_2^2} - \frac{e}{h_1^2} \right) \ell W_r d\ell \qquad (A.23)$$

Substituting Equation (A. 3) and (A. 4) into Equation (A. 23) and performing the integration yields

$$T_p = \frac{e W_r}{\sin^2 \theta} \left[\ln \left(\frac{h_{2f} h_{1a}}{h_{2a} h_{1f}} \right) + (z - z_2 - \frac{1}{2} d_p \cos \theta) \left(\frac{1}{h_{2f}} - \frac{1}{h_{2a}} \right) \right.$$
$$\left. + (1 - - \frac{1}{2} d_p \cos \theta) \left(\frac{1}{h_{1a}} - \frac{1}{h_{1f}} \right) \right] . \qquad (A.24)$$

It might be noted that the limit of T_p as θ goes to zero is

$$T_{p_{\theta \to 0}} = \frac{e W_r}{2} (\ell_f^2 - \ell_a^2) \left(\frac{1}{h_{2c}^2} - \frac{1}{h_{1c}^2} \right) \qquad (A.25)$$

Equations (A. 10) can be substituted into Equations (A. 9), (A. 16), (A. 20), and (A. 24) to define the forces and torques acting on the projectile due to its interaction with the rail system. These equations are coupled with the equations for other forces and torques acting on the p rojectile to describe the motion of the projectile.

APPENDIX B

A DESCRIPTION OF THE
PROJECTILE DYNAMICS COMPUTER PROGRAM

INPUT VARIABLE DEFINITIONS FOR THE DYNAMIC
RAIL/PROJECTILE SIMULATION PROGRAM

Variable	Definition	Units
TEMPI	Temperature or range gas.	°K
PRESSI	Pressure of range gas.	atmospheres
ANGLEI	Cone half-angle.	degrees
FLAG 1	Upper limit on number of reflected waves between rail and projectile.	Integer
FLAC 2	Controls selection of weak or strong reflected shocks. If set equal to zero, weak shocks are called for unless program decides that this is impossible. If set equal to 1, then the first (and only) reflected shock is considered to be a strong shock.	Integer
DROC	Diameter of projectile body.	m
FLEN	Distance from the center-of-gravity of the projectile to the front sholder of the projectile cylindrical body.	m
ALEN	Distance from the center-of-gravity of the projectile to the aft end of the projectile body.	m
MASS	Mass of the projectile.	kg
MOMIN	Moment of Inertia of the projectile about an axis perpendicular to its longitudinal axis through center-of-gravity.	$kg \cdot m^2$
WR	Rail width.	m
ZETA	Nose bluntness ratio, r_n / r_b.	dimensionless
ALNSI	Distance from base of cone to where bow wave hits rail.	m
CONELH	Distance from base of cone to nose tip.	m
TETAS	Shock wave angle where bow wave hits rail.	
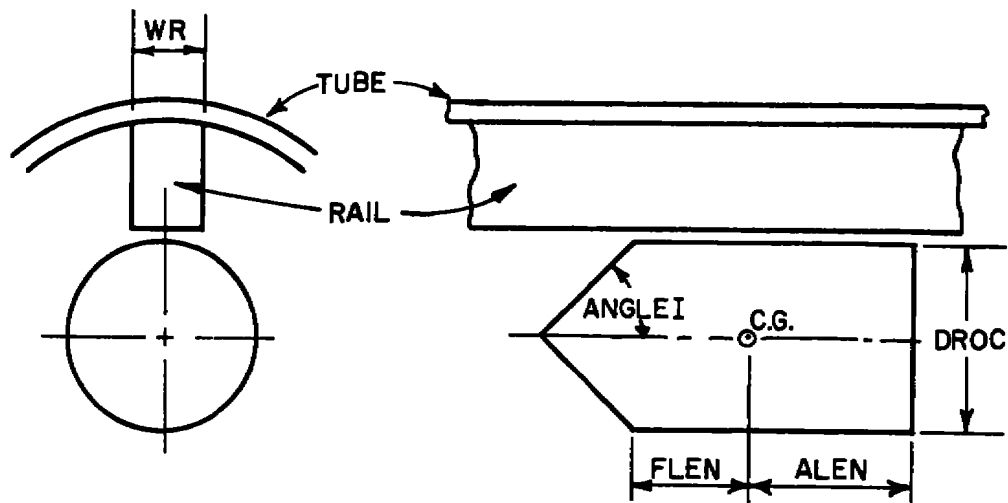
Figure B-1. Sketch Showing Definitions of Rail and Projectile Input
Dimensions.
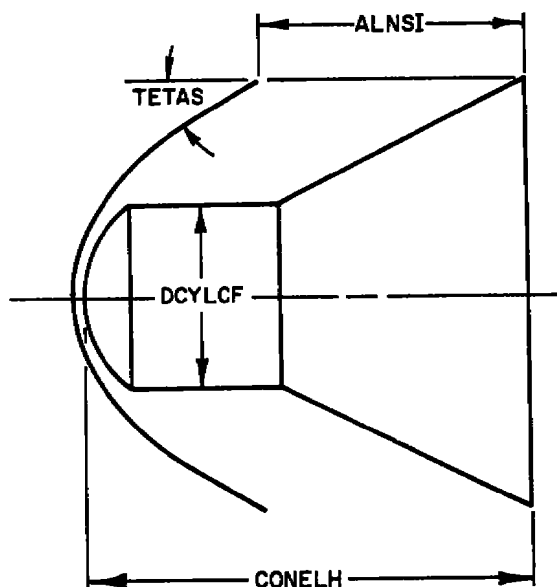
Figure B-2. Sketch Showing Definitions of ALNSI, CONELH, TETAS, and
DCYLCF.

117

Variable	Definition	Units
DCYLCF	Diameter of cylinder on a hemisphere-cylinder-flare projectile	m
IBLUNT	Code number identifying the type of projectile 0 designates a sharp tip cone 1 designates a blunted cone 2 designates a hemisphere-cylinder-flare--read in CONELH and DCYLCF, ALNSI and TETAS are calculated in subroutine SOKSAP 3 designates a hemisphere-cylinder-flare--read in ALNSI, CONELH, TETAS, and DCYLCF	integer
NT	Number of segments which constitute the top rail of the system.	dimensionless
NB	Number of segments which constitute the bottom rail of the system.	dimensionless
YYT	The y-coordinate of the beginning point of the top rail. The x-axis runs parallel to the longitudinal direction of the rail system. The y-axis is perpendicular to the x-axis.	m
YYB	The y-coordinate of the beginning point of the bottom rail.	m
IRULE (I,1)	Code number identifying the geometric shape of the Ith top rail segment as follows: 1 designates a linear segment 2 designates a circular segment 3 designates a parabolic segment 4 designates a sinusoidal segment	dimensionless

Variable	Definition	Units
	For IRULE $(I,1) = 1$, the equation for the rail segment is $$y = mx + b.$$ For IRULE $(I,1) = 2$, the equation for the rail segment is $$y = k \pm \sqrt{r^2-(x-h)^2}.$$ For IRULE $(I,1) = 3$, the equation for the rail segment is $$y = k + \frac{(x-h)^2}{4f}.$$ For IRULE $(I,1) = 4$, the equation for the rail segment is $$y = y_u - A_y + A_y \cos\left(\frac{2\pi x}{L}\right).$$ The x-axis is parallel to the longitudinal direction of the rail system. The y-axis is perpendicular to the x-axis.	
VAR(I,1)	When IRULE $(I,1)$ is 1, VAR(I,1) is the value of m in the equation defining the Ith top rail segment.	dimensionless
	When IRULE $(I,1)$ is 2, VAR(I,1) is the value of r in the equation defining the Ith top rail segment. A positive value of r indicates the curvature is upward; a negative value of r indicates the curvature is downward.	m
	When IRULE$(I,1)$ is 3, VAR(I,1) is the value of f in the equation defining the Ith top rail segment.	m
	When IRULE $(I,1)$ is 4, VAR(I,1) is the value of y_u in the equation defining the Ith top rail segment.	m
DIS(I,1)	The x position at which the Ith top rail ends.	m

Variable	Definition	Units
CX(I, 1)	When IRULE (I, 1) is 1, CX(I, 1) is the value of b in the equation defining the Ith top rail segment.	m
	When IRULE (I, 1) is 2, CX(I, 1) is the value of h in the equation defining the Ith top rail segment.	m
	When IRULE (I, 1) is 3, CX(I, 1) is the value of h in the equation defining the Ith top rail segment.	
	When IRULE (I, 1) is 4, CX(I, 1) is the value of A_y in the equation defining the Ith top rail segment.	
CY(I, 1)	When IRULE (I, 1) is 1, CY(I, 1) is not used; any value can be read-in.	
	When IRULE (I, 1) is 2, CY(I, 1) is the value of k in the equation defining the Ith top rail segment.	m
	When IRULE (I, 1) is 3, CY(I, 1) is the value of k in the equation defining the Ith top rail segment.	m
	When IRULE (I, 1) is 4, CY(I, 1) is the value of L in the equation defining the Ith top rail segment.	m
IRULE(I, 2) VAR(I, 2) DIS(I, 2) CX(I, 2) CY(I, 2)	These variables are defined the same as IRULE (I, 1), VAR(I, 1), DIS(I, 1), CX(I, 1), and CY(I, 1), respectively, except they apply to the Ith bottom rail segment rather than the Ith top rail segment.	
X(1)	The initial x-coordinate of the projectile center-of-gravity (usually 0. 0).	m

120

Variable	Definition	Units
X(2)	The initial y-coordinate of the projectile center-of-gravity. (Must be between the rails in such a manner that the projectile body does not extend outside the rails).	m
X(3)	The initial value of the angle (θ) between the projectile longitudinal axis and the x-axis.	radians
X(4)	The initial value of $\dot{x}$.	m/sec
X(5)	The initial value of $\dot{y}$. (Usually 0.0).	m/sec
X(6)	The initial value of $\dot{\theta}$. (Usually 0.0).	rad/sec
IPCHK	A value of 1 indicates that the output should be printed at specified time intervals. A value of 2 indicates that the output should be printed at specified intervals of x.	dimensionless
IVAR	Indicates which variable should be checked to determine if the numerical integration step should be adjusted. The choices are IVAR = 1, check on the rate of change of x. IVAR = 2, check on the rate of change of y. IVAR = 3, check on the rate of change of θ. IVAR = 4, check on the rate of change of $\dot{x}$. IVAR = 5, check on the rate of change of $\dot{y}$. IVAR = 6, check on the rate of change of $\dot{\theta}$.	dimensionless
T0	The beginning time of the simulation. (Usually 0.0).	sec
TF	The final time of the simulation.	sec

Variable	Definition	Units
XF	The final x-distance of the simulation.	m
TPRNT	The time interval at which output will be printed if IPCHK = 1.	sec
XPRNT	The distance interval at which the output will be printed if IPCHK = 2.	m
CP	The upper limit of central processor time to be used.	sec
CBAR	The mean aerodynamic chord associated with the projectile.	m
CDO	The zero angle of attack drag coefficient for the projectile.	dimensionless
CDA	The change of projectile drag coefficient with change in angle of attack.	per radian
CMO	The zero angle of attack pitching moment coefficient for the projectile.	dimensionless
CMA	The change in projectile pitching moment coefficient with change in angle of attack.	per radian
CLO	The zero angle of attack lift coefficient of the projectile.	dimensionless
CLA	The change in projectile lift coefficient with change in angle of attack.	per radian
CLAD	The change in projectile lift coefficient with the time rate of change of the angle of attack.	per radian
CMAD	The change in projectile pitching moment coefficient with the time rate of change of the angle of attack.	per radian
CLQ	The change in projectile lift coefficient with the change in pitching rate ($\dot{\theta}$).	per radian
CMQ	The change in the projectile pitching moment coefficient with the change in pitching rate ($\dot{\theta}$).	per radian

122

Variable	Definition	Units
G	The acceleration due to gravity. If the two rails being simulated lie in a horizontal plane or if gravity is to be ignored, G should be read-in as 0.0.	m/sec^2
DELTAT	The initial time step of the numerical integration.	sec
HMIN	The minimum time step to be used in the numerical integration.	sec
HFAC	The factor by which the time step is adjusted. If an increase is needed, the present time step will be multiplied by HFAC. If a decrease is needed, the present time step will be divided by HFAC.	dimensionless
VAL1	The value used to determine if the time step should be increased. The test is made on VAL where $$VAL = \left| \frac{RRK(3) - RRK(2)}{RRK(2) - RRK(1)} \right| .$$ RRK(i) is the ith estimate of the rate of change in the variable designed by IVAR. Four estimates of the rate of change of each variable are made at each time step by the fourth order Runge-Kutta numerical integration scheme. If VAL is less than VAL1, the time step is increased by multiplying the present time step by HFAC. A nominal value of VAL1 might be 0.008, but this may depend upon the value of IVAR and the particular system being simulated.	dimensionless
VAL2	The value used to determine if the time step should be decreased. If VAL is greater than VAL2, the time step is decreased by dividing the present time step by HFAC. A nominal value of VAL2 might be 0.08, but this may depend upon the value of IVAR and on the particular system being simulated.	dimensionless

Variable	Definition	Units
HABLAT	Total heat of ablation, L.	Joules/kg
HABL	Heat of ablation due to heat of vaporization and heat of polymerization.	Joules/kg
TWALL	Ablation temperature.	$^{\circ}K$
RHOLEX	Density of projectile material.	kg/m^3
AMUSL	Coefficient of sliding friction, $\bar{\mu}$.	
STIFFC	Elastic deformation coefficient, k_e.	N/m^3

A BRIEF DESCRIPTION OF THE FUNCTION OF THE PROGRAM SUBROUTINES

Section V provides a brief description of the Projectile Dynamics Computer Program (PDCP). Figure 15 shows the basic design of the program. The user should note that the basic system of units used in the PDCP is the MKS system. All of the gasdynamic, thermodynamic, and transport property subroutines; however, use the CGS system of units. The user should also note that specific values of extensive thermodynamic quantities are used in two different ways in the program. When quantities such as enthalpy, entropy and specific heat at constant pressure appear in gasdynamic subroutines, they are expressed on a per gram basis, whereas when they appear in strictly thermodynamic subroutines these quantities appear on a per gram-mole basis. A brief description of each of the 37 individual subroutines follows. Where applicable, references to sources of information used to develop a particular subprogram are given. The listing of the program is replete with comment cards which attempt to describe many of the details of the methods and procedures used in developing the various subroutines.

RAIL

This is the main program. The first function performed is to call INPUT which reads in and initializes quantities. With all quantities initialized, RAIL then calls RK which carries out the numerical integration of the equations of motion. After RK has completed each integration step, all information on the time elapsed, the position of the center-of-mass of the projectile, the first and second derivatives of x, z, and θ and the wear experienced by the top, bottom and side rails during the integration time step are returned to RAIL. RAIL then stores this information along with the results of the previous two integration steps. RAIL then checks to see if the output should be printed. If necessary the Lagrangian interpolation subroutine is called if the output is desired at a time or distance intermediate to the present value of time or distance travelled. The reason for

always having three sets of output stored is so that the Lagrangian inter-
polation can be carried out. RAIL terminates the run when time TF is
reached or when the distance XF is reached. If the velocity of the pro-
jectile decreases by more than 20% from its origianl value, RAIL reinitializes
the gasdynamic conditions and C_{D_0}, C_{L_α}, and C_{m_α} to the current conditions.
It is, of course, possible to update these quantities at the end of each in-
tegration step, but since these quantities do not change drastically or
strongly influence sensitive quantities such as interface normal forces and
moments, it is not necessary to perform these computations at the end of
each integration step.

INPUT

This subroutine reads in all input data. It computes the Mach
number of the projectile from the input data and then computes the shock
angle of an attached conical shock. This computation of the shock angle is
performed by means of a function which is an empirical formula developed
by the authors based on a curve fit to real gas solutions to the conical
shock equations. SOKSAP is then called to compute the thermodynamic
and gasdynamic conditions at key locations on the projectile. The initial
angle-of-attack is computed and then DRAGCO is called to determine initial
values of C_{D_0}, and C_{L_α}, and C_{m_α}. HEATRS is called to determine an
average aerodynamic heating heat transfer coefficient for the interface.

RK

This subroutine is in essence a standard Runge-Kutta fourth-order
numerical integration subroutine having variable time step capability. The
Runge-Kutta method basically computes four separate predictions of the
unknowns to arrive at new values of the unknowns. During each prediction,
RK first computes the angle-of-attack. Then it calls ORIENT to determine
the orientation of the projectile relative to the rails. If any of the separation
distances are negative, ELASTC is called to determine the elastic deformation
forces and moments. With the gap height established for the interfaces, INTER
is called to determine the net interface force components and the net moment

126

due to the interface forces and rail shock interaction forces. Subroutine DRAG is then called to determine the total aerodynamic lift, drag, and moment coefficients at the current angle-of-attack. Subroutine F is then called which determines the force components in the x and z directions. After the four predictions on the unknowns have been computed, RK checks to see if the time step used was too large. If it was, the time step is reduced and the entire procedure indicated above is repeated. If the time step becomes less than a minimum time step read in as input, the program is terminated in RK. If the time step is adequate, a weighted average of the four predictions for each unknown is computed which defines the new values of the unknowns. The new values of the unknowns are then returned to RAIL.

F

This subroutine simply determines the total net force on the projectile in the x and z directions and the net torque.

DRAGCO

The basic function of this subroutine is to determine C_{D_0}, C_{L_α}, and C_{m_α}. C_{L_α} and C_{m_α} are determined for both the conical and cylindrical portions of the projectile using formulas taken from reference 28. The method by which C_{D_0} is determined is fully described in Section 4.1.

DRAG

Given the angle-of-attack and pitching rate, this subroutine determines the total drag coefficient, C_D, the total lift coefficient C_L, and the total moment coefficient about the center of gravity, C_m.

INTER

The complete version of this subroutine is given in Section 4.2 and the simplified version is described in Appendix A.

TURBFP

In this subroutine, the Karman-Schoenherr turbulent skin friction coefficient equation is solved for a given value of the Reynolds number. The

equation being solved is Equation 53 which is an implicit equation. Newton's iterative method for solving for the roots of a transcendental equation is used to determine $\overline{C_f}$.

TURBCE

This subroutine provides the skin friction coefficient for turbulent Couette flow given the Mach number and Reynolds number, Re_h. The Korkegi-Briggs implicit skin friction equation for equal heat transfer rates (Equation 51) is solved by use of Newton's iterative procedure.

ORIENT

This subroutine determines the interface gap heights at four different locations on both the top rail interface and the bottom rail interface. The four locations are the front of the interface, and the three positions on the cylindrical portion of the projectile (see Figure 17). Given the current position of the projectile (x,z, and θ of the center-of-gravity) and geometric quantities related to the dimensions of the projectile this subroutine determines the space coordinates of the four positions indicated above for both the top and bottom of the projectile. Subroutine CONFIG is then called to determine the space coordinates of the top and bottom rails at these four locations. From all of this information, ORIENT then computes the gap heights. Note that gap heights are not computed for the side rail interfaces since the program does not account for lateral motion of the projectile.

If a negative gap height is obtained, ORIENT signals RK through the value of ICOLIN that this has occurred. RK then calls ELASTC . ORIENT prints out a message that an apparent collision with the wall has occurred and tells where on the projectile the apparent collision has occurred.

ELASTC

This subroutine is called from subroutine RK whenever ORIENT determines that the distance between a bearing surface and the rail has become negative, based upon rigid body behavior. ELASTC then computes by means of the equations given in Appendix C, the normal forces required to de-

form the projectile bearing surfaces to zero separation distance. The
moments associated with these normal forces are also computed in
ELAST C.

LGRNG

This is a standard 3 point Lagrangian interpolation subroutine.

CONFIG

This subroutine gives the space coordinates of either the top or
bottom rail at any position x along the rail system. The shape of the rails
is defined by input information which is fully described at the beginning of
this Appendix.

GASDYN

This subroutine solves normal and oblique shock problems for air
and serves as an executive subroutine for carrying out other gasdynamic
computations. This subroutine along with the equilibrium air subroutines
and the undissociated air subroutines can be used over a temperature range
of $50^{\circ}K$ to about $8500^{\circ}K$. At the low end of the temperature range the
user has to use some judgment since the program cannot tell if O_2 or
N_2 will liquify. At the upper end of the temperature range some judgment
must also be used since the ionization of atomic species is not included in
the equilibrium air subroutines.

Some of the details of this subroutine have been presented in Section
3.4.1 and will not be repeated here. The first computation performed in
the subroutine is to determine the conditions immediately downstream of the
bow shock where it hits the rail. Given the shock angle at the rail and initial
conditions GASDYN determines the turning angle of the flow and the downstream flow

conditions. The second computation is to determine the conditions which exist on the cylindrical portion of the projectile. This is accomplished by a call to subroutine PMEXP which performs a Prandtl-Meyer expansion from conditions existing behind the conical shock to conditions which exist behind a flow which has turned through an angle equal to the cone half-angle. The third computation is to determine the conditions downstream of the reflection of the bow shock from the rail. The conditions upstream of this first reflected shock are those just previously computed and the turning angle is the same as the turning angle of the flow as it passed through the bow shock. The shock angle for this first reflected shock is unknown. An estimate of the shock angle based on a solution to the perfect gas with constant specific heat oblique shock equations is obtained from subroutine CUBIC. The oblique shock equations are then solved (three equations in three unknowns) as described in Section 3.4.1. The program will ordinarily assume that weak shock solutions are desired unless a strong shock solution is specifically requested by setting FLAG 2 equal 1 (see the first part of this Appendix for a full description of the input quantities). If the turning angle is too large for a given Mach number, a weak shock solution is not physically possible in which case the program will do a strong shock solution. The user specifies the upper limit on the number of weak reflected shocks that he wants to consider by FLAG 1. GASDYN will determine the conditions behind each of these reflected waves; or if regular reflection is not possible, for a given shock, it will do a strong shock solution and tell the user the number of the shock which has been considered to be a strong shock which, of course, must be the last shock then regardless of what the value of FLAG 1 is. The initial conditions plus conditions behind each subsequent shock are stored in COMMON. After conditions behind all shocks are determined, conditions at other points of interest are determined. First, sonic conditions for the flow behind the last shock are established by a call to CONSTS. Next, conditions at state 4

(conditions after expansion from conditions behind the last shock in the system to the pressure existing behind the attached conical shock, P_2) are determined. If the flow is still supersonic after the last shock, then PMEXP is called to do this expansion. If the flow behind the last shock is subsonic, then PMEXP is called to expand the flow from sonic conditions to P_2 if the pressure at sonic conditions is greater than P_2. If the pressure at sonic conditions is less than P_2, CONSTS is called to isentropically compress the air from sonic conditions to P_2. Finally, stagnation conditions corresponding to the flow behind the last shock are determined by another call to CONSTS.

The thermodynamic and flow properties at each of the conditions described above are stored in COMMON, Table 5 shows how the various points are labelled.

PMEXP

This subroutine performs Prandtl-Meyer expansions and compressions. Three options are provided for handling three different kinds of processes. The calling agrument of this subroutine includes a variable called IPM and another variable called ISTATE. If IPM=1, the turning angle of the flow is specified (through DELNU). If IPM=2, the final pressure is specified (through PF). If IPM=3, the final Mach number is specified (through AMF). The initial conditions are specified through ISTATE which designates the number of the initial state. Initial state conditions are presumed to be available in COMMON labelled STATE. Conditions at the end of the Prandtl-Meyer process are also stored in STATE at the location specified by FSTATE which is also a part of the calling argument for PMEXP. Values of the Prandtl-Meyer function, the thermodynamic properties, and the flow velocity and Mach number are stored at each integration step so they can be used in other subroutines to help define flow conditions at the entrance to the interface region.

The first part of the subroutine uses ideal gas relations to solve Prandtl-Meyer flows. The second part of the subroutine, which is used for high

131

TABLE 1. ISTATE DESIGNATIONS

The gasdynamic conditions at each state in the system are stored in labeled COMMON designated by STATE. The following numbering system for labeling the states is used in the program.

State No.	Gasdynamic Description of State
1	Free-stream conditions.
2	Behind conical (or first) shock.
3	Behind first reflected shock (first reflection off rail).
4	Behind second reflected shock (first reflection off cone).
5	Behind third reflected shock (second reflection off rail).
6	Behind fourth reflected shock (second reflection off cone).
7	Conditions after Prandtl-Meyer expansion around cone-cylinder shoulder (conditions along side of rail-projectile interface).
8	Dummy - stores intermediate state results. If conditions behind last shock are subsonic, then conditions after expansion to M=1 are stored here. Also used to store intermediate results when conditions behind the last shock are highly supersonic. In this case, if CONSTS subroutine does not converge when attempting to locate sonic conditions the results after Prandtl-Meyer expansion to M=4 are stored here.
9	Conditions after expansion from pressure existing behind last shock to pressure existing behind the first shock.
10	Stagnation conditions behind the last shock in the system.

temperature conditions, uses numerical integration to solve the Prandtl-Meyer flow pressure as the integration variable. CONSTS is used in the numerical integration to determine the change in thermodynamic and flow properties with each incremental change in pressure. A Modified Simpson's Rule is used for the numerical integration. The equation which is integrated is given by

$$d\omega = \sqrt{\left(\frac{V^2}{a^2} - 1\right)} \ \frac{d(\ln P)}{{}_0 V^2/P}$$

where $d\omega$ is the angle through which the flow turns as the result of an incremental change in pressure $d(\ln P)$.

      This subroutine actually possesses much more capability than is used in the present version of the Projectile Computer Program. For example, this subroutine rogether with expressions for determining the displacement thickness of the three-dimensional boundary layers on the rail and the projectile could be used to define much more precisely the pressure distribution in the interface for cases where a significant inviscid core region exists between the two boundary layers. This subroutine could be used to perform detailed computations of the circumferential expansion of the inviscid core flow in the interface.

CUBIC

      This subroutine is used to solve the cubic equation which relates the shock wave angle to Mach number and specific heat ratio for two-dimensional flow over a wedge of a perfect gas with constant specific heat. This subroutine is called to provide an estimate of the shock angle when the Mach number and turning angle are known. The equation solved in this subroutine is Equation 150a in Reference 28. This subroutine also includes a hypersonic similarity law empirical formula that gives the shock angle in terms of the Mach number and wedge half-angle. This formula is used when the wedge angle is large and the Mach number is also large.

EQAIR

This subroutine solves for the equilibrium composition of dissociated (but not ionized) air given the temperature and pressure of the air. The composition of the air in a non-dissociated state is taken to be dry air having a molar composition of 20.979% O_2, 78.087% N_2, and 0.934% Argon. The formula weight of one mole of this air is 28.963 grams/gram-mole. Some of the details of this subroutine are discussed in Section 3.4.1. The basic formulation of the coupled set of equilibrium thermodynamic equations and the method of solution is too lengthy to present here. The details are given in Reference 30. Suffice it to point out that the general development follows that originally presented in Reference 31. A great amount of thought and effort has gone into EQAIR in order to produce a computationally efficient program. The procedures used in this subroutine are not straightforward or easy to understand. The Newton-Raphson procedure is used to solve a system of six coupled non-linear algebraic equations. The equations consist of three chemical equilibrium equations for the following reactions:

$$O_2 \rightleftharpoons 2O$$
$$N_2 \rightleftharpoons 2N$$
$$1/2 \, O_2 + 1/2 \, N_2 \rightleftharpoons NO \,,$$
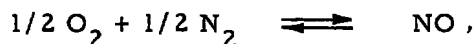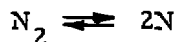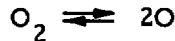
two mass balance equations: one for conservation of oxygen atoms and one for conservation of nitrogen atoms, and Dalton's law of partial pressure.

IGUESS

This subroutine determines initial estimates of the composition of the equilibrium air given the temperature and pressure of the air. These initial estimates are used in EQAIR to start the Newton-Raphson iterative procedure. The equations used to determine the initial estimates of the unknowns were developed along lines similar to those discussed in Reference 30.

SONIC

This subroutine determines the speed of sound of equilibrium air given the temperature, density, and composition of the air as determined in EQAIR. The method used is based on that presented in Reference 31.

DERIV

This subroutine determines the thermodynamic derivatives $\left(\dfrac{\partial H}{\partial T}\right)_P$, $\left(\dfrac{\partial H}{\partial P}\right)_T$, $\left(\dfrac{\partial \rho}{\partial T}\right)_P$, and $\left(\dfrac{\partial \rho}{\partial P}\right)_T$ which are used in GASDYN to carry out the Newton-Raphson procedure applied to solution of the normal shock and oblique shock equations. This subroutine calls CSOLVR to solve a system of linear algebraic equations. The unknowns in one set of linear equations are the thermodynamic derivatives $\left[\dfrac{\partial(\ln n_j)}{\partial(\ln)}\right]_T$ and the unknown in another set of linear algebraic equations are the thermodynamic derivatives $\left[\dfrac{\partial(\ln n_j)}{\partial \ln T)}\right]_P$. These thermodynamic derivatives together with temperature, pressure, density, composition, and individual species thermodynamic properties allow one to determine the four thermodynamic derivatives defined at the beginning of this paragraph. The general method used here is described in Reference 31.

CONSTS

The basic function of this subroutine is to perform thermodynamic process computations for both dissociated air and non-dissociated air. This subroutine can also be used to determine thermodynamic properties when conditions other than temperature and pressure are known. For instance, this subroutine is used in INTER to determine the temperature corresponding to a state where the pressure and enthalpy are known (that is to determine the temperature corresponding to the Sommer-Short reference enthalpy at a pressure equal to the pressure at the edge of a boundary layer). The primary function of this subroutine; however, is to determine

conditions at the end state of an isentropic expansion or compression. The subroutine contains 5 basic options defined by IFLG. If IFLG=1, the final entropy and pressure are specified, if IFLG=2, the final entropy and temperature are specified, if IFLG=3, the final entropy and enthalpy are specified, if IFLG=4, the final entropy and Mach number are specified, and if IFLG=5, the final pressure and enthalpy are specified. In each option, given the specified quantities and initial velocity or Mach number, the other end point thermodynamic properties and velocity and/or Mach number will be determined. The development of this subroutine is based on the method outlined in Reference 31. One non-obvious procedure used to implement option five needs to be explained. The initial enthalpy must be read in as HT and the specified final enthalpy must be read in as MWT.

CSOLVR

This is a linear equation solver subroutine. The method used is Gaussian elimination with pivotal condensation.

TRANSP

This subroutine determines viscosity and thermal conductivity of high temperature air given the temperature and mole fractions of the constituents of the air. The methods used in this subroutine are taken directly from Reference 22.

TCHEM

This subroutine determines the individual specie ideal gas thermodynamic properties at the input temperature and a pressure of one atmosphere. The change in the Gibbs function; change in entropy, and change in enthalpy for each of the three reactions discussed in the description of EQAIR, evaluated at one atmosphere, are also computed in this subroutine as well as the equilibrium constants for the three reactions. This subroutine serves as an executive subroutine with most of the computations actually performed in the following four subroutines which represent a statistical thermodynamic package for the determination of thermodynamic properties[32].

SPECF

This subroutine calculates thermodynamic properties of N_2, O_2, O, N, NO and Ar. Specific heats, enthalpy, and entropy at one atmosphere are computed from partition functions for translation, rotation, vibration, and electronic excitation contributions. At high temperatures, anharmonicity corrections are applied.

TRANS

Evaluates the translational partition function for each species.

VIBR

Evaluates the vibrational partition function for each species.

CORREC

Evaluates anharmonicity corrections for each species.

MUSTAR

A function subprogram which returns the viscosity of undissociated air given the temperature of the air.

KSTAR

A function subprogram which gives the thermal conductivity of undissociated air.

SIG

A function subprogram which gives the Prandtl number of undissociated air.

CPSTAR

A function subprogram which determines the specific heat of undissociated air.

GAMMA

A function subprogram which gives the specific heat ratio of undissociated air.

ENT

This function determines by means of table lookup the enthalpy of undissociated air considered to be a perfect gas. This function returns an enthalpy divided by a constant given by .0686132 x 273.16. The data in the table were calculated with SPECF of this program and are nearly identical to those given in Reference 33. The temperature range is 50 to 3000°K. The table is in increments of 10°K up to 800°K and incrementsof 50°K from 800°K to 3000°K.

KELVIN

This is the inverse function of ENT. It returns the temperature of air given the enthalpy divided by 0.0686132 x 273.16.

SOKSAP

The primary function of this subroutine is to determine the shape of the bow shock and compute both the axial location where the bow shock would intersect the rail if the gap height were zero and the angle of the bow shock at this location. The method used to estimate the shape of the bow shock is that given by Inouye.[34] The shock standoff distance is computed by Inouye's method after GASDYN has been called to determine the density ratio across the normal shock. After the position and angle of the bow shock at the radial distance r_b have been determined, the quantities ALNSI and TETAS defined in Figure B-2, GASDYN is called to determine the gasdynamic conditions at the states defined in Table 1 of this Appendix.

HEATRS

This subroutine is used to determine boundary layer heat transfer coefficients. The methods used are taken directly from Appendix C of Reference 27.

APPENDIX C

LINEAR ELASTIC DEFORMATION ANALYSIS
OF PROJECTILE BEARING SURFACES*

*This analysis was developed by Dr. J.B. Hicks of the Aeroballistic
Branch of VKF at AEDC.

LINEAR ELASTIC DEFORMATION ANALYSIS
OF PROJECTILE BEARING SURFACES*

The basic concept used to determine the elastic deformation of the projectile bearing surface is to allow the surface to deform whatever amount is necessary to prevent a negative separation distance from occurring between the projectile and the rail. The elastic deformation analysis of the projectile is not coupled to the gas bearing analysis, that is, no elastic deformation is considered when separation distances are positive.

Subroutine ORIENT determines the separation distances at the front and rear of the top and bottom bearing surfaces. These distances are defined in Appendix A as h_{1f}, h_{1a}, h_{2f}, and h_{2a} where the subscripts 1 and 2 refer to the top and bottom bearing surfaces, respectively while the subscripts f and a refer to the front and rear (aft) ends of the bearing surfaces, respectively. Whenever any of these separation distances are negative subroutine ELASTC is called to determine the normal force required to deform the bearing surface to zero separation distance.

Three simplifying assumptions are made in the development of the elastic deformation analysis. First, the force per unit area $P_{e\ell}$ required to deform the surface by an amount $\delta_{e\ell}$ is assumed to follow a linear relationship of the form given by

$$P_{e\ell} = k_e \delta_{e\ell} \tag{C-1}$$

where k_e is an elastic coefficient. Second, the deformation over the width of bearing surface is assumed to be constant. Third, the deformation over the length of the bearing surface is assumed to be linear. The total normal force is then obtained by integrating Equation (C-1) over the length of the bearing surface where negative separation distances occur.

---

*This analysis was developed by Dr. J.B. Hicks of the Aeroballistic Branch of VKF at AEDC.

The methods used to arrive at the working equations used in subroutine ELASTC based upon integrating Equation C-1 are next described. Three separate cases are defined for determining the working equations depending on the signs of the separation distances. These three cases are defined for the top surface as follows:

Case 1 : $h_{1a} \leq 0$ and $h_{1f} \leq 0$

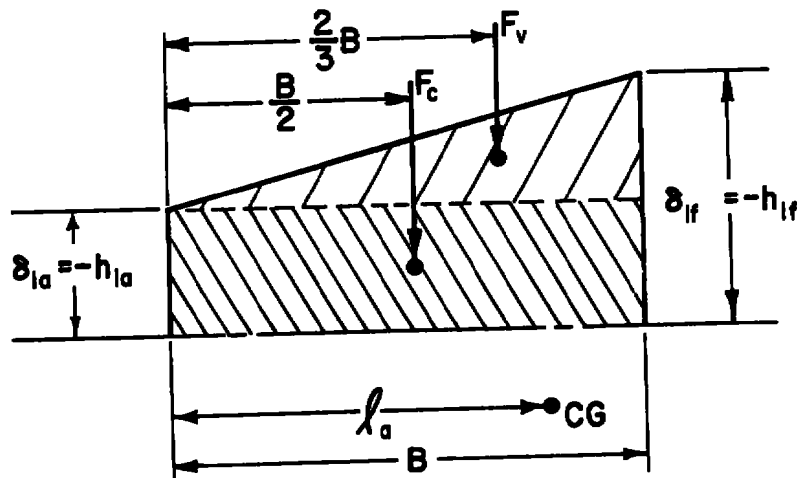Case 2 : $h_{1a} \geq 0$ and $h_{1f} < 0$

Case 3 : $h_{1a} < 0$ and $h_{1f} \geq 0$

Similarly, three cases are defined for the bottom surfaces.

<u>Case 1 for Top Bearing Surface</u> (h_{1a} and h_{1f} both negative)

The following loading diagram sketch for Case 1 (top surface) is used to define certain quantities and illustrate the method used to determine the total normal force and moment.

For Case 1 this sketch illustrates that the total loading can be considered as the sum of a constant loading and a variable (linear) loading. The normal force due to the uniform loading, F_c is simply

$$F_c = - W_r Bk_e h_{1a} \qquad \text{(C-2)}$$

while the normal force due to the linear loading, F_r is

$$F_r = -\frac{1}{2} W_r Bk_e (h_{1f} - h_{1a}) \qquad \text{(C-3)}$$

The total normal load, F_n is then

$$F_n = - F_c - F_r$$

The total normal load on the top bearing surface F_{n1} is then (with the same sign convention as used in Section V and Appendix A).

$$F_{n1} = \frac{1}{2} W_r Bk_e (3 h_{1a} - h_{1f}) \qquad \text{(C-4)}$$

The moment about the center-of-gravity of F_n is the sum of the moment due to F_c and F_v and can be written by inspection of the loading diagram as

$$T_{I_1} = - F_c (\frac{B}{2} - \ell a) - F_v (\frac{2}{3}B - \ell a) \qquad \text{(C-5)}$$

where again the sign convention is that used in Section V and Appendix A.

Case 2 for Top Bearing Surface (h_{1f} negative, h_{1a} positive)

The loading diagram for Case 2 is as follows:
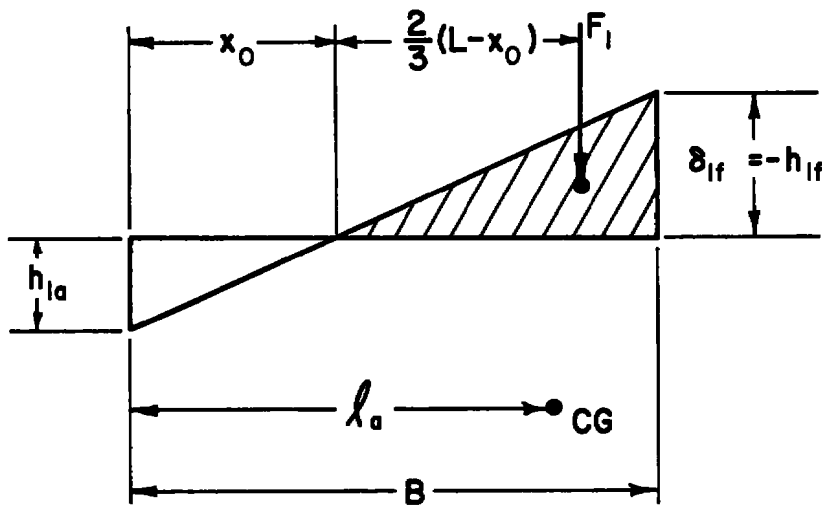
The normal force and moment can very simply be expressed in terms of the distance from the rear of the projectile to the point where the loading is zero, x_o. From the law of similar triangles, x_o can be written as

$$\frac{x_o}{h_{la}} = \frac{B}{h_{la} - h_{lf}}$$

<div align="right">(C-6)</div>

or

$$x_o = \frac{B}{\left(1 - \dfrac{h_{lf}}{h_{la}}\right)}$$

and from inspection of the loading diagram

$$F_{nl} = -F_1 = \frac{W_r k_e h_{lf}}{2}(B - x_o)$$

<div align="right">(C-7)</div>

and the moment about the center-of-gravity is

$$T_{I_1} = -F_1\left[x_o + \frac{2}{3}(L - x_o) - \ell_a\right]$$

which can be simplified to

$$T_{I_1} = - F_1 \left(\frac{x_o}{3} + \frac{2}{3} B - \ell_a \right)$$

(C-8)

Case 3 for Top Bearing Surface (h_{la} negative, h_{lf} positive

The loading diagram for Case 3 is as follows
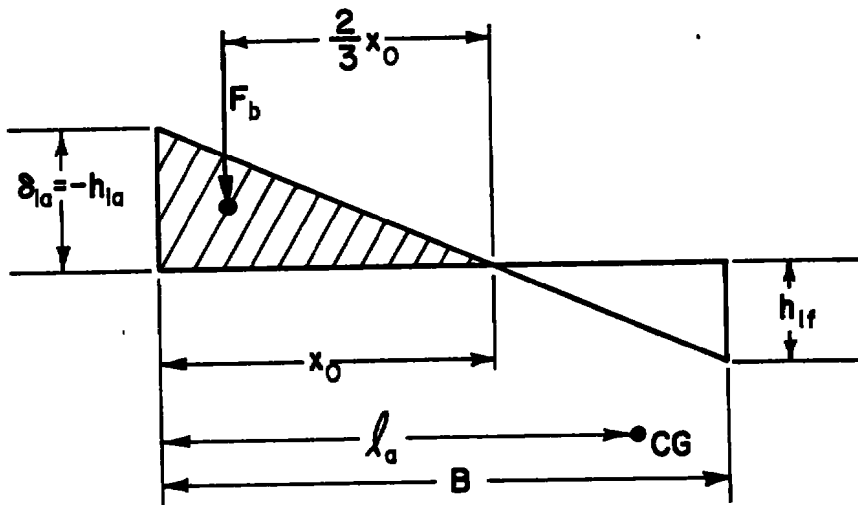
The law of similar triangles applied to this loading diagram leads to

$$\frac{x_o}{-h_{la}} = \frac{B}{h_{lf} - h_{la}}$$

or

(C-9)

$$x_o = \frac{B}{\left(1 - \frac{h_{lf}}{h_{la}} \right)}$$

and from inspection of the loading diagram

$$F_{n1} = - F_1 = \frac{1}{2} W_r k_e h_{la} x_o$$

(C-10)

and the moment is

$$T_{I_1} = F_1 \left(\ell_a - \frac{x_o}{3} \right)$$ (C-11)

The normal loads and moments due to elastic deformation of the bottom bearing surface for each of the three cases can be written by inspection of the loading diagrams for each corresponding top surface case. The same sign convention is used for the bottom surface as for the top, that is, forces are positive in the upward direction and counterclockwise moments are positive.

Case 1 for Bottom Surface (h_{2f} and h_{2a} both negative)

$$F_c = - W_r B k_e h_{2a}$$ (C-12)

$$F_v = - \frac{1}{2} W_r B k_e (h_{2f} - h_{2a})$$ (C-13)

$$F_{n2} = - \frac{1}{2} W_r B k_e (3 h_{2a} - h_{2f})$$ (C-14)

$$T_{I_2} = F_c \left(\frac{B}{2} - \ell_a \right) + F_v \left(\frac{2B}{3} - \ell_a \right)$$ (C-15)

Case 2 for Bottom Surface (h_{2f} negative and h_{2a} positive)

$$x_o = \frac{B}{\left(1 - \dfrac{h_{2f}}{h_{2a}} \right)}$$ (C-16)

$$F_{n2} = - \frac{1}{2} W_r k_e (B - x_o) h_{2f}$$ (C-17)

$$T_{I_2} = F_{n2} \left(\frac{x_o}{3} + \frac{2B}{3} - \ell_a \right)$$ (C-18)

Case 3 for Bottom Surface (h_{2a} negative and h_{2f} positive)

$$x_o = \frac{B}{(1 - \dfrac{h_{2f}}{h_{2a}})} \tag{C-19}$$

$$F_{n2} = -\frac{1}{2} W_r x_o k_e h_{2a} \tag{C-20}$$

$$T_{I_2} = -F_{n2} (\ell_a - \frac{x_o}{3}) \tag{C-21}$$

The elastic deformation analysis developed here is incorporated in the computer program in subroutine ELASTC. Note that this analysis is based upon assuming that the interface region can be represented by one straight line segment. This procedure is thus inconsistent with the method used to track the wear of the top and bottom interface regions as described in Section 5.4. Two straight line segments are used to describe the geometry of the top and bottom wear surfaces. Therefore, an obvious improvement in the accuracy of the program could be made by using two straight line segments to define the shape of the elastically deformed interface.

REFERENCES

1. Teng, R.N., Hickman, R.S., and Sutila, G.E., "Development of a Scaled-Up Hypervelocity Guiding and Retrieving System," AEDC-TR-74-123, Arnold Engineering Development Center, January 1975.

2. Norfleet, G.D., Hendrin, R.E., and Jackson, D., "Development of a Hypervelocity Track Facility at AEDC," AIAA 15th Aerospace Sciences Meeting, Paper 77-151, Los Angeles, California, January 1977.

3. Graff, K.F., and Dettloff, B.B., "The Gouging Phenomena Between Metal Surfaces at Very High Sliding Speeds," Wear 14, 1969, pp. 87-97.

4. Gerstle, F.P., Follansbee, P.S., Pearsall, G.W., and Shepard, M.L., "Thermoplastic Shear and Fracture of Steel During High Velocity Sliding," Wear 24, 1973, pp. 97-106.

5. Gerstle, F.P., and Pearsall, G.W., "The Stress Response of an Elastic Surface to a High Velocity Unlubricated Punch," JAM 41, 1974, pp. 1036-1040.

6. Bowden, F.P., and Tabor, D., The Friction and Lubrication of Solids, Part II, Clarendon Press, Oxford, 1964.

7. Dayson, C., "The Sublimating Film Gas Bearing," Wear 30, pp. 149-178, 1974.

8. Gross, W.A., Gas Film Lubrication, John Wiley and Sons, 1962.

9. Schlichting, H., Boundary Layer Theory, 3rd Edition, McGraw-Hill.

10. Korkegi, R.H., and Briggs, R.A., "On Compressible Turbulent Plane Couette Flow," AIAA Journal, Vol. 6, No. 4, April 1968, pp. 742-744.

11. Korkegi, R.H. and Briggs, R.A., "Compressible Turbulent Plane Couette Flow with Variable Heat Transfer Based on Von Karman Model," AIAA Journal, Vol. 8, No. 4, April 1970, pp. 817-819.

12. Korkegi, R.H. and Briggs, R.A., The Hypersonic Slipper Bearing-- A Test Track Problem, Aerospace Research Laboratory Report ARL 69-0074, May 1969.

13. Boylan, D.E., Axial-Force Measurements on Cone Cylinders Mounted in a Simulated Aeroballistic Range Track in Tunnel F with Application to a Full Scale System, Arnold Engineering Development Center Report AEDC-TR-75-78, May 1975.

REFERENCES (Continued)

14. Wilkins and Taylor, "Boundary Layer Transition of Ablating Cones at Speeds up to 7 km/s," AIAA Journal 4, 1966, pp. 1344-1348.

15. Intrien, Kirk, Chapman, and Terry, "Ballistic Range Tests of Ablating and Nonablating Slender Cones," AIAA Journal 8, 1970, pp. 558-564.

16. Korkegi, R.H., and Briggs, R.A., Aerodynamics of the Hypersonic Slipper Bearing, Aerospace Research Laboratory Report ARL 68-0028, February 1968.

17. Mirels, Harold, "Laminar Boundary Layer Behind Shock Advancing into Stationary Fluid," NACA TN 3401, 1955.

18. Mirels, Harold, "Laminar Boundary Layer Behind a Strong Shock Moving into Air," NACA TN D-291, 1961

19. Boehman, L.I., "Stability of the Boundary Layer Induced by a Moving Shock Wave," Air Force Flight Dynamics Laboratory Technical Memorandum, AFFDL-TM-75-20-FXE, 1975.

20. Boison, J.C., "Investigation of Test Facility Environmental Factors Affecting Boundary Layer Transition," AFFDL-TR-73-106, 1973, (also "Highly Cooled Boundary Layer Transition Data in a Shock Tube," proceedings of the Tenth International Shock Tube Symposium, 1975, pp. 127-140.

21. Ostrach, S., and Thornton, P.R., "Stability of Compressible Boundary Layers Induced by a Moving Wave," Journal of the Aerospace Sciences, Vol. 29, 1962, pp. 289-296.

22. Hansen, F.C., "Approximations for the Thermodynamic and Transport Properties of High-Temperature Air," NASA TR R-50, 1959.

23. Korkegi, R.H., and Briggs, R.A., "On Compressible Turbulent Plane Couette Flow," AIAA Journal, Vol. 6, No. 4, April 1968, pp. 742-744.

24. Korkegi, R.H., and Briggs, R.A., "Compressible Turbulent Plane Couette Flow with Variable Heat Transfer Based on Von Karman Model," AIAA Journal, Vol. 8, No. 4, April 1970, pp. 817-819.

25. Katsikas, C.J., Castle, G.K., and Higgins, J.S., "Abletion Handbook-Entry Materials Data and Design." AFML-TR-66-262, November 1966.

REFERENCES (Continued)

26. Thompson, Philip A., <u>Compressible Fluid Dynamics</u>. McGraw-Hill, 1972.

27. Richards, B.E., Culotta, S., and Slechten, J., "Heat Transfer and Pressure Distributions on Re-Entry Hose Shapes in the VKI Longshot Hypersonic Tunnel," AFML-TR-71-200, June 1971.

28. Truitt, R.W., <u>Hypersonic Aerodynamics</u>, Ronald Press, 1959.

29. <u>Equations, Tables, and Charts for Compressible Flow</u>, NACA Report 1135, 1953.

30. Boehman, L.I., "Design of a Combustion Tunnel and Experimental Test Program," Published in 1975, USAF-ASEE Summer Faculty Research Program Research Reports, Air Force Office of Scientific Research, September 1975, pp. 1-19 to 1-32.

31. Huff, V.N., Gordon, S., and Morrell, V.E., "General Method and Thermodynamic Tables for Computation of Equilibrium Composition and Temperature of Chemical Reactions," NACA Report 1037, 1951.

32. Mariscalco, M.G., "Evaluation of the Partition Function in the Computation of Thermodynamic Properties for Perfect Gas Products of Combustion," Masters Degree Research Project Report, Department of Mechanical Engineering, University of Dayton, Dayton, Ohio, July 20, 1976.

33. Hilsenrath, J., et al., <u>Tables of Thermal Properties of Gases</u>. National Bureau of Standards Circular 564, November 1955.

34. Inouye, Mamoru, "Blunt Body Solutions for Spheres and Ellipsoids in Equilibrium Mixtures," NASA Technical Note TN D-2780, May 1965.

LIST OF SYMBOLS

A	Area of interface
A_c	Ablating contact area
$A\ell$	Interface area affected by lubrication
a	Sound speed
B	Length of projectile bearing surface
ΔB	Increase in B caused by wear into the conical surface
B_c	Correction coefficient to account for mass added to boundary layer
c	Proportionality constant for shear stresses
$\bar{c}$	Distance from center-of-gravity to center-of-pressure
C_D	Aerodynamic drag coefficient
C_L	Aerodynamic lift coefficient
C_f	Skin friction coefficient for laminar Couette flow
$\bar{C}_f$	Average skin friction coefficient
C_m	Aerodynamic pitching moment coefficient
$C_{1..5}$	Numerical factors involving pressure drag defined after Equation 35
C_{D_α}	Coefficient defining the change in the drag coefficient with a change in angle of attack
C_{D_b}	Base drag coefficient
C_{D_p}	Drag coefficient from pressure on the forebody
$C_{D_{SI}}$	Drag coefficient arising from the interference of the shock wave by the rails

LIST OF SYMBOLS (Continued)

C_{D_T} Total projectile drag coefficient

C_{D_v} Viscous drag coefficient on entire projectile

C_{D_0} Drag coefficient at zero angle of attack

C_L^0 Lift coefficient

C_{L_α} Coefficient defining the change in the lift coefficient with a change in angle of attack

C_{L_q} and C_{L_α} Damping coefficients associated with the lift

$C_{L_{SI}}$ Lift coefficient arising from the interference of the shock wave by the rails

C_{L_0} Lift coefficient at zero angle of attack

C_m Moment coefficient

C_{m_0} Lift coefficient at zero angle of attack

C_{m_α} Coefficient defining the change in the pitching moment coefficient with a change in angle of attack

C_{m_q} and $C_{m_{\dot\alpha}}$ Damping coefficients associated with the pitching moment

$C_{m_{SI}}$ Pitching moment coefficient arising from the interference of the shock wave by the rails

$C_{p\ max}$ Term defined especially for Equation 36

D_A Aerodynamic drag force

D_I Frictional force between projectile and rail

d_p Projectile diameter

e Proportionality constant involving transverse pressure

F Viscous force

F_{av} Average viscous force

F_n Normal force due to elastic deformation

F_{sf} Sliding friction force

LIST OF SYMBOLS (Continued)

f_{lube}	Lubrication force
f_{tan}	Net tangential force due to interface phenomena
G	Proportionality constant
g	Acceleration of gravity
H	Gas enthalpy
H*	Reference enthalpy
h	Gap heighth
h_m	Minimum gap heights
h_1	Gap heighth to top rail
h_2	Gap heighth to bottom rail
h_{1a}	Distance between upper rail and rearward end of projectile
h_{1c}	Distance between upper rail and center of projectile
h_{1f}	Distance between upper rail and forward end of projectile
h_{2a}	Distance between lower rail and rearward end of projectile
h_{2c}	Distance between lower rail and center of projectile
h_{2f}	Distance between lower rail and forward end of projectile
h_m	Minimum gap heighth
I_y	Pitching moment of inertia of projectile
K	Boltzmann constant
k	Thermal conductivity of interface gas
k_e	Elastic coefficient
L	Heat of ablation

LIST OF SYMBOLS (Continued)

L_A	Aerodynamic lift force
L_I	Lift force from projectile/rail interface
ℓ	Distance along projectile body from center of gravity
ℓ_a	Distance from rear of projectile to center of gravity
ℓ_f	Distance from front of projectile to center of gravity
Δ_ℓ	Increment along projectile position parameter, 1
M	Mach Number
M_p	Projectile mass
MW	Molecular weight
m	Individual molecular mass, or projectile mass
m_a	Ablative mass loss
M_{sf}	Ablation mass loss rate from sliding friction
n	Number density of atoms
P	Static pressure
$\bar{P}$	Average static pressure
P_T	Transverse gas pressure in interface
P_{SI}	Average pressure on cone surface
P_{abl}	Interface pressure caused by ablation products
$P_{e\ell}$	Local elastic deformation force
P_1	Pressure on projectile from upper rail interface
P_2	Gas pressure in region 2 defined in Figure 6
$\dot{Q}_{sf}$	Energy dissipation from sliding friction
q	Pitch rate $(\dot{\theta})$
$\bar{q}$	Nondimensional heat flux at the rail

LIST OF SYMBOLS (Continued)

q_w	Heat flux to ablative wall
R_a	Gas constant for ablation products
Re	Reynolds Number
$Re*$	Lubrication Reynolds Number
Re_B	Reynolds Number based on length B
Re_h	Reynolds Number based on gap heighth, h
Re_{ls}	Reynolds Number based on free stream conditions and cone slant length
$Re_{\Delta x}$	Reynolds Number based on Δx
Re_x	Reynolds Number based on x
r_b	Cone base radius
r_n	Nose radius
S	Cross sectional area of projectile
s	Entropy
T	Gas temperature
T_A	Aerodynamic torque
T_I	Torque from projectile/rail interface
T_p	Torque on projectile from pressure couple in interface
T_S	Torque on projectile from shear couple in interface
T_v	Ablation temperature
T_w	Rail temperature
T_∞	Range gas temperature
U_∞	Sliding velocity
u	Local gas velocity component along rail axis

LIST OF SYMBOLS (Continued)

V	Projectile velocity
v	Local gas velocity component along circumference of projectile
W	Projectile velocity component normal to rail
W_r	Width of rails
w	Local gas velocity component normal to rail
W'	Average bearing pressure above inlet pressure
Δx	Distance along rail from strong shock to gap entrance
Δx_{SI}	Distance from cone base to reflected shock impingement point
x	Denotes direction of projectile travel
y_δ	Laminar boundary layer thickness
z	Vertical coordinate of projectile center of gravity
z_1	Vertical coordinate of upper rail
z_2	Vertical coordinate of lower rail

GREEK SYMBOLS

Λ	Bearing number
α	Angle of attack
β	Define parameter for Equation 51
γ	Angle between velocity vector and rail axis
$\delta_{e\ell}$	Local elastic deformation
σ	Cone half-angle
θ	Angle between longitudinal axis of projectile and rail axis
θ_i	Shock angle from rail axis

LIST OF SYMBOLS (Continued)

θ_s	Shock angle
θ_r	Shock reflection angle
μ	Gas viscosity
$\bar{\mu}$	Coefficient of sliding friction
ν	Kinematic viscosity using pressure from region n of Figure 6 and temperature of rail
ν_n	Kinematic viscosity (n refers to gas region from Figure 6)
ζ	Bluntness ratio
ρ	Gas density
τ	Equivalent shear stress of interface region
τ_w	Stress defined in Equation 45
τ_{xz}	Viscous shear stress in x direction
τ_{yz}	Viscous shear stress in y direction
τ_1	τ evaluated on upper rail
τ_2	τ evaluated on lower rail
ϕ	Non-dimensional ablative mass loss
'	Prime specifies turbulent fluctuations of quantity

SUBSCRIPTS

aw	adiabatic wall conditions
b	Projectile base conditions
e	Conditions at edge of boundary layer
number	Gas dynamic conditions for regions defined in Figure 6 and Section 3.3.2
∞	Free stream conditions
w	Conditions evaluated at a surface